

**CHARACTERIZATION AND DESIGN OF LIQUID
CRYSTAL POLYMER (LCP) BASED MULTILAYER RF
COMPONENTS AND PACKAGES**

A Dissertation
Presented to
The Academic Faculty

By

Dane Thompson

In Partial Fulfillment
of the Requirements for the Degree
Doctor of Philosophy
in
Electrical and Computer Engineering



School of Electrical and Computer Engineering
Georgia Institute of Technology
May 2006

Copyright © 2006 by Dane Thompson

**CHARACTERIZATION AND DESIGN OF LIQUID
CRYSTAL POLYMER (LCP) BASED MULTILAYER RF
COMPONENTS AND PACKAGES**

Approved by:

Dr. John Papapolymerou, Co-Advisor
Assoc. Professor, School of ECE
Georgia Institute of Technology

Dr. Mark Allen
Professor, School of ECE
Georgia Institute of Technology

Dr. Manos Tentzeris, Co-Advisor
Assoc. Professor, School of ECE
Georgia Institute of Technology

Dr. Andrew Peterson
Professor, School of ECE
Georgia Institute of Technology

Dr. Joy Laskar
Professor, School of ECE
Georgia Institute of Technology

Dr. Dennis Hess
Professor, School of Chemical and Biomolecular Engineering
Georgia Institute of Technology

Date Approved: March 31, 2006

TABLE OF CONTENTS

ACKNOWLEDGEMENTS	v
LIST OF TABLES	vii
LIST OF FIGURES	viii
LIST OF SYMBOLS AND ABBREVIATIONS	xiv
SUMMARY	xvi
CHAPTER 1 INTRODUCTION	1
CHAPTER 2 BACKGROUND	13
CHAPTER 3 INVESTIGATION OF LCP MM-WAVE DIELECTRIC PROPERTIES	17
3.1 mm-Wave Dielectric Characterization	17
3.1.1 Ring Resonator Method	18
3.1.2 Cavity Resonator Method	27
3.1.3 Transmission Line Method	29
3.1.4 Summary of LCP mm-wave Dielectric Properties	30
3.1.5 Transmission Line mm-wave Loss Characteristics	31
3.2 High Temperature mm-wave Dielectric Characterization	39
3.2.1 Method of Identifying Dielectric Stability	39
3.2.2 Thermal Coefficient of Dielectric Constant Measurement	41
3.2.3 Dielectric Constant Thermal Stability Results	43
3.2.4 High Temperature Dielectric Characterization Conclusion	46
CHAPTER 4 MULTILAYER LCP PROCESS DEVELOPMENT	47
4.1 Bonding Process	48
4.2 Laser Processing	53
4.3 Alignment	59
CHAPTER 5 LCP PASSIVE DEVICE PACKAGING AND TESTING	61
5.1 Example: NASA 14/35 GHz dual-polarization 2x2 element antenna arrays	61
5.2 Flexibility Testing	63
5.3 LCP Water Absorption	70
5.3.1 Water Absorption Measurement	72
5.3.2 Water Weight Gain	73

5.4	Passive Device Sensitivity to Water Absorption	76
5.4.1	Device Selection	76
5.4.2	Fabrication	77
5.4.3	Measurement	77
5.4.4	Corrosion	79
5.4.5	Passive Device Sensitivity to Water Conclusion	79
CHAPTER 6 LCP ACTIVE DEVICE PACKAGING AND TESTING		81
6.1	Package Interconnect	82
6.2	MEMS Switch Package	84
6.3	Microwave Monolithic Integrated Circuit (MMIC) Packaging	88
6.3.1	Packaging Concept	88
6.3.2	Component Selection	90
6.3.3	Multilayer LCP Package Design Considerations	91
6.3.4	Package Fabrication	93
6.3.5	MMIC Measurements	97
6.3.6	Packaged MMIC Conclusion	98
6.4	MMIC Package Water Seal Testing	99
CHAPTER 7 CONCLUSION		101
REFERENCES		104

ACKNOWLEDGEMENTS

First, I would like to thank my parents, Jim and Patricia Thompson, for their support throughout my perpetual student career. I owe them a huge debt of gratitude for lending open ears to many, many talks over the years and for making sure I was enjoying myself along the way. Since grade school, they insisted that school was my “job”, and I took them seriously. The phrase “make it happen” has been a family motto and has culminated in long journey of education and discovery.

My advisors, Manos Tentzeris and John Papapolymerou, have been instrumental in putting together an amazing collaborative lab with world class tools, facilities, and people. I am very grateful for spending my time at Georgia Tech in such a great learning environment under their mentorship. In addition, they have created a research program with ever present industry contact to ensure our research challenges were both challenging and plentiful while working on relevant and new topics. The help with late night paper edits and the training/preparation sessions for presentations at many conferences were also greatly appreciated.

I would like to thank Dr. Mark Allen for the sharing of his laser lab and other equipment/facilities such as the microscopes, digital scales, hot presses, and automated drills. I also owe Richard Shafer a huge debt of gratitude for training and assisting me with Dr. Allen’s equipment. He helped with numerous processes and real world implementation ideas that were critical for the realization of the thin-film LCP packages. In general, Richard was selfless with his time, often going above and beyond standard requirements and even answering calls over the weekend. Thank you Richard!

Lauren Rose at the Georgia Tech Microelectronics Research Center (MiRC) was a project saver with her willingness to perform wire bonding for the amplifier chips. Thanks

Laureen for your great attitude and excellent wire bonding job, especially on short notice.

The staff in the Georgia Tech (MiRC) cleanroom were important contributors to helping my research. Specifically, thanks to Vinh Nguyen for his help with the Karl Suss wafer bonder, and to Gary Spinner for keeping the whole operation running.

Of course, I could not have made it through PhD studies without the help and friendship of my fellow graduate students. Thank you all for the conversations, cleanroom tips/suggestions, and design/measurement help. I would type out specifics, but the number of items I am grateful/thankful for would take another dissertation to type out! So I'll do a generic "thank you" to everyone for your unique individual contributions during my time at Georgia Tech. Probably most important was the shared extracurricular activities that kept me sane during a sometimes ridiculously demanding process. Thanks again, and when I get my first paycheck, the beers are on me (or rootbeer for some of you)!

LIST OF TABLES

Table 1	Transverse coefficient of thermal expansion comparison	15
Table 2	Ring resonator configurations	19
Table 3	Ring resonator impedances	21
Table 4	TRL lines used in CB-CPW-to-microstrip transitions	22
Table 5	Summary of reported LCP material properties	31
Table 6	Losses from CB-CPW transmission lines	33
Table 7	CPW configurations measured.	34
Table 8	Losses from microstrip transmission lines	38
Table 9	Alignment plate geometries	59
Table 10	Low water absorption materials tested	72
Table 11	Water absorption compared with “in air” conditions	76

LIST OF FIGURES

Figure 1	Examples of applications below 10 GHz which can be cheaply and compactly integrated and packaged with the SoC approach.	2
Figure 2	System-in-package exploded pictorial representation.	3
Figure 3	System-in-package side view pictorial representation.	4
Figure 4	Real (ϵ') and imaginary (ϵ'') parts of the permittivity of water. ϵ' is the same thing as the dielectric constant and ϵ'' is the loss term (not the loss tangent).	5
Figure 5	Dielectric constant and loss tangent of water vs. frequency and temperature. A phenomenon called dielectric relaxation occurs in water across the plotted frequency range where the dielectric constant drops from ~ 80 to a value closer to 5 while the loss tangent peaks at 1.76 (880 times higher than a low loss microwave substrate with $\tan \delta = 0.002$) anywhere from 40–100 GHz depending on the temperature.	6
Figure 6	Examples of hermetic metal packages.	7
Figure 7	Antenna efficiency vs. normalized substrate thickness for microstrip patch antennas on the minimum and maximum dielectric constants for standard LTCCs and for the dielectric constant of LCP.	9
Figure 8	Atmospheric attenuation of electromagnetic energy by water vapor and oxygen as function of frequency. To obtain the total loss these curves must be added to each other.	10
Figure 9	Water and oxygen permeability of different polymer families.	13
Figure 10	CAD drawing of ring resonator configuration with CB-CPW to microstrip transitions.	19
Figure 11	Transmission-line cross sections for: (a) microstrip, (b) CB-CPW, and (c) CPW.	20
Figure 12	Microstrip ring resonator configuration diagram.	20
Figure 13	Fabricated ring resonators and TRL calibration lines on 5 mil LCP. A 1 mil low melting temperature LCP bond layer was used to affix a $5 \mu\text{m}$ smooth copper foil to avoid losses due to conductor surface roughness above 30 GHz.	23
Figure 14	S_{21} measurement for ring resonator configuration D.	24

Figure 15	Extracted dielectric constant using ring resonator designs A through F and cavity resonators with 2 and 4 mil LCP.	24
Figure 16	LCP loss tangent versus frequency for 2 and 4 mil substrate thicknesses measured with the cavity resonator method. Results for the ring resonator method and the transmission line (TL) method on 3 mil LCP substrates are shown with and without subtracting radiation loss. The values extracted from the cavity resonator method are the benchmark for accuracy due to the much higher Q -factor of the the resonant cavity topology.	26
Figure 17	Cavity resonators used in collaboration with the University of Limoges, France, and NIST, Boulder, CO.	27
Figure 18	LCP loss tangent versus frequency for 2 and 4 mil substrate thicknesses measured with the cavity resonator method.	29
Figure 19	CB-CPW line losses on 2-8 mil LCP substrate thicknesses.	33
Figure 20	CPW total measured loss on a lossy poster-board spacer.	35
Figure 21	CPW total measured loss on a hollow plastic spacer.	35
Figure 22	CPW total measured loss on a low loss foam spacer.	36
Figure 23	Microstrip line losses on 2-5 mil LCP substrate thicknesses.	37
Figure 24	Drafting drawing for the custom aluminum spacer plates to elevate the mm-wave mixing modules.	41
Figure 25	Heated temperature measurement setup on the 8510XF network analyzer. The digitally controlled Temptronic hot chuck and custom aluminum spacer plates are shown.	42
Figure 26	Absolute value of the thermal coefficient of dielectric constant, τ_{ϵ_r} , vs. frequency of several standard materials and of the broadband τ_{ϵ_r} for LCP. The closer $ \tau_{\epsilon_r} $ is to zero, the more stable the dielectric constant is with respect to temperature.	44
Figure 27	The ratio of LCP's heated dielectric constant and the dielectric constant at 25 °C vs. temperature. The values for LCP are for measurements from 11–105 GHz from this research. As a comparison, 99.5% alumina and PTFE/glass have been included. Notice that the values for 99.5% alumina and for PTFE/glass are for measurements at 10 GHz.	45

Figure 28	LCP's dielectric constant vs. frequency and temperature. The dielectric constant increases with increasing frequency and decreases with increasing temperature. Note that the peak at 21 GHz did not have a well shaped gaussian distribution and thus the resonant frequency could not be accurately calculated. However, the 21 GHz measurement at 125 °C was the best fit at that frequency and so only it is included for an estimate of the dielectric constant.	45
Figure 29	Attenuation of 3 and 5 mil LCP substrate microstrip transmission lines as a function of temperature. Line width, W, was 104 μm for both lines which gave $Z_0 = 68 \Omega$ and 88Ω for the 3 and 5 mil thicknesses, respectively.	46
Figure 30	LCP modulus of elasticity vs. temperature. The sharp drop near 285 °C for type 2 LCP corresponds to an abrupt material phase change where it rapidly changes from a solid to a liquid with increasing temperature. . . .	49
Figure 31	The Karl Suss silicon wafer bonder enables a precise LCP lamination process for a total thickness of up to several millimeters.	50
Figure 32	Recommended LCP bonding profile.	52
Figure 33	Bare LCP layers cut into the desired shapes with the CO ₂ laser, including the sample perimeter, alignment holes, and cavities in the left sample. . .	54
Figure 34	Four mil LCP with 18 μm copper on each side with four alignment holes drilled by the infrared laser. The green color seen through the holes is polyester green tape used to protect the backside metallization during the etching process.	55
Figure 35	248nm KrFl excimer laser. Minimum obtainable features are $\sim 5\mu\text{m}$	56
Figure 36	Precise alignment hole cut with the excimer laser.	56
Figure 37	Laser cut samples before and after oxygen plasma cleaning.	59
Figure 38	Small aluminum alignment fixture.	60
Figure 39	June 2003 LCP antennas. These antennas were the first devices bonded after the development of a successful LCP bond recipe.	61
Figure 40	December 2004 aperture coupled 2x2 antennas with all of the patterned layers shown.	62
Figure 41	Diagram of the layer stackup for the final design for the aperture coupled 2x2 antennas.	62
Figure 42	December 2004 aperture coupled 2x2 antennas resting on the alignment fixture.	63

Figure 43	S_{11} measurements for the first generation of 14 and 35 GHz antenna arrays on LCP.	64
Figure 44	The 14 GHz 1x2 antenna array on a 17 mil bonded LCP substrate.	64
Figure 45	Measurement repeatability testing by connecting the antenna five times and re-measuring it. The dotted rectangle area is magnified and re-plotted in Figure 46.	65
Figure 46	Zoomed in plot of Figure 45. The resonance minimum occurs at the exact same frequency point every time showing that the measurement is repeatable when the antenna is in its default (flat) state.	66
Figure 47	Various pipe diameters in which to roll the 14 GHz antenna.	67
Figure 48	The antenna conformed inside the 2-5/8" inner pipe diameter.	67
Figure 49	The antenna rolled around a magic marker and taped in place.	68
Figure 50	The antenna roll diameter from the magic marker shown in comparison to the diameter of a penny.	68
Figure 51	Top and side views of the residual curvature of the antenna after taking it out of the 2-5/8" diameter pipe.	68
Figure 52	Top and side views of the residual curvature of the antenna after taking it off of the magic marker.	69
Figure 53	Measurement results of all of the cases of flexing the antenna. Two of the measurements include the antenna in a curved state while the rest are of the flattened antenna after conforming it to different roll diameters.	69
Figure 54	Zoomed in representation of Figure 45.	70
Figure 55	2" x 2" test sample with four 14 GHz microstrip patch antennas.	73
Figure 56	Measured sample weights to the nearest tenth of a milligram for the following cases: 1) Immediately after baking in an oven at 110°C for 1 hour; 2) Dry, at room temperature and ambient humidity; 3) After 24 hours submersed on edge in distilled water, the surface water dried thoroughly upon removal, and the sample measured immediately; 4) With the same method as 3) except after the samples were submerged for 16 days.	74
Figure 57	Measured frequency shift of 14 GHz microstrip patch antennas for the two submersion cases as compared with the resonant frequency from the "in air" case.	78

Figure 58	Frequency shifts of the worst case 14 GHz antenna on the 6202 substrate after the 16 day submersion in water. This plot corresponds to the 0.55% frequency shift case from Figure 57. Successive traces are of the same antenna after waiting 2 minutes and 10 minutes for the water embedded in the board to evaporate. After 10 minutes the response is identical to the dry measurement made before the submersion. The original trace for the dry measurement is not shown to reduce plot clutter. Also shown for comparison is the antenna simulation result.	79
Figure 59	14 GHz microstrip patch antennas on a control board which was kept in air at ambient humidity vs. an antenna that was submersed in distilled water for 16 days. The submersed antenna demonstrates the corrosion that can occur due to moisture interaction with copper.	80
Figure 60	Three different FGC cross sections present in the measured packaging structures. Impedance values are from HFSS 3D simulator for an FGC with signal width $S=200 \mu\text{m}$, gap $G=120 \mu\text{m}$, and $\epsilon_r = 3.16$. Z_0 only differs by 4Ω in the three different cross sections.	83
Figure 61	S_{11} for cavities with electrical lengths from $0-360^\circ$. The CB-FGC in the cavity has $Z_0 = 57 \Omega$ and the CB-FGC with superstrate feeding the cavity has $Z_0 = 53 \Omega$. The feeding CB-FGC lines are $\lambda_G/4$ at 20 GHz which is an optimal configuration for minimizing the already low reflections. . . .	83
Figure 62	Air-bridge type MEMS switch on an LCP substrate. The springs anchor the membrane to the CB-FGC's ground planes [not shown]. Note: Dark brown is electroplated gold. Yellow is evaporated gold.	85
Figure 63	Top left: LCP superstrate packaging layer with holes for alignment and probe feed-throughs. The packaged cavities between each set of probing holes are visible due to LCP becoming partially transparent at a 2 mil thickness. Top right: CB-FGC transmission lines with air-bridge RF MEMS switches in the center of the transmission lines. Bottom right: Both layers stacked on alignment fixture and probed through the feed-through windows.	86
Figure 64	Comparison of S-parameter measurements of an air-bridge type CPW MEMS switch in the "UP" state. Case 1: The switch is measured in open air. Case 2: The packaging layer is brought down and taped into hard contact and measured. Case 3: A top metal press plate and a fifteen pound weight are put on top of the packaging layer (15psi) to simulate bonding pressure. The weight and the press plate are then removed and the switch was re-measured.	87
Figure 65	Comparison of S-parameter measurements of an air-bridge type CPW MEMS switch in the "DOWN" state. The three measurement cases shown are the same as those explained in the caption for Figure 64. . . .	87

Figure 66	Comparison of S-parameter measurements of the MEMS switch transmission line after the switch was physically removed. The cases with the package and without the package layer are nearly the same.	88
Figure 67	Pictorial side view of package stackup.	89
Figure 68	Comparison of the LCP multilayer package stackup. The left picture shows only the package layers with cavities. The right picture shows the full LCP package stackup.	90
Figure 69	Comparison of the LCP laser machined base layer before and after the MMIC and parallel plate capacitor were mounted with an inorganic silver paste and wire bonded to the feed lines.	94
Figure 70	Hittite HMC342 13–25 GHz GaAs LNA and a 130 pF parallel plate bypass capacitor attached inside of an excimer laser micromachined cavity in a 4 mil LCP substrate. Aluminum wedge wire bonds connect the components to the feeding transmission lines.	94
Figure 71	Top view of the 13-25 GHz GaAs MMIC packaged in multiple thin layers of LCP.	95
Figure 72	Gain measurement of the Hittite HMC342 13–25 GHz LNA. The chip measures very similarly with or without the LCP package. The package presence and package lamination process show no significant effect. . . .	98
Figure 73	S_{11} measurement of the Hittite HMC342 13–25 GHz LNA.	98
Figure 74	18 μm thick LCP transmission line passing directly through the side of a bonded superstrate package stackup.	99
Figure 75	Gain measurement of the Hittite HMC342 13–25 GHz LNA. The first measurement is of the packaged/bonded MMIC. The second measurement was done immediately after the packaged MMIC was submerged in water on edge for 48 hours. The match of the measurements demonstrates a successful seal by the LCP package. The minimal water absorption into the package shows no significant effect on the MMIC performance.	100

LIST OF SYMBOLS AND ABBREVIATIONS

$>$	greater than.
α_d	dielectric loss (here in units of nepers per meter).
ϕ_c	interior cavity diameter.
CB-CPW	conductor-backed coplanar waveguide.
CB-FGC	conductor-backed finite ground coplanar.
$^\circ$	degrees.
cm	centimeter.
CPW	coplanar waveguide.
CTE	coefficient of thermal expansion.
dB	decibel.
ϵ''	loss term.
ϵ_r	dielectric constant.
Δf	frequency shift.
f_0	resonance frequency or center frequency.
GaAs	gallium arsenide.
GHz	gigahertz = 10^9 cycles per second.
GSG	ground-signal-ground.
LCP	liquid crystal polymer.
LTCC	low-temperature co-fired ceramic.
MEMS	micro-electro-mechanical-systems.
MiRC	Microelectronics Research Center.
mm	millimeter.
mm-wave	millimeter-wave.
MMICs	monolithic microwave integrated circuits.
μm	micrometer or micron = 10^{-6} meter.

NIST	National Institute of Standards and Technology.
PEC	perfect electric conductor.
ppm	parts per million.
PTFE	polytetraflouroethylene.
PTHs	plated through holes.
<i>Q</i>	quality factor.
RF	radio frequency.
rms	root-mean-square.
SiGe	silicon germanium.
~	similar to.
SoC	system-on-chip.
SOLT	short-open-load-through.
SoP	system-on-package.
ΔT	temperature difference.
τ_{ϵ_r}	temperature coefficient of dielectric constant.
tan δ	loss tangent.
THz	terahertz = 10^{12} cycles per second.
TRL	through-reflect-line.
VNA	vector network analyzer.
WLANs	wireless local area networks.

SUMMARY

This thesis discusses the investigation and utilization of a new promising thin-film material, liquid crystal polymer (LCP), for microwave and millimeter-wave (mm-wave [>30 GHz]) components and packages. The contribution of this research is in the determination of LCP's electrical and mechanical properties as they pertain to use in radio frequency (RF) systems up to mm-wave frequencies, and in evaluating LCP as a low-cost substrate and packaging material alternative to the hermetic materials traditionally desired for microwave circuits at frequencies above a few gigahertz (GHz).

A study of LCP's mm-wave material properties was performed. Resonant circuit structures were designed to find the dielectric constant and loss tangent from 2-110 GHz under both ambient and elevated temperature conditions. Several unique processes were developed for the realization of novel multilayer LCP-based RF circuits. These processes include thermocompression bonding with tight temperature control (within a few degrees Celsius), precise multilayer alignment and patterning, and LCP laser processing with three different types of lasers. A proof-of-concept design that resulted from this research was a dual-frequency dual-polarization antenna array operating at 14 and 35 GHz.

Device characterization such as mechanical flexibility testing of antennas and seal testing of packages were also performed. A low-loss interconnect was developed for laser-machined system-level thin-film LCP packages. These packages were designed for and measured with both RF micro-electromechanical (MEM) switches and monolithic microwave integrated circuits (MMICs). These research findings have shown LCP to be a material with uniquely attractive properties/capabilities for vertically integrated, compact multilayer LCP circuits and modules.

CHAPTER 1

INTRODUCTION

As frequencies tend to increase for the next generation of wireless applications, the materials and integration techniques in radio frequency (RF) systems are experiencing more demanding performance constraints. At microwave and millimeter-wave (mm-wave) frequencies, the water and gas permeability characteristics of the RF substrate and packaging materials are critical to reliable operation and long service lifetimes. Above a few gigahertz (GHz), substrate water absorption can lead to unacceptable losses in elements such as antennas, filters, and transmission lines. As a result, the substrate materials that absorb moisture whose losses are small for 2.4 and 5.8 GHz wireless local area networks (WLANs) may no longer be suitable for applications at 10 GHz or above. Higher frequencies also mean circuits get smaller, and low material expansion (which is related to a material's water absorption characteristics) becomes more important for circuit reliability. Equally important is the ability to integrate these materials easily and cheaply with different system components. Finally, consumers are demanding continually better performance for the lowest possible price. New material technologies must be identified that can simultaneously tackle these challenges of performance, invariance to frequency and environmental changes, and cost.

Two major philosophies for addressing these mm-wave (30–300 GHz) RF packaging concerns are system-on-chip (SoC) and system-on-package (SoP). System-on-chip is a fully integrated design with RF passives and digital and/or optical functions on wafer [1]. For SoC, particularly at mm-wave frequencies, gallium arsenide (GaAs) is often required for the high cutoff frequency performance it offers transistors, and for the low substrate loss it provides analog components. However, GaAs is expensive, and using large areas of the substrate for analog components is not cost-effective. Silicon germanium (SiGe) on either CMOS/BiCMOS grade Si or high resistivity Si is a lower cost replacement for GaAs for

some applications, but it is still a relatively lossy substrate for passive RF components.

The SoC method is attractive from a cost standpoint when it is feasible (at relatively low frequencies) since a single component like a capacitor on-chip costs about one-quarter of a cent and an entire transceiver cost is about 25 cents, while taking up less than 4 mm² [2]. These prices are far below what is achievable with standard microwave substrate materials (referring to the price per passive function since active functions are only possible on-chip). Intel expects to eventually produce an entire RF transceiver on a silicon chip operating up to a maximum frequency of about 10 GHz. Some examples of these compact, inexpensive RF modules that are packaged and readily available for applications below 10 GHz are shown in Figure 1.



Figure 1. Examples of applications below 10 GHz which can be cheaply and compactly integrated and packaged with the SoC approach.

Past 10 GHz, the losses incurred by such RF functions as filtering and mixing become too great for reasonable accommodation on silicon chips. This is the approximate cutoff point for when systems with a combination of chips for the signal processing and passive elements on an external low-loss RF substrate for other functions becomes necessary (excluding the very expensive GaAs from the analysis).

Passive component examples are on-board metallized traces like transmission lines, filters, and antennas, while active component examples include chips such as amplifiers and oscillators. The antenna is almost always much more useful off-chip due to size, efficiency, and radiation pattern improvements. A result of these considerations is that RF systems

with frequencies in the mm-wave spectrum require intelligent material and topology selections for the off-chip substrate material selection. Put simply, the high frequency wireless industry is looking for materials with excellent electrical and mechanical properties suited for packaging *and* integrating passive and active components into environmentally robust RF modules.

To reduce the size, complexity, and cost of RF systems, multilayered substrate materials in which passive elements are integrated as distributed elements inside the substrate/packaging layers is required. A solution for the compact integration of these passive components, potentially with embedded active chips as well, is the system-on-package (SoP) approach. SoP condenses space hungry analog components into a multilayer dielectric material and integrates chips within or on the same dielectric packaging material [3]. An exploded representation of a SoP stackup is shown in Figure 2. A side view with a similar representation is seen in Figure 3.

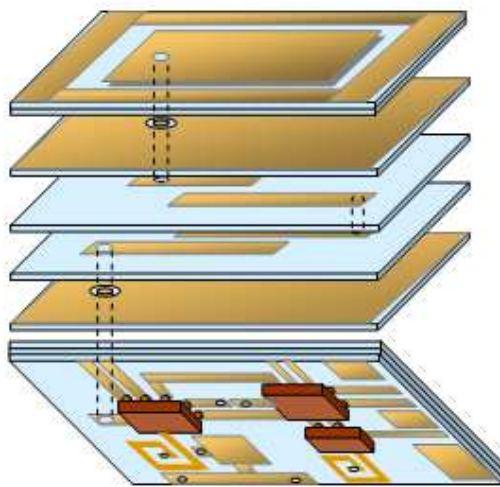


Figure 2. System-in-package exploded pictorial representation.

SoP modules solve the major shortfalls of SoC by providing a low loss substrate material for the RF passives and a unique space saving capability for chip integration in or on the substrate. Connecting these passive and active components on the board and encapsulating the assembly inside of a robust package are two steps critical to reliable operation of

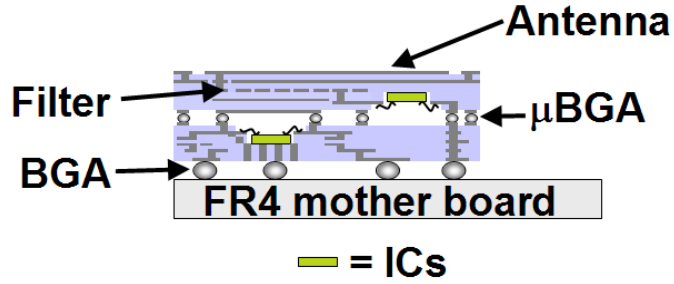


Figure 3. System-in-package side view pictorial representation.

an RF system. The package should create an acceptable environmental seal without significantly affecting the electrical characteristics of the entire circuit. Specifically, the electrical discontinuities created from the package should create minimal reflections and minimal inductive or capacitive parasitics to avoid throwing off the sensitive matching circuits of active devices. The most important material characteristics for use in SoP systems are low electrical loss and excellent seal integrity, generally specified by permeability to moisture and gases.

To examine the motivation for requiring excellent packaging characteristics, the frequency-dependent properties of water must first be examined. Water (which includes environmental humidity) has a natural dielectric relaxation effect that begins after a few GHz in which the water molecule's rotational motion absorbs electromagnetic energy with much greater efficiency (i.e., losses resulting from water absorption go way up) [4]. Figure 4 shows the real and imaginary parts of water's permittivity from 1 GHz to 1 THz as a function of temperature. The real part of the permittivity is the same thing as the relative dielectric constant (ϵ_r), while the imaginary part is known as the loss term.

Microwave engineers are more familiar with loss tangent ($\tan \delta$) than the loss term (ϵ''). The loss tangent is simply a ratio of the loss term and the dielectric constant ($\epsilon' = \epsilon_r$) and is given by (1).

$$\tan \delta = \frac{\epsilon''}{\epsilon'} \quad (1)$$

Focusing first on the loss term (ϵ''), Figure 4 illustrates that that maximum loss (absorption)

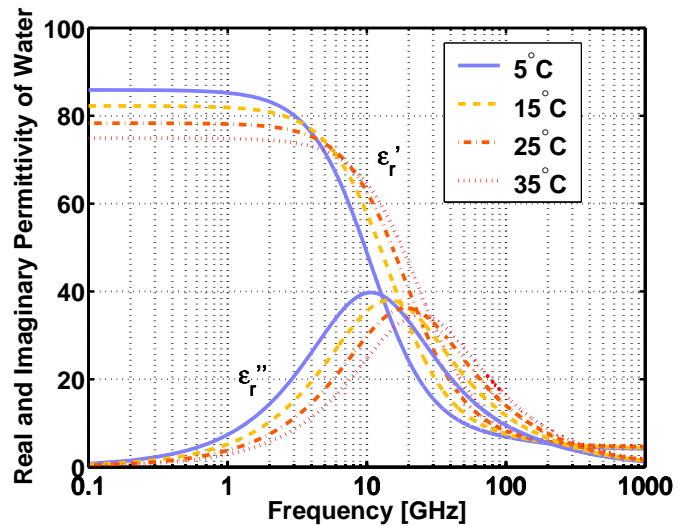


Figure 4. Real (ϵ') and imaginary (ϵ'') parts of the permittivity of water. ϵ' is the same thing as the dielectric constant and ϵ'' is the loss term (not the loss tangent).

of electromagnetic energy by water occurs somewhere between 10 and 20 GHz, depending on the temperature. However, the high dielectric constant of water ~ 80 at the low end of this range makes the value for loss tangent (according to the definition) lower in the 10-20 GHz range than it is at higher frequencies. This is somewhat counterintuitive, as one might expect the peak loss tangent value to occur at the same frequency as the peak of the loss term. The sharp decline in dielectric constant in that same range makes the plot for loss tangent peak anywhere from 40-100 GHz, again depending on temperature. Figure 5 shows the corresponding plot of the dielectric constant and the loss tangent.

Regardless of whether the loss term or the loss tangent is observed as the more important metric, it is easily seen that at frequencies of a few GHz or greater, water becomes highly lossy and it is vitally important to minimize its absorption into RF substrates. For example, a selected high-performance microwave composite (which will go unnamed) with $\epsilon_r = 2.94$, $\tan \delta = 0.0012$, and a water absorption of 0.1% will have an effective loss tangent increase of 147% if it absorbs 0.1% water by weight in the 40–100 GHz range, where water's loss tangent can peak as high as 1.76 (a loss tangent of 1.76 is 1467 times higher than the loss tangent of this test material!). This increase of nearly 2.5x in the effective loss tangent could prove disastrous to an RF system designed with the dry loss tangent in mind.

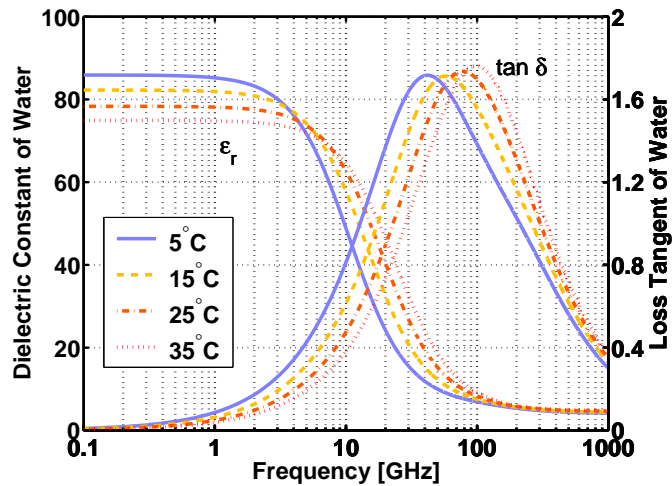


Figure 5. Dielectric constant and loss tangent of water vs. frequency and temperature. A phenomenon called dielectric relaxation occurs in water across the plotted frequency range where the dielectric constant drops from ~ 80 to a value closer to 5 while the loss tangent peaks at 1.76 (880 times higher than a low loss microwave substrate with $\tan \delta = 0.002$) anywhere from 40–100 GHz depending on the temperature.

Current materials used to overcome these water absorption difficulties are advanced microwave composites and ceramics. Both of these material categories have generally excellent electrical performance and very low moisture absorption and transmission, but they can also be relatively expensive.

Microwave composites such as variations of Rogers Duroid or Taconic RF [5, 6] series materials use proprietary mixes of materials like polytetrafluoroethylene (PTFE), glass weave, and ceramic fills. These complicated materials are engineered for excellent performance, but the effort and materials required in their fabrication makes many of them expensive. Alumina is another commonly used ceramic for high frequency applications due to its zero water absorption characteristics. However, alumina's dielectric constant near 10 makes it non-ideal for antenna applications (see explanation below). In addition, alumina has a high thermal coefficient of dielectric constant, which means its dielectric constant changes significantly with temperature (see Figure 26 in chapter 3). This is why network analyzers, which frequently use alumina substrates, are often left turned on continuously – to ensure the dielectric properties of the RF substrates are stabilized. A limitation of these microwave composites and alumina materials is that none are capable of creating

homogeneously laminated compact 3D integrated RF modules. In other words, these microwave boards must use other adhesive materials, which have significantly worse water and gas permeability characteristics, to achieve a compact stacked configuration.

Fully hermetic packaging with microwave boards is often required for military specifications or in satellites, but at much greater financial expense. The term hermetic means that zero water or gas will permeate the package. An example of the standard topology for hermetic packaging for these mission critical applications is shown in Figure 6.



Figure 6. Examples of hermetic metal packages.

At the International Microwave Symposium in 2005, the author spoke with the founder of Thunderline-Z, a leading company for this type of package [7]. The main points noted were that the approximate cost of a single metal package, populated with an RF circuit board is about \$5,000. Brazing or welding is then used to seal a metal lid to the metal box before testing. To certify the package is hermetic, an additional \$15,000 in testing must be performed. The conclusion is that truly hermetic tested RF enclosures may run in the neighborhood of \$20,000 a piece! However, due to metals' interaction with electromagnetic energy, these expensive metal packages cannot be used with the SoP approach, but only as a shielded/packaged solution. In addition, an antenna cannot send or receive through a metal enclosure. As a result, this package type requires an external antenna, and

possibly other components.

Ceramics are the only other material class the author is aware of that is hermetic and used for microwave applications. Ceramics have the unique ability to be laminated into multilayer homogeneous dielectric substrates and packages. Low-temperature co-fired ceramic (LTCC) is the most commonly used ceramic substrate material for compact RF designs. LTCC has very low electrical loss and can be used in multilayer laminated modules that have densely integrated passive and active devices stacked and connected vertically to save space and cost [8]. New advances in ceramics, such as zero-shrinkage LTCC, have enabled the horizontal dimensions of LTCC to stay the nearly the same during firing, which has resulted in more reliable alignment of the layers during and after the firing process. Overall, LTCC is a very attractive material technology, especially for applications that require the greatest functionality in the smallest footprint, such as with wireless handsets. However, as with any material, LTCC has application areas where it is not well suited.

The first limitation of LTCC is due to its 850 °C lamination temperature. This temperature is far above that which destroys active devices. So despite the ability to create hermetic multilayer substrates with densely integrated passive components, the active devices still must be packaged separately and connected after the firing process. The chips often have a plastic or other package topology with wire leads or ball grid arrays for mounting externally or inside cavities in the LTCC stackup. The pre-packaging requirement adds bulk to the assembly and provides some limitations for the number of chips that can be accommodated as well as their placement locations in relation to the passive device layers.

A major drawback to LTCC for antenna applications is its relatively high dielectric constant ($\epsilon_r = 5.9\text{--}9.1$). The high dielectric constant is detrimental to antenna radiation efficiency. Figure 7 shows a comparison of liquid crystal polymer (LCP) and LTCC in terms of radiation efficiency vs. normalized substrate thickness for a microstrip patch antenna [9].

The higher dielectric constant of LTCC results in significantly less efficiency as the substrate height is increased for improving bandwidth. Thicker substrates leak more energy

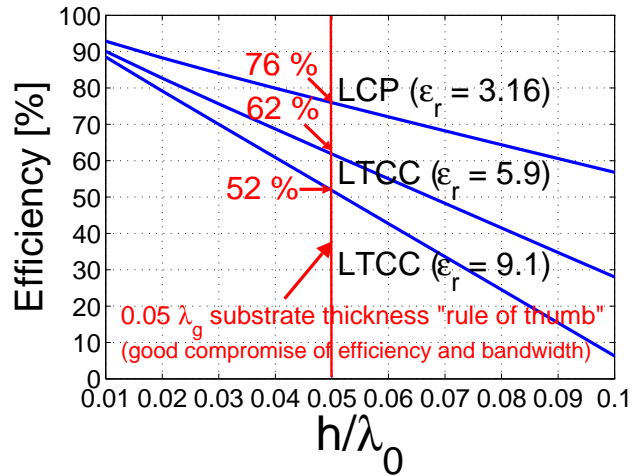


Figure 7. Antenna efficiency vs. normalized substrate thickness for microstrip patch antennas on the minimum and maximum dielectric constants for standard LTCCs and for the dielectric constant of LCP.

into substrate modes or surface waves which decreases the efficiency. However, it is often desirable to maximize antenna bandwidth, so an antenna on a low dielectric constant such as LCP is more useful in obtaining both performance metrics. This comparison is confined to LCP and LTCC since these materials are uniquely capable to provide multilayer RF circuit integration with hermetic or near-hermetic packaging characteristics.

Another limiting consideration for LTCC is that it may not practical to use in applications that require large amounts of horizontal real estate. The manufacturing process is usually limited to 5" x 5" squares and even the largest LTCC foundries have 8" x 8" maximum size capabilities [10]. Also, because LTCC is brittle, it is not desirable for applications that could encounter mechanical shocks or collisions. Finally, the screen printed metallization of LTCC has lower conductivity and higher surface roughness than the electrodeposited or rolled copper of standard microwave circuit boards like LCP. The roughness results from the nature of the screen printing metallization process and the subsequent exposure to the ~850°C firing temperature. This metallization roughness can cause increased conductor losses due to the skin effect, especially at mm-wave frequencies. New types of photodefinable metallization such as Dupont's Fodel® method are helping to make higher

quality LTCC metallization possible. However, the relatively high dielectric constant and brittleness limitations of LTCC should be considered when using it as an antenna substrate.

To understand why large antenna areas may be required, attention should first be given to the free space attenuation of microwaves vs. frequency. Atmospheric absorption increases by several orders of magnitude across the mm-wave band, and as a result, many mm-wave applications may require moderate to large (in comparison to multiples of the wavelength) substrates with many antenna elements to increase the radiation directivity. Figure 8 shows the drastic increase in atmospheric absorption of electromagnetic energy in the mm-wave range and illustrates the importance of efficient directive antennas. The plot includes absorption from moisture and oxygen independently. The total loss is a sum of the two curves, which would further emphasize the drastic absorption increase.

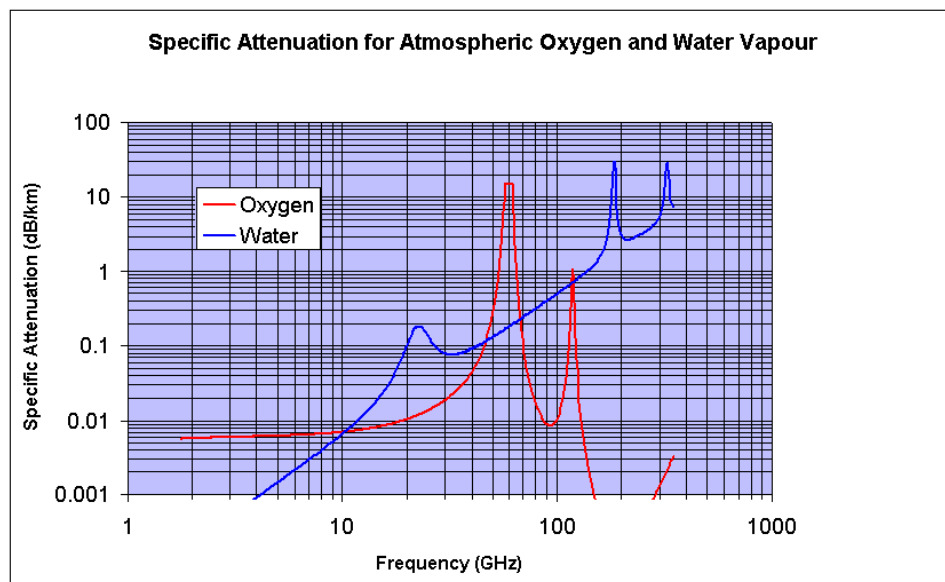


Figure 8. Atmospheric attenuation of electromagnetic energy by water vapor and oxygen as function of frequency. To obtain the total loss these curves must be added to each other.

A tangible example of what this atmospheric absorption means for the antenna requirements follows. One example is 77 GHz collision avoidance radar, which requires antenna beamwidth of 2-3° and gain of around 35 dB [11]. To obtain this gain, a theoretical minimum of 2048 antenna elements would be needed. This assumption is based on a single

patch providing the maximum theoretically possible gain of 7 dB and each doubling of the elements providing an additional 3 dB. Using this methodology, 2048 elements gives an idealized maximum theoretical gain of 37 dB. However, due to several practical implementation factors such as feeding network effects and lowered efficiency from a relatively high dielectric constant substrate, a more realistic array might require 4096 or even 8192 elements. Using the modest assumption of 4096 elements, a 64 x 64 array is required. At 77 GHz, with patch size and spacing of a half guided wavelength on a Ferro A6 (very common) LTCC substrate with $\epsilon_r = 5.9$, this equates to array dimensions of roughly 4.71" x 4.71". These dimensions may not fit a 5" x 5" LTCC process if any significant edge clearance is required. An array on LCP with the same number of elements would be 6.25" x 6.25". The LCP antenna array would not be constrained by fabrication size limitations. Additional LCP benefits include the significantly higher efficiency, the ability to be mechanically conformed, and much more mechanical durability than a large antenna on LTCC.

Thus, for applications like short-range ultra-high bandwidth wireless communications at 60 GHz, for the previously mentioned automotive collision avoidance radar at 77 GHz, or for any application that would benefit from highly directive antenna arrays, a larger substrate area with a low dielectric constant would be beneficial. Some additional applications are for space or air-based imaging arrays and radars. For satellites, antennas on LCP could be deployable in flat panels or rolled out due the mechanical flexibility. Aircraft could also utilize the flexible nature by conforming antenna arrays on LCP to the fuselage or other external surfaces.

The reasons for suggesting LCP as a mm-wave substrate and packaging material is related to the topics of this research. LCP is certainly not the only capable low dielectric constant substrate that can be used for antenna arrays or other microwave applications. However, in evaluating available microwave materials, LCP could be unique in its ability to create near-hermetic homogeneous multilayer dielectric laminations at a temperature

(~285 °C) low enough to potentially package both active and passive devices in compact, vertically integrated RF modules. The environmentally invariant LCP antenna arrays previously discussed could thus have the additional benefit of enclosing all additional RF components in laminated layers below the antenna to create near-hermetic packaged mm-wave systems out of a low-cost polymer material.

These speculations about the potential benefits and uses of LCP were known at the start of this research, and were based on the knowledge that LCP is perhaps the best polymer available in terms of packaging characteristics. However, for real world applications, the feasibility of using a new microwave material like thin-film LCP first requires a thorough investigation into its material properties and process capabilities. For example, the electrical characteristics of a dielectric substrate material can change vs. frequency, temperature, and humidity. In addition, to enable multilayer LCP circuits to be fabricated with both passive and active RF components, special processes must first be established, such as thermocompression bonding, laser processing, and multilayer alignment, among others. The investigations into these and several other practical implementation considerations for utilizing LCP as a mm-wave substrate and packaging material are the topics of this research.

CHAPTER 2

BACKGROUND

LCP has drawn much attention for its outstanding packaging characteristics. A comparison of these packaging characteristics vs. all other polymers is shown in Figure 9. The water and oxygen permeability are presented on a double logarithmic scale. LCP is in the bottom left corner of this plot which corresponds to the location with minimum permeability to both water and oxygen. Low permeability properties are critically important for the stability and reliability of high-frequency electronics built on these dielectric substrates.

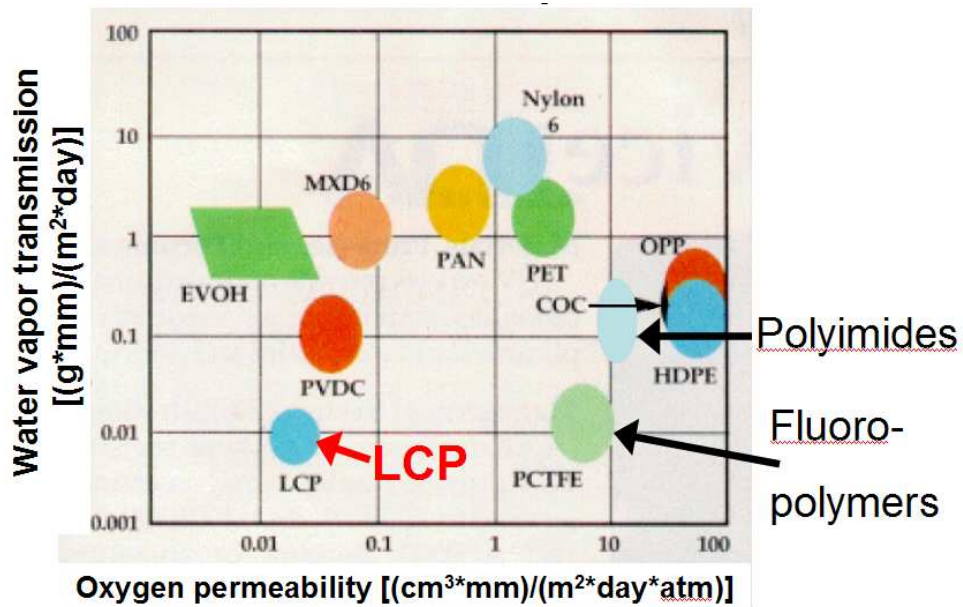


Figure 9. Water and oxygen permeability of different polymer families.

The conclusion from Figure 9 is that LCP is in a class of its own as a polymer in terms of packaging characteristics. LCP has been called near-hermetic and has also been compared to glass in terms of water transmission. And because LCP is a polymer, it has the potential to be much cheaper than ceramics or microwave composites. LCP's combination of being a low-cost material with the best packaging characteristics of any polymer has generated great interest in using it as a dielectric substrate and packaging material for mm-wave applications. Previous literature has described the numerous benefits of LCP [12–14]:

- Excellent high-frequency electrical properties (stable ϵ_r and low loss [$\tan \delta=0.002-0.004$] for $f < 35$ GHz) [15–17],
- Quasi-hermetic (water absorption $< 0.04\%$) [18],
- Low cost ($\sim \$5/\text{ft}^2$ for 2-mil single-clad low-melt LCP) [19],
- Low xy coefficient of thermal expansion (CTE), which may be engineered to match metals or semiconductors,
- Naturally non-flammable (no need to add halogens \Rightarrow environmentally friendly),
- Recyclable,
- Flexible for conformal and/or flex circuit applications,
- Multilayer all-LCP lamination capabilities to create multilayer LCP RF modules,
- Relatively low lamination processing temperature (~ 285 °C),
- Low dielectric constant ($\epsilon_r = 3.16$) for use as an efficient antenna substrate [20].

The use of LCP as a microwave circuit substrate is not a new idea. It has been around in thin-film form since the early 1990s when it was first recognized as a candidate for microwave applications [15, 21, 22]. However, early LCP films would easily tear and were difficult to process. Film uniformity was not acceptable and poor LCP-to-metal adhesion and failure to produce reliable plated through holes (PTHs) in LCP limited the capabilities for manufacturing circuits on it. Devising and optimizing LCP surface treatments and via drilling and de-smearing techniques were also necessary to bring the material to a state where circuits on it could be manufactured with confidence. Much work has focused on methods to improve these fabrication difficulties [23–30].

A biaxial die extrusion process was developed [18, 19, 22], that solved the tearing problems by giving the material uniform strength and also created additional processing benefits. It was discovered that by controlling the angle and rate of LCP extrusion through

the biaxial die, the xy coefficient of thermal expansion (CTE) could be controlled approximately between 0 ppm/°C and 40 ppm/°C. Thus, this unique process can achieve a thermal expansion match in the xy -plane with many commonly used materials. LCP is made commercially with xy CTEs of 17 and 5, the first for matching copper and the second for matching semiconductors. Table 1 shows how the transverse CTE of LCP can be made to match both metals and semiconductors used in high-frequency systems.

Table 1. TRANSVERSE COEFFICIENT OF THERMAL EXPANSION COMPARISON

	LCP	Cu	Au	Si	GaAs	SiGe
CTE (ppm/°C)	0-40	16.8	14.3	4.2	5.8	3.4-5

LCP's z -axis CTE is considerably higher (~ 150 ppm/°C), but because of the thin layers of LCP used, the absolute z -dimension difference between LCP and a 2 mil high copper PTH is less than one micrometer within a 100 °C temperature range [31]. This makes z -axis expansion a minimal concern until very thick multilayer modules come into consideration. It was not until late 2002 that many of the LCP process limitations had been overcome [32], and LCP has only been available commercially in thin films with single and double copper cladding since December 2001 and June 2003, respectively¹. Interest has grown quickly in utilizing LCP for higher frequency applications since then [33], [34].

The start of this research coincides with the time when commercial LCP availability was still in the developmental stage. However, throughout the last several years, LCP as a microwave substrate has become a standard product. The results of this research have been utilized along the way by the materials supplier(s) in demonstrating the RF characteristics and capabilities of the LCP material. The investigation of LCP mm-wave electrical properties, multilayer circuit enabling processes, and demonstrations of novel high-frequency packaging structures are the desired contributions of this research.

Specifically, the research performed includes the following:

¹Rogers Corporation, Rogers, CT. [Online]. Available: <http://www.rogerscorporation.com/whatsnew.htm>

- Determination of LCP's electrical properties up to mm-wave frequencies, and finding the material's dielectric sensitivity to elevated temperature and humidity conditions over the same frequency range.
- Developing a multilayer LCP process with thermocompression bonding, alignment, and laser micromachining to enable the 3D integration of RF components into multilayer LCP packaged structures.
- Evaluating the flexibility characteristics of conformal and/or rollable antennas on LCP substrates.
- Creating and evaluating novel LCP packaging structures including
 - A package interconnect for feeding RF transmission lines through package interfaces.
 - Thin-film LCP packages for RF MEMS and MMICs.

The objective will be to determine the feasibility and performance expectations of using LCP for multilayer, low-cost, reconfigurable mm-wave RF front-ends and modules.

CHAPTER 3

INVESTIGATION OF LCP MM-WAVE DIELECTRIC PROPERTIES

To ensure that LCP can be used as a low-cost material for use as a high-frequency substrate and packaging material, its mm-wave electrical properties must first be proven sufficiently attractive through the frequency range it is desired for use. Thus, the first investigation involved the design, fabrication, and testing of resonant circuits and the use of resonant cavities for accurate broadband (2–110 GHz) extraction of the dielectric constant and loss tangent. In addition to the ambient dielectric characteristics, the sensitivity of LCP's dielectric constant to temperature changes were also investigated. The dielectric temperature stability is important for maintaining the desired operating characteristics in hot environments or for high power circuits that are expected to experience significant heating.

3.1 mm-Wave Dielectric Characterization

Previous literature [15–17] has focused on lower-frequency characterization of LCP using microstrip ring resonators to extract ϵ_r and $\tan \delta$ up to 34.5 GHz. This existing knowledge of LCP's promising electrical performance only provided information on the dielectric constant and loss tangent up to the beginning of the mm-wave range. But as seen with water, these values do not always stay the same with changes in frequency. In addition, broadband dielectric material characterization at mm-wave frequencies creates several non-trivial measurement problems. At these high frequencies the skin depth approaches the metal surface roughness of a printed resonator's traces and the radiation effects from microstrip transmission lines can become significant. Thus, techniques had to be developed to minimize these uncertainties.

In this research, accurate broadband dielectric properties (ϵ_r , $\tan \delta$) of LCP for frequencies from 30 to 110 GHz have been obtained for the first time. Microstrip ring resonators

of varying diameters and substrate thicknesses have been used in conjunction with cavity resonators, and the methods cross-referenced in order to provide certainty of the results.

In addition, the losses per unit length of conductor-backed coplanar waveguides (CB-CPWs), coplanar waveguides (CPWs), and microstrip lines, each on varying substrate thicknesses, have been characterized for the first time from 2 to 110 GHz and the results quantified in decibels per centimeter (dB/cm). The transmission line losses across the mm-wave range provide a design guide for loss versus frequency of circuits built on LCP substrates. The results of this investigation give a thorough knowledge of LCP dielectric properties and the performance of LCP-based circuits up to mm-wave frequencies.

3.1.1 Ring Resonator Method

Ring resonators provide dielectric information at discrete points at the periodic resonant frequency peaks in an S_{21} measurement. The extraction of ϵ_r is dependent on the resonant frequencies for a resonator of a given radius, while the extracted $\tan \delta$ is a function of the quality factor (Q) of the peaks. For each substrate thickness, the desired resonant peaks and corresponding ring radii were devised according to (2)

$$f_0 = \frac{nc}{2\pi r_m \sqrt{\epsilon_{eff}}} \quad (2)$$

where f_0 corresponds to the n th resonant frequency of a ring with mean radius r_m , effective dielectric constant ϵ_{eff} , and c being the speed of light in vacuum [16], [35]. A computer aided drawing of a general ring resonator configuration is shown in Figure 10.

To ensure the results obtained were not sensitive to the number of resonances used, small and large ring diameters were employed for each substrate thickness. The small ring was designed for approximately five resonant peaks and the large one for about ten peaks across the 2-110 GHz measured frequency range. A standard microstrip feed could not be used due to the cutoff of most coaxial connectors at 50 GHz. Thus, CB-CPW-to-microstrip transitions were included on both ends of the ring resonators so that on-wafer

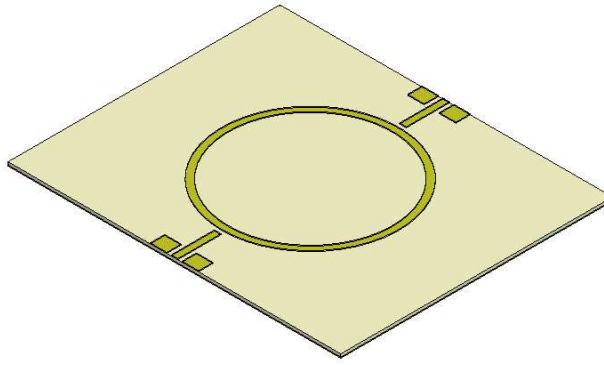


Figure 10. CAD drawing of ring resonator configuration with CB-CPW to microstrip transitions.

probes rated to 110 GHz could be utilized. The transitions were optimized for frequencies above 30 GHz.

To minimize radiation losses and dispersion (impedance change vs. frequency) in the microstrip lines, high-impedance lines are desirable [36], [37]. Thus, microstrip and CB-CPW lines were chosen in a range between 60–90 Ω .

Six slightly varying ring resonator configurations were designed using Ansoft HFSS and Flomerics Microstrips on varying substrate thicknesses and using different coupling gaps, line widths, and ring radii. The multiple designs were used to ensure that the results were not influenced by slight design variations. The final designs for the ring resonators, including their feeding transitions, are shown in Table 2.

Table 2. RING RESONATOR CONFIGURATIONS. NOTE: ALL DIMENSIONS ARE IN MICROMETERS, EXCEPT FOR ‘h,’ WHICH IS IN MILS

Ring Resonator	Ring Resonator			CB-CPW					Microstrip	
	h	r_m	G	S	W	W_g	TL	L	W	L
A	3	1477	80	104	85	276	0	250	104	500
B	3	2947	70	104	85	276	0	250	104	500
C	5	1477	80	104	85	276	0	250	104	500
D	5	2947	70	104	85	276	0	250	104	500
E	5	2683	185	196	85	506	100	150	234	500
F	5	2954	185	196	85	506	100	150	234	500

Dimension nomenclature designations for the transmission line cross sections and ring resonator layout are shown in Figures 11 and 12.

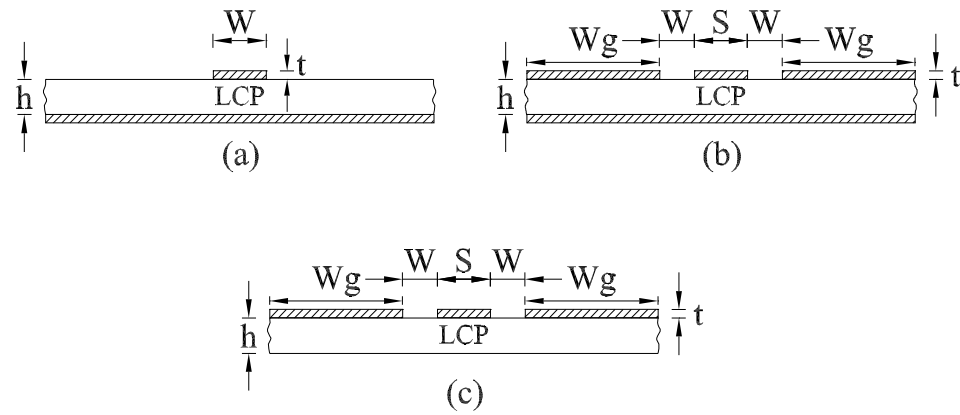


Figure 11. Transmission-line cross sections for: (a) microstrip, (b) CB-CPW, and (c) CPW.

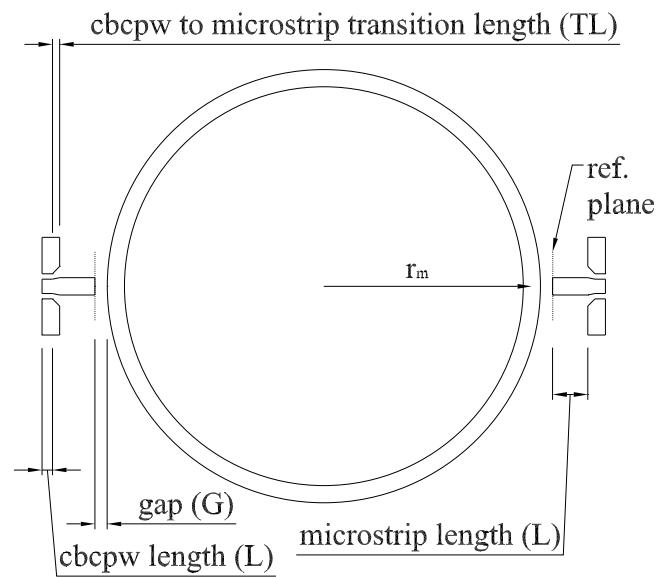


Figure 12. Microstrip ring resonator configuration diagram.

As shown in Table 3, designs A, B, E, and F have closely matched CB-CPW-to-microstrip impedances, while designs C and D were mismatched to provide a higher impedance for the microstrip portion. The impedances were calculated with the HP ADS LineCalc software utility using the fabricated dimensions and assuming the manufacturers specification of

$\epsilon_r = 2.9$. Slight mismatches in the design were due to a combination of factors. The probe pitch for the GSG probes gave dimensional limitations for the S+2W of the CB-CPW, and depending on the substrate thickness, the signal width for CB-CPW and microstrip lines of the same impedance were sometimes difficult to match. Thus a tapered $100 \mu\text{m}$ transition section was used in some designs. The etching undercut during fabrication also played a role in the final dimensions. The dimensions shown in Table 2 are those measured from the fabricated structures. The microstrip impedances have been taken near the middle of the frequency range (at 60 GHz) due to the $\sim 2 \Omega$ variation in calculated microstrip impedance between 30 and 110 GHz.

Table 3. RING RESONATOR IMPEDANCES

	CB-CPW [Ω]	Microstrip [Ω]
A, B	68	71
C, D	80	90
E, F	60	61

To remove the effects of the feeding sections and eliminate the effects of the slight impedance mismatch, a through-reflect-line (TRL) calibration was performed with six delay lines, a through, and an open reflect. HP BASIC and the National Institute of Standards and Technology (NIST) Multical software were used in the calibration [38]. A reference plane was set at the edge of the coupling gap to the resonator so that only the response of the resonating ring element (a microstrip ring) was effectively measured. The TRL lines lengths used in the calibration are shown in Table 4.

The double copper clad LCP substrates from Rogers Corporation were inspected with a Wyko optical profilometer and the $18 \mu\text{m}$ of electrodeposited copper showed $0.4\text{--}0.6 \mu\text{m}$ root-mean-square (rms) surface roughness. Unfortunately, accurate loss tangent extraction using the ring resonator method requires reliable theoretical equations for microstrip conductor losses. With the surface roughness potentially approaching the copper skin depth

Table 4. TRL LINES USED IN CB-CPW-TO-MICROSTRIP TRANSITIONS

TRL Lines	Total Length [cm]
Delay 1	1.1924
Delay 2	0.4590
Delay 3	0.2436
Delay 4	0.1838
Delay 5	0.1653
Delay 6	0.1535
Through	0.1000
Reflect Open	0.0500

as low as 12 GHz, an undesirably large surface roughness correction factor would be required in the conductor loss formulas for frequencies above 30 GHz. As a solution, the 18 μm copper was etched off of one side of 2 and 4 mil high-melt temperature LCP core layers. A Karl Suss SB-6 wafer bonder was used to bond a smooth 5 μm rolled copper foil to the bare 2 and 4 mil LCP surfaces with a 1 mil low melting temperature LCP layer as the bond layer. As a result of this process modification, the ensuing ring resonators were patterned on 3 and 5 mil LCP substrates. The bonded construction is assumed electrically homogeneous since identical electrical characteristics are listed for high and low melting temperature LCP. Depending on the orientation to the rolled foil's copper grain structure, its rms surface roughness measured between 0.1–0.35 μm . With these values, the surface roughness reaches the copper skin depth at the worst case near 36 GHz, while at the moderate to best case, the roughness would not approach the skin depth until well after 110 GHz. Figure 13 shows some ring resonators and TRL calibration lines fabricated on the smooth bonded 5 μm rolled copper foil.

The measurements were done over a 2-110 GHz band using an Agilent 8510XF vector network analyzer (VNA) and Cascade Microtech 250 μm probe pitch ground-signal-ground (GSG) 110 GHz probes. The maximum number of frequency points (801) and an averaging factor of 128 were used in the measurement. The 3 dB bandwidth of the resonant peaks was found to be roughly one hundredth of each peak's center frequency. Thus the 3 dB

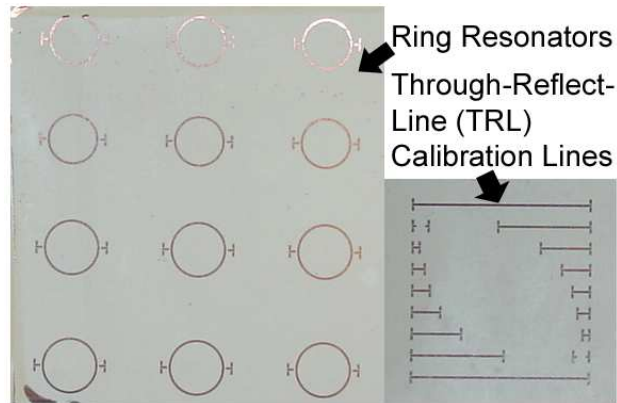


Figure 13. Fabricated ring resonators and TRL calibration lines on 5 mil LCP. A 1 mil low melting temperature LCP bond layer was used to affix a 5 μm smooth copper foil to avoid losses due to conductor surface roughness above 30 GHz.

bandwidth was around 300 MHz for a 30 GHz peak and near 1 GHz for a 100 GHz peak. The measured data points were 135 MHz apart, but post processing interpolation using MATLAB with an interpolation factor of 15 gave frequency resolution of about 10 MHz.

A test was applied to determine if the accuracy of this interpolation method was sufficient. A TRL calibration and re-measurement of a known resonant peak was performed using 801 data points over a 4 GHz band. The results with this 5 MHz resolution were identical to that using more sparse data points and interpolation. Following this test, the rest of the measurements were done using the broadband measurement with data interpolation. One such measurement file is shown in Figure 14.

ϵ_{eff} and ϵ_r both are obtained using the equations found in [17]. Depending on the geometry, different numbers of resonant peaks were discernable for different designs. Only clearly defined resonant peaks were evaluated. The dielectric constant results vary by less than 2.6% between the six resonator designs in any 10 GHz frequency band and less than 4.3% over the entire 80 GHz band. The results of LCP's broadband dielectric constant from the ring resonator measurements are shown in Figure 15. Also seen in this figure are the results from the alternative cavity resonator method, which will be discussed in the next section. The extracted dielectric constant from the two methods match well.

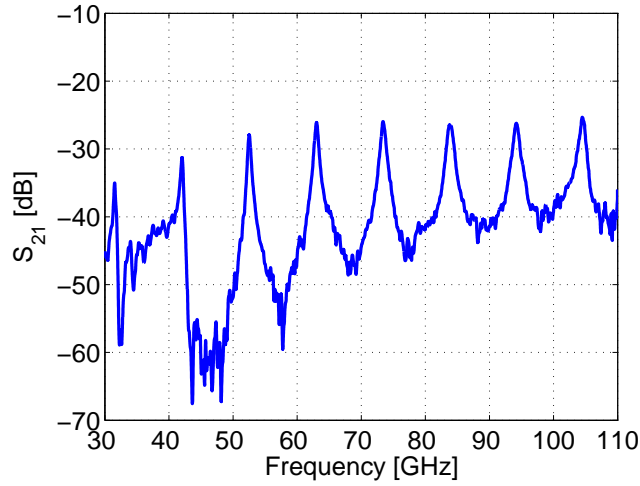


Figure 14. S_{21} measurement for ring resonator configuration D.

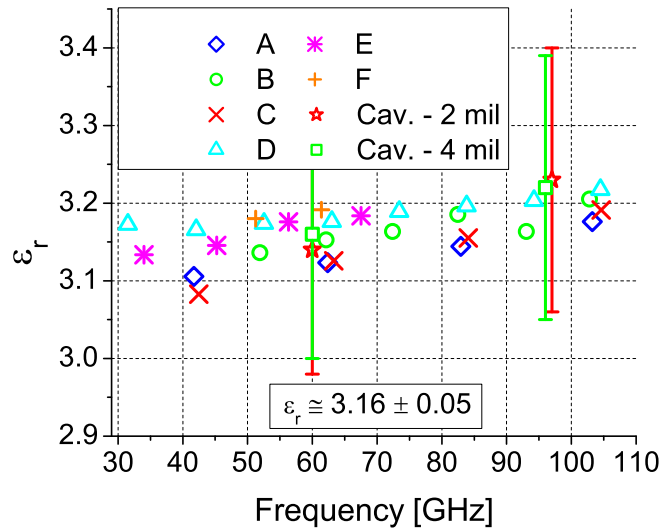


Figure 15. Extracted dielectric constant using ring resonator designs A through F and cavity resonators with 2 and 4 mil LCP.

The results show approximately that $\epsilon_r = 3.16 \pm 0.05$ with a slight increase with increasing frequency. The lowest value observed was 3.083 and the highest was 3.217, but a majority of the data points fell closer to the high end of this range. In data point groupings near 43, 62, and 104 GHz, the approximate average values are 3.13, 3.15, and 3.19, respectively. These stable dielectric constant results are important for establishing LCP as a material that can be used for designs at frequencies across the mm-wave frequency spectrum.

The extraction of loss tangent using the ring resonator at such high frequencies is more difficult. The ring resonator method gives the total loss at the frequency locations of each resonant peak [16], and subtracting theoretical values for conductor and radiation losses is required to isolate the dielectric loss (α_d). α_d in nepers per meter may then be inserted into 3 to obtain the results for loss tangent [39].

$$\tan \delta = \frac{\alpha_d \lambda_0 \sqrt{\epsilon_{eff}} (\epsilon_r - 1)}{\pi \epsilon_r (\epsilon_{eff} - 1)} \quad (3)$$

where λ_0 is the free-space wavelength, ϵ_{eff} is the effective dielectric constant, and ϵ_r is the relative dielectric constant.

Accurate theoretical equations for both conductor and radiation losses are a necessity for extracting $\tan \delta$ using the microstrip ring resonator method. However, available conductor loss [40–43] and radiation loss [42–44] formulas are dated from the 1970’s or before and were not meant for describing microstrip characteristics in the tens or hundreds of GHz. To the author’s knowledge, no analytical formulas are available which are optimized for describing conductor and radiation losses in a microstrip line from 30 to 110 GHz.

Four microstrip conductor loss formulas were investigated and found to differ significantly. As an example, the theoretical conductor losses on the microstrip geometry on 3 mil LCP differed by about 0.74 dB/cm at 110 GHz from highest [44] to lowest [43]. The conductor loss equation used in a previous LCP material characterization [17] was found to use an incorrect formula for conductor loss [40], which was later corrected in [41]. This would lead to an artificially high extracted loss tangent, which could explain why values for $\tan \delta$ similar to 0.0038 were reported at 10 GHz, while 0.002-0.003 are the values at 10 GHz reported by LCP suppliers Rogers Corporation and W.L. Gore respectively. Sorting out the available theoretical formulas, the combination which gave us reasonable values for extracted loss tangent came from [43] for conductor loss and using 0.35 μm (max. measured) for our rms surface roughness.

Two of the three radiation loss formulas tested [43,44], including the one used in [17],

give radiation loss curves with unreasonable f^2 increases at frequencies past 30 GHz. In fact, the theoretical radiation losses from these equations give values higher than the total measured loss past about 80 GHz. The third radiation loss formula, found in [42] (originally from [45]), is the only one tested that did not diverge to unreasonable levels in the measured frequency band, and it is used in the analysis. The loss tangent is plotted in Figure 16 with and without subtracting the radiation loss for an open ended microstrip from [45]. This radiation loss was multiplied by a factor of two to account for the two discontinuities. Radiation from the ring element is assumed negligible and has been neglected in the calculation. The ring resonator plot with the radiation losses subtracted gives a good approximation of the values found by the cavity resonator method. It shows values between 0.003-0.004 with the exception of one outlier near 93 GHz.

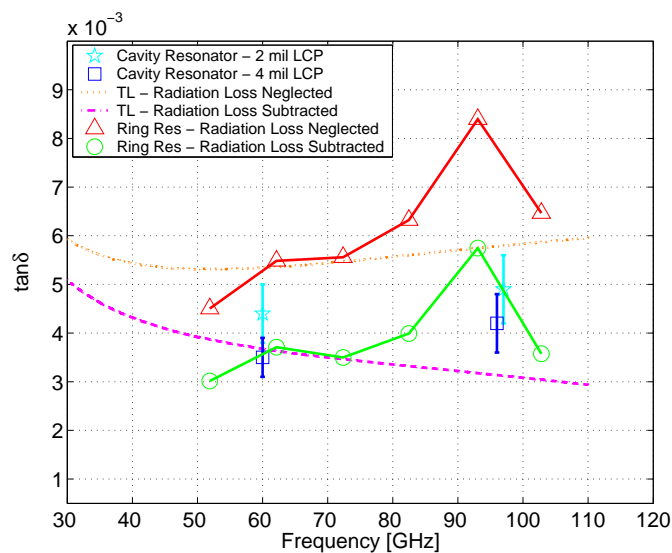


Figure 16. LCP loss tangent versus frequency for 2 and 4 mil substrate thicknesses measured with the cavity resonator method. Results for the ring resonator method and the transmission line (TL) method on 3 mil LCP substrates are shown with and without subtracting radiation loss. The values extracted from the cavity resonator method are the benchmark for accuracy due to the much higher Q -factor of the the resonant cavity topology.

3.1.2 Cavity Resonator Method

With the aim of verifying the dielectric properties measured by other methods, a resonant cavity method has been used for permittivity and loss tangent measurements. This technique permits an accurate measurement without preparation of the sample (no cutting, polishing, or metallization) and it avoids any important theoretical approximations. These cavity resonator measurements were carried out in collaboration with the National Institute of Standards and Technology (NIST), Boulder, CO, and the University of Limoges, Limoges, France. A picture of the cavity resonators is shown in Figure 17.

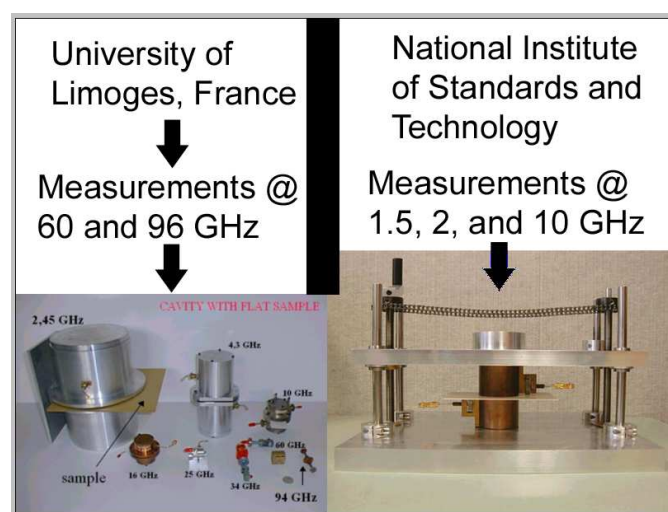


Figure 17. Cavity resonators used in collaboration with the University of Limoges, France, and NIST, Boulder, CO.

The cavity resonator measurement involves measuring the cavity's resonant frequency and Q -factor with the cavity empty and then with a sample inserted between the two split-cylinder resonator sections. By measuring the shift in resonant frequency and the new measured Q of the cavity, the dielectric constant and loss tangent may be extracted with very good accuracy. The resonator Q is defined as the resonant peak center frequency divided by its 3 dB bandwidth. In this extraction process, correction factors are applied to take into account the cavity dimension change from inserting the substrate and also to account for fringing fields at the gap. The following description of the cavity resonator measurement methodology is written in terms of the 60 GHz and 96 GHz cavities. However, the same

techniques are valid for the 2 GHz and 10 GHz cavity resonator measurements made by NIST.

The sample is inserted between the two halves of a cylindrical cavity excited in $TE_{01,2q+1}$ the mode. The interior diameter of the cavity determines the frequency band in which, for a given sample, the measurements can be made. Two cavities with resonant frequencies near 60 and 96 GHz have been used.

Using two of the $TE_{01,1or3or5}$ modes, the electrical field is parallel to the dielectric plane and has negligible (practical zero) values close to the gap between the dielectric specimen and the wall of the cavity. The horizontal dimensions of the substrate must be chosen higher than the interior diameter (ϕ_c) of the cavity ($\phi_c = 7.8$ mm at 60 GHz and 5 mm at 96 GHz) and the thickness less than 0.5 mm at 60 GHz and 0.3 mm at 96 GHz to minimize the radiation in the gap between the two halves of the cavity. In such a configuration, the resonant frequency and the quality factor of the $TE_{01,2q+1}$ mode can be computed exactly. Thanks to an iterative computation, the complex permittivity of the sample can be extracted from the resonant frequency and quality factor. First, the measurement with a VNA of the resonant frequencies of two $TE_{01,2q+1}$ modes (TE_{013} and TE_{015} for example) is necessary to adjust the interior dimensions of the cavity taken into account during computations. The loaded quality factor of one of these modes is used to compute the power losses due to the metallic walls. Then, only the measurement of the resonant frequency and of the loaded quality factor of the cavity loaded with sample is necessary to determine the permittivity and the loss tangent of the substrate [46]. The uncertainties of the quality factors, the resonant frequencies and the coupling (through $|S_{21}|$ at the resonant frequency) are reflected in the uncertainties shown for ϵ_r and $\tan \delta$ of the 2 and 4 mil LCP substrates (Figure 15 and Figure 18). The error tolerances are due to uncertainties on the cavity dimensions Δr on radius and ΔH on the height), and on the uncertainty of the sample thickness, Δd .

The cavity ϵ_r results match those of the ring resonators well within the cavity measurements error tolerance. In regards to $\tan \delta$, the cavity resonator results are the benchmark for

accuracy. The values for $\tan \delta$ fall between 0.0035–0.0045 at 60 GHz and 0.0042-0.0049 near 96 GHz.

In addition to the mm-wave (60 and 96 GHz) cavity resonator measurements, cavity resonator measurements performed with the assistance of NIST at 1.5, 2 and 10 GHz are included in Figure 18 to cover the frequency range from 1.5 to 96 GHz. Since the cavity resonator results for loss tangent are the most accurate method, this plot is provided independently of the extracted ring resonator loss tangent data.

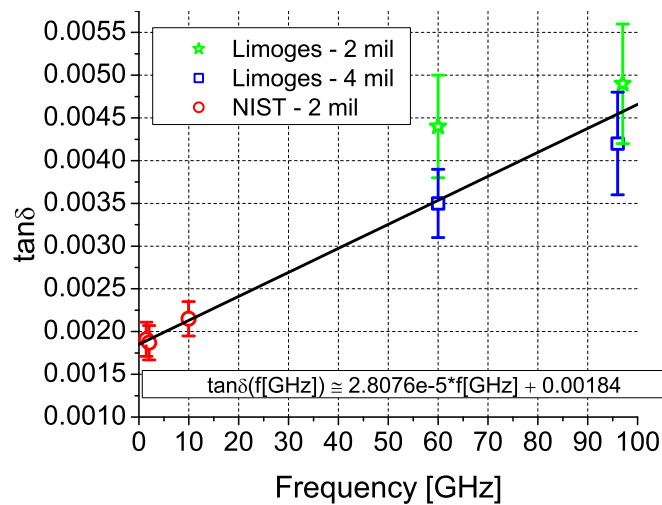


Figure 18. LCP loss tangent versus frequency for 2 and 4 mil substrate thicknesses measured with the cavity resonator method.

A linear fit equation is included in the figure to match the frequency dependent loss tangent. This equation is a useful result of this research that can be used to determine the loss tangent value in LCP circuit designs from 1 GHz to over 100 GHz. LCP becomes more lossy with increasing frequency, but the loss value is still relatively low across the mm-wave frequency spectrum.

3.1.3 Transmission Line Method

Instead of using a ring resonator for the extraction of total loss, a TRL transmission line calibration can be used to provide the total loss for use in loss tangent extraction. However, instead of measuring the loss data at widely spaced resonant frequencies, the TRL total

loss is at every frequency point in the calibration. The theoretical conductor and radiation losses can be subtracted by curve matching the total loss plot with a smoothed spline and using the same method as described above. The dielectric loss can then be inserted into (3) to retrieve the loss tangent.

As seen previously in Figure 16, the loss tangent values from the transmission line method settle close to the range defined with the cavity and ring resonators. However, a higher value than expected is seen at the lower end of the measured frequency range and a slight decrease in loss tangent is observed in the case where radiation losses are subtracted. The discrepancies are likely due to the approximations in conductor and radiation losses. Despite this, the loss tangent for either line in the transmission line method do not vary by more than 0.002 over the 80 GHz band of measurement (30-110 GHz) and the plot with radiation loss subtracted is a good indicator of the magnitude of dielectric loss. However, this method is the least accurate of the three for determining mm-wave loss tangent. The cavity resonator results and linear fit equation provided represent the true broadband loss tangent values of LCP.

3.1.4 Summary of LCP mm-wave Dielectric Properties

A summary of previous LCP material characterization, as well as that extended by this research, are shown in Table 5. In this table, the average loss tangent values for the cavity resonator measurements of the 2 and 4 mil thick LCP substrates are shown. The values measured for ϵ_r are slightly higher than the others shown in Table 5. However, the frequency range tested in this research is higher and it is shown above that ϵ_r for LCP may increase slightly with frequency. If a linear regression is fitted through the data in Figure 15 with a slope of 0.12%, the data in this research would predict an ϵ_r of 3.1 at 10 GHz, which agrees well with the reported values. Furthermore, the measured value of ϵ_r at 30 GHz, i.e., 3.12, in this research agrees with the value in [15], but whereas the wide-band measurements in this research show an increase in ϵ_r with frequency, the narrow-band measurements in [15] predict no frequency dependence. To test the sensitivity of the results

to the listed LCP substrate thickness tolerance of 10%, an investigation in the calculation of ϵ_r was performed. This modification resulted in only a small change of the extracted ϵ_r by ± 0.02 . The loss tangent values shown in Table 5 from this research are higher than those previously reported, but again, the loss tangent is shown in Figure 18 to be frequency dependent.

Table 5. SUMMARY OF REPORTED LCP MATERIAL PROPERTIES

Source	f [GHz]	ϵ_r	$\tan \delta [10^{-3}]$
Rogers	10	2.9	2
W. L. Gore	10	3.0	3
[15]	6.97 - 34.66	3.07 - 3.18	-
[16]	3.85 - 34.45	3.00 - 3.04	3.4 - 2.7
This research	31.53 - 104.60	3.16 ± 0.05	4 at 60 GHz, 4.5 at 96 GHz*
*The following LCP loss tangent equation was determined from this research: $\tan \delta(f[\text{GHz}]) \approx 2.8076e-5 * f[\text{GHz}] + 0.00184$			

Broadband ϵ_r extraction was found to be reliable using both ring and cavity resonators, but the cavity resonator measurement is the most accurate for loss tangent extraction at mm-wave frequencies.

The frequency dependent loss tangent from 2–110 GHz was extracted from measurements and follows equation (4)

$$\tan \delta(f[\text{GHz}]) \approx 2.8076e - 5 * f[\text{GHz}] + 0.00184 \quad (4)$$

This equation can be used to determine LCP's loss tangent for any desired frequency in the range investigated.

3.1.5 Transmission Line mm-wave Loss Characteristics

Three of the most common transmission line types used in microwave circuits are microstrips, coplanar waveguides (CPWs), and conductor-backed coplanar waveguides (CB-CPWs). When designing RF circuits, electromagnetic simulators are generally used, with the assumption that the metals are perfect electrical conductors (PEC) and have no metal

loss. Even when a conductivity value is added to the simulation, simulated transmission lines do not take into effect metal surface roughness. At low frequencies this may be okay, but for mm-wave structures, the skin depth becomes very small ($\sim 0.2 \mu\text{m}$ @ 100 GHz), and this can create significant real-world conductor losses that are not detected in simulation. To create a guide for RF circuit designers using LCP substrates, all three transmission line types have been measured on varying substrate thicknesses with the standard copper metallization from the manufacturer and attenuation vs. frequency given from 2–110 GHz for the first time.

All transmission line measurements were done by performing measurements with the NIST TRL standard and using between 4-6 delay lines. The same hardware and software as above was used for all measurements. The loss per unit length is one of the parameters directly extracted by the NIST Multical software from comparing attenuation values between the different line lengths.

3.1.5.1 Conductor-backed Coplanar Waveguide Transmission Lines

CB-CPWs were designed and fabricated on 2, 4, and 8 mil LCP substrates. An important consideration for the design of CB-CPWs is that a parasitic parallel-plate waveguide mode is excited when the total width of the transmission line ($S + 2*W + 2*W_g$) is greater than $\lambda_g/2$. The measurements shown in Figure 19 demonstrate this effect beginning at about 80 GHz for the transmission line on the 8 mil substrate.

Table 6 documents the measured transmission line dimensions, calculated line impedances from the ADS LineCalc utility using the fabricated dimensions, and the peak attenuation values observed at 110 GHz. The measured line dimensions were slightly affected by the etching undercut, which at this stage of research was not being compensated for on the mask.

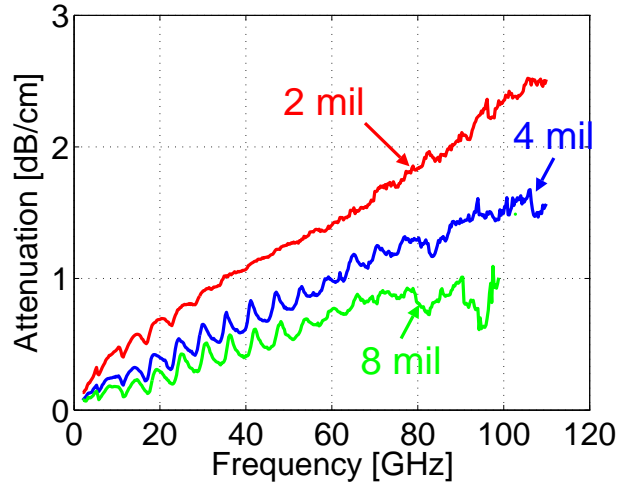


Figure 19. CB-CPW line losses on 2-8 mil LCP substrate thicknesses.

Table 6. CB-CPW TRANSMISSION LINES: LINE GEOMETRIES AND PEAK LOSSES.

h: substrate height, S: signal width, W: gap width, W_g : gnd width						
h [mil]	S [μm]	W [μm]	W_g [μm]	Z_0 [Ω]	Sets Meas.	Attn. at 110 GHz [dB/cm]
2	104	148	290	55	1	2.51
4	189	104	501	53	1	1.54
8	253	72	662	55	1	0.85*
*Value at 80 GHz. The parallel-plate waveguide mode interfered with this measurement above 80 GHz.						

3.1.5.2 Coplanar Waveguide Transmission Lines

CPWs do not have a backside ground plane, but are assumed to have an electrically infinite distance of free space beneath the substrate. However, when performing on-wafer measurements, the sample is usually forced to be in contact with a metal chuck. To overcome this limitation, an electrically thick dielectric spacer must be used between the CPW and chuck. Initially the measurements were tried on a piece of foam poster board, then on a piece of internally corrugated hollow plastic, and finally on a low-loss dielectric spacer from Cuming Microwave, Avon, MA. All of the spacers were from 1/8" to 3/16" thick. Simulations calculated this thickness to effectively isolate the CPW from the chuck metalization, thus avoiding parasitic microstrip moding. The low-loss dielectric spacer is called

C-Stock RH-5, which has $\epsilon_r = 1.09$ and $\tan \delta = 0.0004$ at 5 GHz. For each different spacer, interesting phenomena arose that warranted further testing. Together the three are able to accurately characterize the expected performance of CPW lines.

Due to LCPs low dielectric constant, 50 Ω CPW lines require signal widths and gap widths far too large to measure with 110 GHz probes. The dimensions selected are based on the probe pitch and on easily fabricated line widths and gap widths. The resulting impedances are in the range near 80 Ω . A summary of the circuits measured and the peak attenuation values are shown in Table 7.

Table 7. CPW CONFIGURATIONS MEASURED. LPB=LOSSY POSTER BOARD; HP=HOLLOW PLASTIC; LLF=LOW LOSS FOAM

h [mil]	S [μm]	W [μm]	W_g [μm]	Z_0 [Ω]	Type of Dielectric Spacer	Sets Meas.	Attn. at 110 GHz [dB/cm]
2	221	91	591	83	LPB	1	2.06
4	209	98	561	81	LPB	1	1.80
8	193	104	520	80	LPB	1	1.52
2	221	91	591	83	HP	2	0.96
4	209	98	561	81	HP	2	1.11
8	193	104	520	80	HP	2	1.19
2	221	91	591	83	LLF	3	0.88
4	209	98	561	81	LLF	3	1.08
8	193	104	520	80	LLF	3	1.04

Measuring the CPW lines on the lossy poster board gave the cleanest attenuation curves, but it resulted in inaccurately high attenuation values. The results are shown in Figure 20. In addition, the lines on the thinnest LCP substrate (2 mil) had the greatest loss since this is the configuration that allows the greatest amount of field interaction with the lossy spacer below. Ideally, with a lossless spacer, the 2 mil substrate should be the configuration with the least loss since it would have the least interaction with the LCP substrate and more field lines passing through “free space” on the underside.

The hollow plastic spacer measurements show significantly lower loss in Figure 21, but large oscillations are seen in the extracted loss data past 70 GHz. The structure of

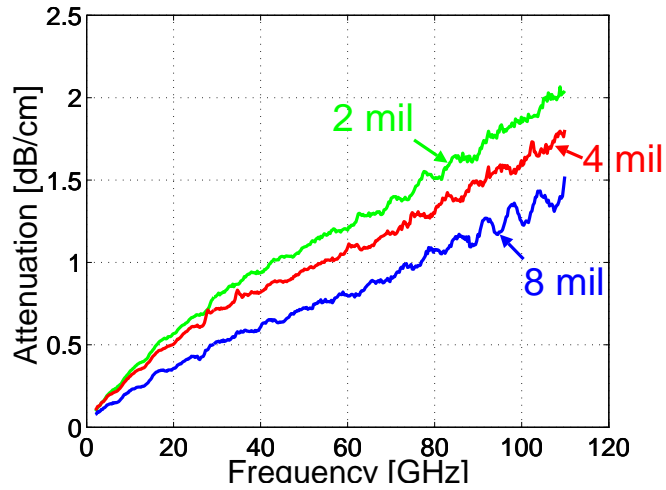


Figure 20. CPW total measured loss on a lossy poster-board spacer.

the spacer has waveguide-shaped dielectric channels beneath the thin plastic surface. The dimensions of these channels are consistent with a waveguide cutoff frequency near where the oscillations begin to occur. It is expected that these channels could have supported dielectric waveguide modes, resulting in the oscillatory responses shown. However, the loss trend is still easily deciphered and the peak loss level at 110 GHz has values below 1.2 dB/cm.

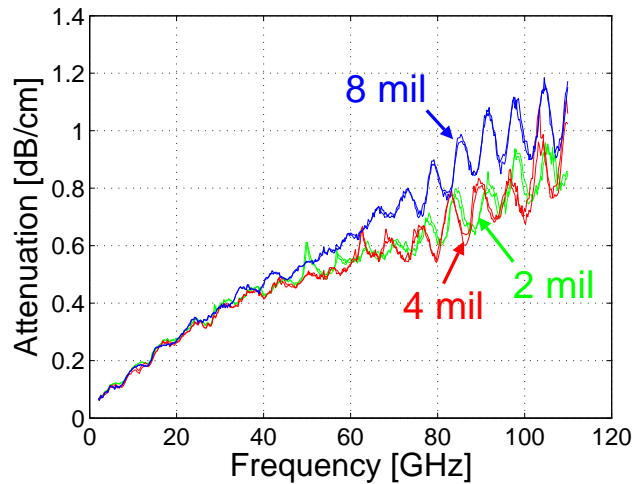


Figure 21. CPW total measured loss on a hollow plastic spacer.

The low-loss foam spacer in Figure 22 shows considerable more jitter, a flattening of

attenuation in the 40-70 GHz range, and almost indistinguishable attenuation levels between the three substrate thicknesses. The jitter in the measurement can be explained by the surface of the spacer. It is a rigid, but very porous surface that is not uniform or homogenous. The size of the foam cells are on the order of the size of the transmission-line features, which introduces foam cell boundaries to the transmission line along its entire length. Though it performs very well in overall loss levels, the porous surface makes tidy loss plots impossible. The close bunching of the loss characteristics shows that there is minimal interaction with lossy material beneath the LCP. The results identify that CPW lines on LCP are capable of peaking with loss less than 1 dB/cm up to 110 GHz. The CPW attenuation results on the low-loss foam spacer should be used as the true indicator of transmission line loss on LCP since the low-loss foam measurement gives the best representation of free-space beneath the sample.

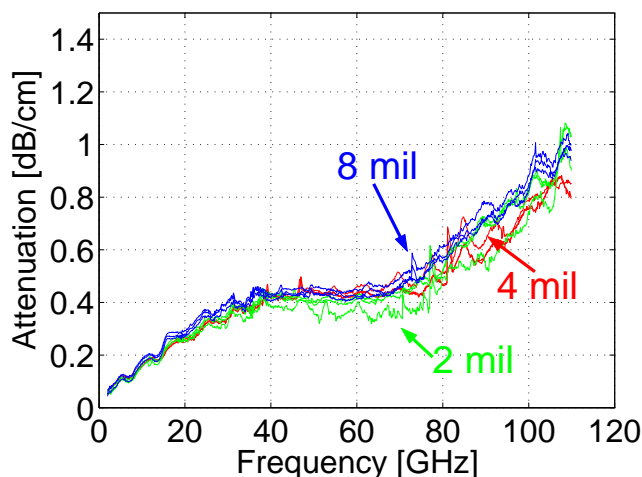


Figure 22. CPW total measured loss on a low loss foam spacer.

3.1.5.3 Microstrip Transmission Lines

Microstrips were designed with masks of $W = 114 \mu\text{m}$ for a 2 mil substrate and $W = 244 \mu\text{m}$ for a 4 mil substrate in order to obtain 50Ω lines. These mask dimensions were also used later to pattern on 3 and 5 mil substrates. The 2 and 4 mil substrates were patterned on the $18 \mu\text{m}$ standard copper, while those on 3 and 5 mil substrates were patterned on the

5 μm rolled copper foil. Due to the etching undercut and dielectric constant change to 3.16 (the transmission lines were originally designed for the manufacturer's dielectric constant value of 2.9 rather than the 3.16 found in this research), the characteristic impedance of the microstrips initially designed for 50 Ω varied by up to 6 Ω . The plots have been suppressed below 30 GHz since the CB-CPW-to-microstrip transition is not optimized below this frequency and the loss plot there is somewhat erratic. The fabricated lines had varying impedance values from 52 Ω to 88 Ω . The lines on 2 and 4 mil substrates were measured on several physically different sets of TRL lines. The spread in the attenuation levels is up to 0.15 dB/cm for a single design on a given substrate thickness (for 2 and 4 mil designs). This can be attributed to etching differences and imperfections in the fabrication of the TRL sets and also to measurement errors.

The results in Figure 23 show that loss decreases with increasing substrate thickness and that microstrip peak loss values are between 1.39-2.55 dB/cm at 110 GHz.

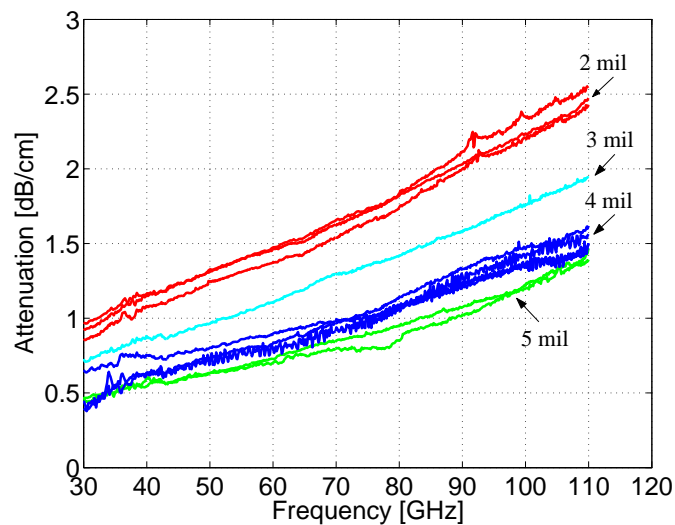


Figure 23. Microstrip line losses on 2-5 mil LCP substrate thicknesses.

The microstrip transmission lines configurations measured and their peak loss per unit length results are given in Table 8.

Table 8. MICROSTRIP TRANSMISSION LINES: LINE GEOMETRIES AND PEAK LOSSES.

h: substrate height, W: signal width				
h [mil]	W [μm]	Z_0 [Ω]	Sets Meas.	Attn. at 110 GHz [dB/cm]
2	88	56	3	2.55
3	104	68	1	1.94
4	218	52	4	1.62
5	104	88	1	1.47
5	234	59	1	1.39

The results of the transmission line loss per unit length measurements can be used as a design guide for expected losses for standard metallized traces on LCP substrates. The transmission lines of various impedances and types on different LCP substrate thicknesses show maximum attenuation of 0.88-2.55 dB/cm at 110 GHz. LCP's steady dielectric constant, relatively low loss tangent, and low transmission line losses for frequencies up to 110 GHz show for the first time that it has attractive electrical qualities for applications throughout the mm-wave frequency spectrum.

3.2 High Temperature mm-wave Dielectric Characterization

In this research LCP has been shown to have promising electrical properties for applications above 10 GHz [20], but temperature testing on it has previously only been done up to 8 GHz [47]. Since many of the desired LCP applications are at mm-wave frequencies, the material's thermal dielectric stability characteristics are important to identify across the mm-wave range.

LCP's thermal dielectric constant stability is investigated for the first time up to 105 GHz with the temperature varying between room temperature (25 °C) and 125 °C. A variable denoted τ_{ϵ} , the thermal coefficient of dielectric constant, is commonly given on material data sheets to specify dielectric temperature stability. To determine LCP's thermal characteristics at mm-wave frequencies, its τ_{ϵ} is investigated at 10 frequency points between roughly 11 and 105 GHz. In addition, the temperature dependent microstrip transmission line losses in dB/cm are measured from 10–110 GHz. The goal is to determine how significantly elevated temperatures affect LCP's dielectric constant and loss for frequencies greater than 10 GHz.

3.2.1 Method of Identifying Dielectric Stability

3.2.1.1 Temperature Coefficient of Dielectric Constant

The temperature coefficient of dielectric constant describes how much a material's dielectric constant changes with a given temperature change. This variable is usually given as

a constant over some temperature range, although it often changes slightly depending on the specific temperature. Typical absolute values for τ_{ϵ_r} based on a random sampling of material data sheets are from 11–280 [ppm/°C]. Values of τ_{ϵ_r} can be positive or negative, indicating an increasing or decreasing dielectric constant, respectively, with an increasing temperature. To extract τ_{ϵ_r} , the measured dielectric constant at some reference temperature, T_{ref} (usually 25 °C), is compared with that obtained at some lower, $T_{initial}$, and higher, T_{final} , temperature. Equation (5) is then used to find τ_{ϵ_r} .

$$\tau_{\epsilon_r} = \frac{\frac{\epsilon_r(T_{final})}{\epsilon_r(T_{ref})} - \frac{\epsilon_r(T_{initial})}{\epsilon_r(T_{ref})}}{T_{final} - T_{initial}} * 10^6 \left[\frac{\text{ppm}}{^\circ\text{C}} \right] \quad (5)$$

The τ_{ϵ_r} value has units of parts per million per degree Celsius [ppm/°C]. As an example, a material with $\epsilon_r = 3$, $\tau_{\epsilon_r} = -50$, and a temperature increase of 100 °C would be expected to change to $\epsilon_r \text{ at temp} = 3 + 3*(-50e-6)*100 = 2.985$.

3.2.1.2 Measurement Structures

Traditional mm-wave high-temperature dielectric characterization methods such as using split-cylinder, split-post, or Fabry-Perot resonators [48] inside of an environmental chamber can become prohibitive past 50 GHz. This and other resonant cavities have excellent measurement fidelity but they become problematic when attempting to integrate 1.85 mm or 1 mm coaxial connectors feeding into an environmental chamber. These connectors are expensive, fragile, usually short in length, and difficult to connect with precision. In addition, the design of coupling loops at the ends of very small diameter coaxial conductors is not a trivial matter, especially for mm-wave measurements. These loops are used to transfer the signal from coaxial to resonant cavity modes. Finally, 1 mm cables capable of 110 GHz measurements are almost exclusively used for measurements with GSG on-wafer probes.

Another measurement complexity arises from 50 GHz and higher signal generators. Bulky mm-wave mixing modules typically up-convert the signal very close to the measurement area. This makes for a cramped space for a temperature controlled measurement.

The numerous limitations of cavity resonators restricted the mm-wave temperature

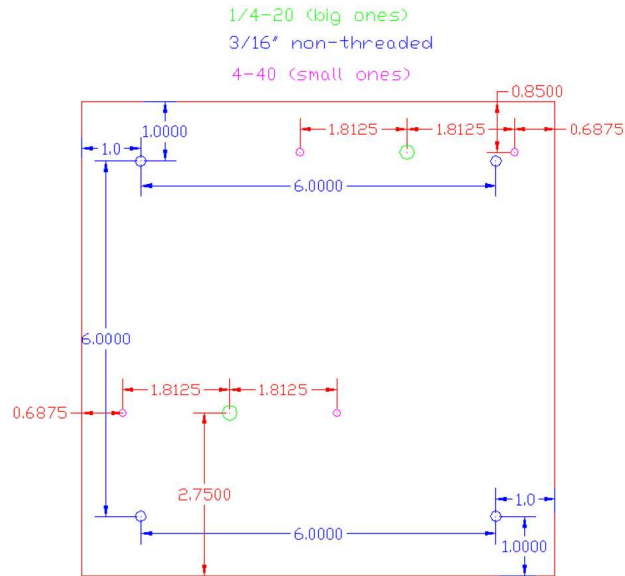


Figure 24. Drafting drawing for the custom aluminum spacer plates to elevate the mm-wave mixing modules.

measurements to printed resonant circuits with GSG feeding structures. The solution was to mount a Temptronic digitally controlled hot chuck (with 0.1 °C accuracy) onto the Agilent 8510XF chuck and to custom build 2” thick aluminum spacers for elevating the mm-wave mixing modules and the attached GSG probes to the same level as the hot chuck.

Mounting hole patterns for the custom aluminum spacer plates were derived experimentally from measuring the hole patterns on the underside of the mm-wave mixing modules with a digital micrometer. The drafting drawing for the plates is shown in Figure 24.

The final installed measurement setup including the spacer plates is shown in Figure 25.

3.2.2 Thermal Coefficient of Dielectric Constant Measurement

3.2.2.1 Measurement Procedure

Ring resonator configuration D from the mm-wave LCP characterization was used for the temperature measurements. The same measurement method was performed, but due to the resolution required for detecting extremely small changes in resonant frequency, a two stage measurement was performed. First, the ring resonators were measured to identify the locations of the resonant peaks. Then, once the resonant frequencies were established,

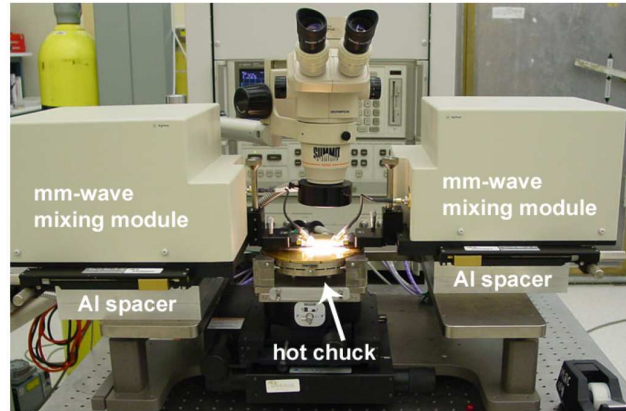


Figure 25. Heated temperature measurement setup on the 8510XF network analyzer. The digitally controlled Temptronic hot chuck and custom aluminum spacer plates are shown.

a second TRL calibration was done with much finer frequency resolution around each peak. The peaks were calibrated with frequency resolutions varying between 1.25 MHz and 3.75 MHz. The hot chuck was initially set to 25 °C. Calibrated S-parameters were then taken at 25, 50, 75, 100, and 125 °C. Once the hot chuck reached each desired temperature, 10 minutes were given for the probes and attached coaxial cable to heat evenly and for the temperature to settle.

An averaging factor of 256 was used for all measurements to reduce measurement noise. However, noise was still present in the measured data. Postprocessing using MATLAB was used to perform least-squares fits with each resonant peak to an analytical gaussian distribution. The residuals were then checked to verify an acceptable fit. Using the fitted gaussian equation, the maximum amplitude point for resonant peak was then identified to the nearest 1 KHz. This value was used as the resonant frequency for each peak. One exception was made near the 21 GHz resonance where the resonant peaks were strongly distorted and did not fit the expected gaussian distribution. This resonance frequency was thus left out of the analysis.

3.2.2.2 Measurement Accuracy

The most important consideration in taking a measurement with varying temperature is accounting for the expansion of the materials under test. The xy -CTE of LCP and the CTE of copper are matched at 17 [ppm/°C]. The z -CTE of LCP is higher at 150 [ppm/°C]. The measured resonant frequencies are thus a combination of both dielectric/metal dimension changes and changes in the dielectric constant. To separate these contributions, the equations from [20] for converting the measured resonant frequencies to ϵ_{eff} and ϵ_r were carried out with the corrected expanded dimensions for the mean ring radius r_m , the substrate height h , and the strip width W at each temperature. These dimensional uncertainties as well as the uncertainty in the LCP xy -CTE (± 3) [47] were taken into account as shown by the error bars in Figure 26.

3.2.3 Dielectric Constant Thermal Stability Results

3.2.3.1 Temperature Coefficient of Dielectric Constant

Two changes occur when the resonant structures under test are heated. A frequency shift of the resonant peak corresponds to a combination of the change in structure size and the change in the dielectric constant. Second, a decreasing Q -factor of the peaks with increasing temperature indicates an increase in dielectric loss.

Frequency shifts at each of the four ΔT values (25, 50, 75, and 100 °C) were recorded for each resonance. Calculating the dielectric constant (while accounting for the dimension changes at each temperature) provided four τ_{ϵ_r} values for each set of resonant peaks. The τ_{ϵ_r} value is known to vary slightly with temperature so the mean value was taken and this is the value given at each resonant frequency shown in Figure 26.

LCP's temperature stability near 11 GHz is excellent. However, it slowly degrades with increasing frequency and it seems to converge to a nearly constant τ_{ϵ_r} value between 53 and 105 GHz. Overall, LCP's temperature stability is as good or better than the 10 GHz PTFE/glass and alumina temperature stability values [5]. This is comparing LCP's stability over a nearly 100 GHz range while the others are for a τ_{ϵ_r} only at 10 GHz. Thus, the values

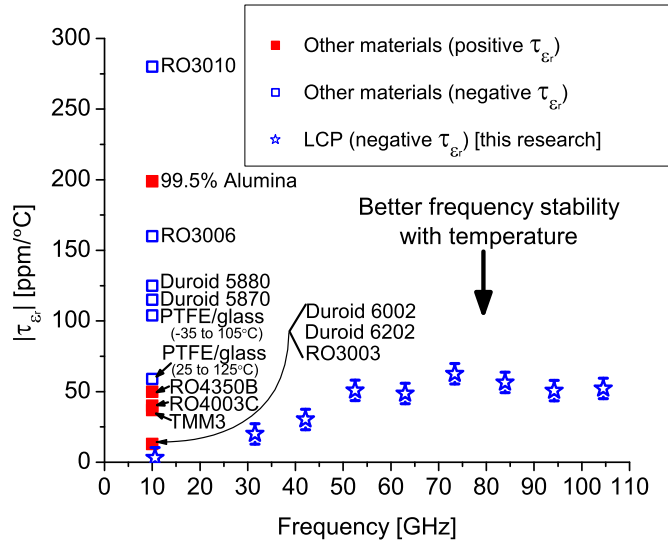


Figure 26. Absolute value of the thermal coefficient of dielectric constant, $\tau_{\epsilon'}$, vs. frequency of several standard materials and of the broadband $\tau_{\epsilon'}$ for LCP. The closer $|\tau_{\epsilon'}|$ is to zero, the more stable the dielectric constant is with respect to temperature.

measured for LCP show that it has attractive temperature stability properties for mm-wave applications.

Figure 27 shows the data in a different representation as normalized dielectric constant vs. temperature. This shows that the dielectric constant of LCP drops more sharply with increasing temperature at high frequencies. Finally, Figure 28 shows the actual values of LCP's dielectric constant vs. frequency and temperature.

3.2.3.2 Microstrip Transmission Line Losses vs. Temperature

At mm-wave frequencies, power becomes scarce and low insertion loss for transmission lines is important. Therefore, temperature dependent loss variations need to be taken into account. Microstrip losses in dB/cm were extracted from the TRL calibration previously mentioned using Multical software [38]. Losses are shown in Figure 29 for 3 and 5 mil LCP substrate microstrip lines.

Microstrips on both substrate thicknesses experience increases in loss of approximately 20% for $\Delta T = 50^\circ\text{C}$ and 50% or more for $\Delta T = 100^\circ\text{C}$ at 110 GHz. The specific percentage values are shown in Figure 29. These loss increases should be accounted for in LCP circuits

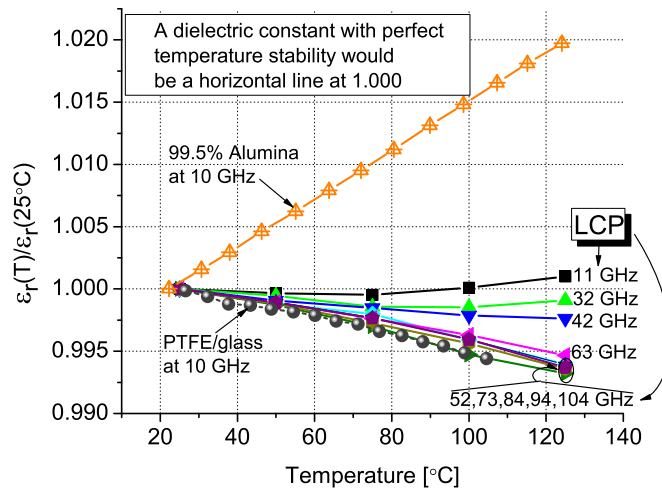


Figure 27. The ratio of LCP's heated dielectric constant and the dielectric constant at 25 °C vs. temperature. The values for LCP are for measurements from 11–105 GHz from this research. As a comparison, 99.5% alumina and PTFE/glass have been included. Notice that the values for 99.5% alumina and for PTFE/glass are for measurements at 10 GHz.

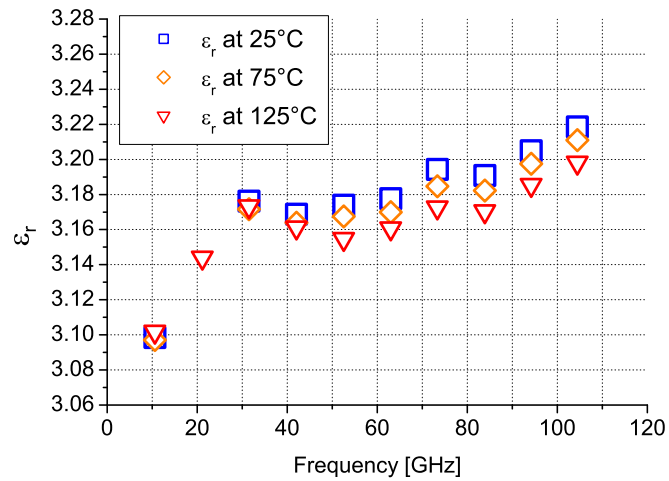


Figure 28. LCP's dielectric constant vs. frequency and temperature. The dielectric constant increases with increasing frequency and decreases with increasing temperature. Note that the peak at 21 GHz did not have a well shaped gaussian distribution and thus the resonant frequency could not be accurately calculated. However, the 21 GHz measurement at 125 °C was the best fit at that frequency and so only it is included for an estimate of the dielectric constant.

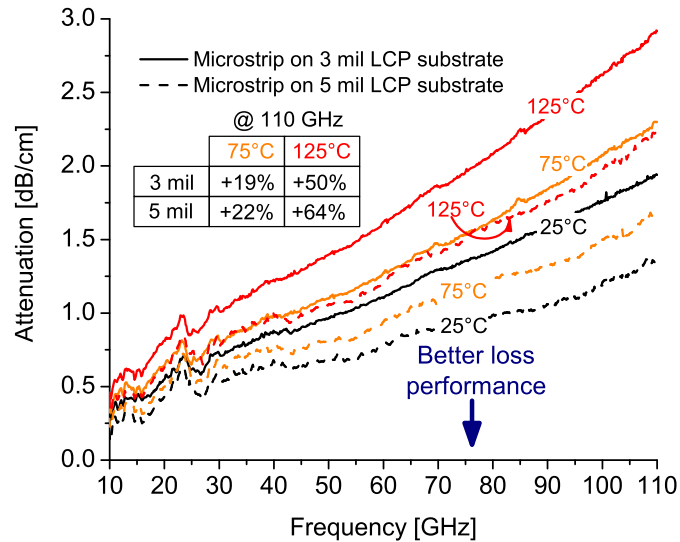


Figure 29. Attenuation of 3 and 5 mil LCP substrate microstrip transmission lines as a function of temperature. Line width, W , was $104 \mu\text{m}$ for both lines which gave $Z_0 = 68 \Omega$ and 88Ω for the 3 and 5 mil thicknesses, respectively.

used at high temperatures.

3.2.4 High Temperature Dielectric Characterization Conclusion

LCP has shown to be an excellent material for high temperature dielectric stability up to mm-wave frequencies for the first time. The average of the absolute values of τ_{ϵ_r} from 11–105 GHz is approximately -42 [ppm/°C]. This is comparatively better than a majority of other standard microwave substrate materials in this parameter. The microstrip transmission line losses on LCP increased steadily with increasing temperature. Loss increases of approximately 20% and 50% or more were observed for temperature increases to 75 °C and 125 °C, respectively. These loss increases should be considered for LCP transmission lines that experience significantly elevated temperatures.

CHAPTER 4

MULTILAYER LCP PROCESS DEVELOPMENT

Much of the promise of LCP is due to the potential to use it for multilayer RF circuits and systems. Multilayer circuits are possible as a result of two types of LCP material with different melting temperatures, but identical electrical characteristics. High melting temperature LCP (315 °C) can be used as core layers, while low melting temperature LCP (285 °C) is used as a bond ply. Thus, vertically integrated designs may be realized similar to those in LTCC. To the author's knowledge, no other material technologies besides LTCC and LCP are able to obtain a homogeneous dielectric lamination for creating hermetic or near-hermetic packages, which further elevates LCP's potential for highly integrated and packaged RF systems.

One important difference between LTCC and LCP lamination is that LCP's lamination temperature (at 285 °C) is potentially low enough to allow bare die semiconductor chips to be embedded during the bond process (this investigation is documented in chapter 6). LTCC's lamination temperature of ~850 °C is above the 400–500 °C threshold at which metallization in chips becomes damaged. The ability to bond LCP with active devices enclosed inside a homogeneous multilayer construction is thus a unique capability for a near-hermetic microwave substrate and packaging material.

An additional benefit in multilayer LCP over LTCC, due to its relatively low dielectric constant, is the increased radiation efficiency of antennas built on top of multilayer modules. In addition, LCP is advantageous for applications requiring larger area, high gain antennas, or in conformal applications.

The LTCC industry has proven the benefits of multilayer designs, including compactness, decreased cost, decreasing surface mount components in favor of embedded passives, and excellent stability/reliability as a result of the outstanding packaging characteristics of a multilayer laminated module. To obtain similar benefits in LCP, several investigations

were performed in this research to enable the construction of multilayer LCP circuits with integrated passive *and* active components. The goal of these process advances is to create low-cost mm-wave packaged antenna arrays and/or compact RF systems where embedded devices like RF switches, MMICs, filters, phase shifters, matching networks, etc., can be packaged in the same multilayer substrate.

Three processes had to be developed to create multilayer laminated LCP modules:

1. A reliable bonding recipe/procedure.
2. Precision hole and cavity drilling.
3. A multilayer alignment procedure.

4.1 Bonding Process

The bonding/lamination process of LCP is something that required the iterative testing of several different hot presses and many recipes of varying time, pressure, temperature, and vacuum settings. The process took eight months to develop and the first two hot presses used were found to be insufficient for controlling the bond process.

The primary reasons for difficulty with the bonding process are related to the tight temperature uniformity and accuracy required for proper LCP lamination. The tight temperature tolerance in the LCP bonding process is due to LCP's steep change in modulus of elasticity as seen in Figure 30. This figure shows that LCP has almost full mechanical stability up to its melting temperature, at which point only small increases in temperature drastically increase its flow characteristics. The trick to a successful LCP bond is to reach a temperature that is high enough to fuse LCP layers together by slightly melting type 2 low-melt bond ply material as "glue" layers to hold that stackup together, but without causing significant mechanical deformation. Due to the extreme modulus change over such a small temperature range, achieving the required temperature accuracy and tolerance across a lamination surface for an LCP bond proved to be beyond the capabilities of most standard

equipment.

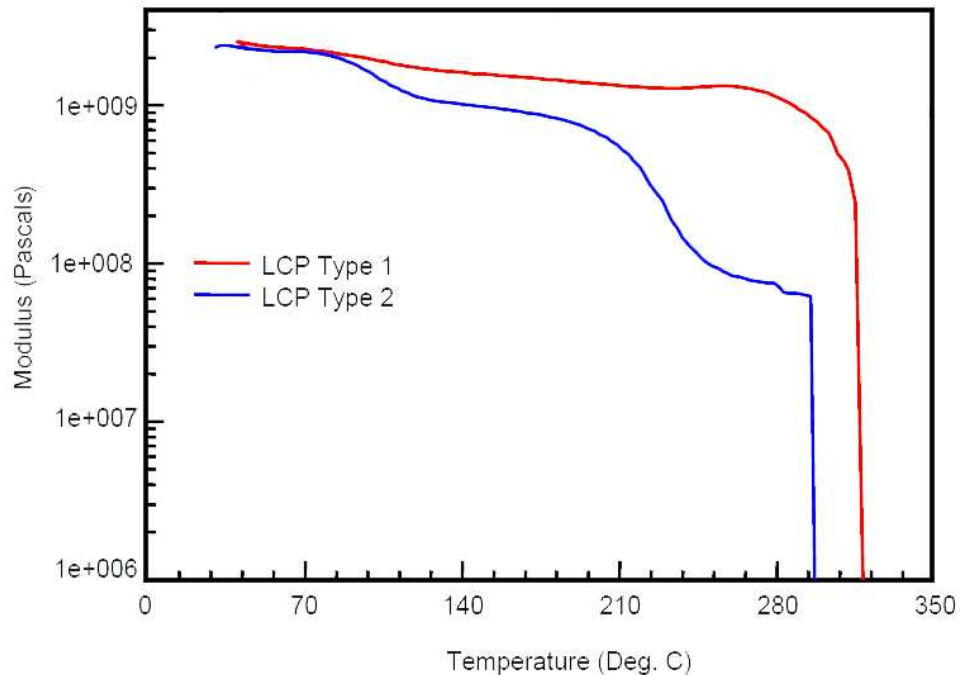


Figure 30. LCP modulus of elasticity vs. temperature. The sharp drop near 285 °C for type 2 LCP corresponds to an abrupt material phase change where it rapidly changes from a solid to a liquid with increasing temperature.

The desired lamination conditions required an extremely uniform 285 °C temperature distribution across press plates with a maximum deviation of only ± 2 °C. Unfortunately, this uniformity and accuracy is not possible with electrically heated presses. A heated thermal fluid press is required to achieve these lamination conditions. In a thermal fluid press, the platen temperatures are tightly regulated by heated fluid, which is distributed evenly inside of the press plates. Unfortunately, the knowledge of the correct lamination press needed for LCP lamination was not known until the end of the investigation.

The first press investigated was a 6" x 6" open air press with a hydraulic hand activated tool pressure and electrically heated platens. The tool pressure was controlled manually by adjusting a lever and screw release according to a digital pressure gauge readout. The press could not be controlled tightly enough in temperature and often over-melted the LCP layers forcing them to flow and bubble. This press was quickly discarded due to its poor

performance.

Next, a Wabash vacuum press with 24” electrically heated and water cooled platens was investigated for LCP bonding. Although this press could be programmed to run a specific temperature and pressure cycle, it was not capable of creating the platen temperature uniformity to result in reasonable LCP bonds. At lower temperatures, the temperature uniformity was tested by hand and extreme temperature differences across the platen surfaces were verified.

Finally, in June 2003, a successful LCP lamination process was developed in the Georgia Tech Microelectronics Research Center (MiRC) clean room with the Karl Suss SB-6 silicon wafer bonder. The wafer bonder was determined to be the most capable machine available at Georgia Tech for providing an LCP bonding capability. It has computer controlled top and bottom platen temperatures, vacuum pressure, and tool pressure. Figure 31 shows the bonding machine.



Figure 31. The Karl Suss silicon wafer bonder enables a precise LCP lamination process for a total thickness of up to several millimeters.

Some practical considerations for LCP bonding in the wafer bonder include:

- Maximum lateral size = ~4"
- Maximum vertical thickness (including the LCP stackup, alignment plates, non-stick foils, etc.) = 6 mm

The wafer bonder worked for a majority of the requirements for research grade LCP bonding, however, since the wafer bonder is an electrically heated press that is optimized for accuracy closer to 400–500 °C for bonding wafers, the temperature accuracy near LCP's ~285 °C desired lamination temperature was not ideal. To overcome this mismatch, many experimental bond temperatures were run until the desired bonds occurred. The method for this bond recipe optimization involved starting with a temperature far below 285 °C, and the temperature raised in successive bonds by 10–20°C until the layers were laminated together. If the temperature was too high, the layers would visually flow too much and if it was too low, the layers would be easily pulled apart. A fine tuning in between these extremes was performed until the LCP bonded as desired. Each time, the bonded samples were examined under a microscope and a razor blade used to determine whether the bonded layers could be split apart.

A graphic representation of the desirable LCP bond parameters is shown in Figure 32. These recipe parameters are those deemed reliable for commercial bonding. This recommended bonding profile, from Rogers Corporation, was not available until about one year after bonds were being performed with the Karl Suss wafer bonder at Georgia Tech. However, helpful hints were obtained by speaking with company representatives during the development stage. Once this recipe was verified as optimal for LCP bonding, the recipes used at Georgia Tech were migrated to match the commercial parameters. The recipe was found to work very well.

As briefly mentioned already, in industry, due to reliability and repeatability considerations, heated thermal fluid presses are a requirement for LCP lamination. These hot fluid circulating presses have quoted temperature tolerance and uniformity of ± 2 °C, which is a

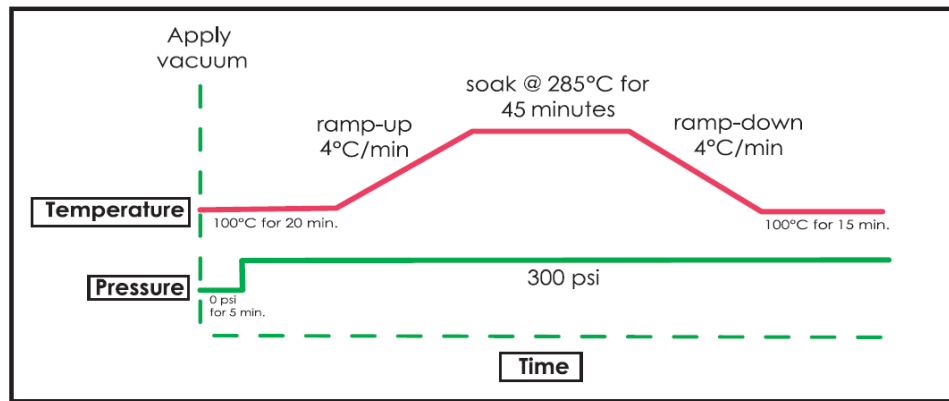


Figure 32. Recommended LCP bonding profile.

significant improvement over even the best electric presses. The best electric presses have approximately $\pm 5^\circ\text{C}$ at LCP's lamination temperature. The wafer bonder has an accuracy estimated at $\pm 5\text{--}10^\circ\text{C}$ which is easily a large enough temperature difference from the required lamination temperature to introduce uncertainties from one run to the next in terms of producing a successful or unsuccessful lamination. Despite this equipment limitation, the wafer bonder was used successfully for robust LCP bonding. To account for potential bonding inaccuracies, several samples were prepared for bonding. The yield, higher than 75% for established process parameters, was acceptable for research purposes.

To perform a bond, the layers are stacked over a fixture with alignment pins and low melting temperature LCP bond layers are placed between each set of core layers. Teflon sheets with 5 mil thickness are placed on the outermost LCP layers to prevent the LCP from sticking to the press plates. The top plate is positioned on the top of the bond stackup. Aluminum foil is then wrapped around the exterior of the fixture to protect the bonder in case the LCP melts and flows outside the bonding contact area. The press plates are placed in the bonder and run through the automated optimized LCP bond process according to the process shown in Figure 32. Note that all of the layers (including the Teflon non-stick layers) on the fixture have laser cut alignment holes to ensure precise alignment. The laser

processing and alignment setups are described below.

For future research, two leading companies with thermal fluid presses have been contacted and quotes obtained for a laboratory sized thermal fluid press. Each has a Windows computer with software for automated process control, a vacuum chamber, and sufficient tool pressure to provide the desired 300 psi for LCP lamination across the entire platen area. These lab sized solutions are from OEM Press Systems and Burkle.

This successful LCP lamination process was probably the most important enabling step to continue research in multilayer LCP RF constructions.

4.2 Laser Processing

To create precise alignment holes and package cavities, a detailed laser processing investigation was performed. As opposed to mechanical drilling, laser processing of LCP does not require de-burring and the laser precision is far superior. Mechanical drilling was passed over because of a multilayer antenna design that required alignment to be within 15–20 μm in the worst case. Two of three available laser systems have stage positioning accuracy of 1 μm or better and precise alignment procedures using video microscopes. The author chose to investigate using the lasers since they seemed better suited for the job than a mechanical drill. As a result of this investigation, several unique capabilities were discovered which enabled the formation of thin-film, multilayer, laser micromachined LCP packaging structures (described in chapter 6).

The three systems investigated were CO₂, infrared, and excimer lasers. Below is a summary of the findings of the advantages, disadvantages, and key enabling features of each laser related to the multilayer LCP process.

CO₂ Laser (10 μm wavelength, 150 μm spot size):

CO₂ Laser Advantages:

- The CO₂ laser is the fastest for cutting alignment holes, outer sample boundaries, and arbitrary shapes such as square holes through bare LCP. As an example, a square hole

becomes a cavity when solid LCP layers are laminated on top and bottom. Drilling four 1/16" alignment holes into LCP thicknesses from 1–4 mils takes ~5 seconds.

- Unlike the infrared laser and excimer laser, which each suffered occasional reliability problems, the CO₂ laser seemed to be extremely reliable. Power supply instabilities, maintenance of critical gas tube mixtures, and burn marks on laser optics were problems with the infrared and excimer lasers. The CO₂ laser did not experience any of these problems.
- The laser is ready to fire immediately when it is turned on. No lengthy warmup/cooldown routine or checking/re-filling of gas is required.

As an example of the CO₂ laser cutting capabilities, some LCP superstrate layers cut out by the laser are shown in Figure 33.

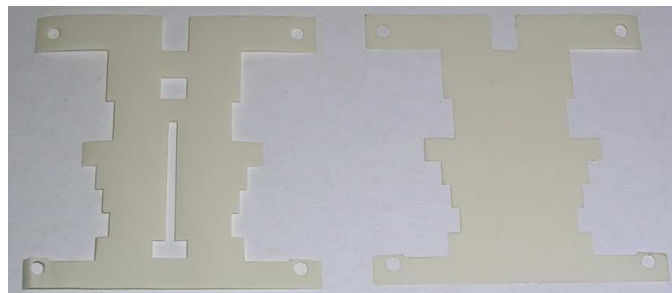


Figure 33. Bare LCP layers cut into the desired shapes with the CO₂ laser, including the sample perimeter, alignment holes, and cavities in the left sample.

CO₂ Laser Disadvantages:

- It leaves the worst burn residue of carbon ash along the cutting edges, that can smear and dirty the sample. A solution to remove the burn residue, which was worked well and was used regularly, was to remove it with an oxygen plasma clean.
- The precision is the lowest of the three laser systems, though it is still good enough to make cavities, alignment holes, and sample boundary cuts.
- The laser spot size is too large to make features below a few hundred microns.

- A precise alignment procedure does not exist for the engraving laser (no microscope and/or moving chuck) [however, a more expensive CO₂ laser could have alignment].

Infrared Laser (1047 nm wavelength, 75 μ m spot size):

Infrared Laser Advantages:

- It can cut through metal, which is ideal for cutting alignment holes through double copper-clad LCP before patterning.
- Alignment is done with a video microscope and the stage accuracy is better than 1 μ m.
- Feature accuracy and edge quality are generally excellent. Features frequently measured within 10 μ m of the design size, although the smallest features achievable are limited by the 75 μ m beam spot size.

A double copper-clad 4 mil piece of LCP with alignment holes cut by the infrared laser is shown in Figure 34.

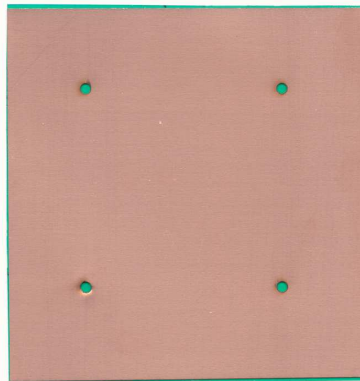


Figure 34. Four mil LCP with 18 μ m copper on each side with four alignment holes drilled by the infrared laser. The green color seen through the holes is polyester green tape used to protect the backside metallization during the etching process.

Infrared Laser Disadvantages:

- Warmup time of this laser system is 1 hour.

Excimer Laser (248 nm wavelength, spot size defined by mask [down to 5 μm]):

Figures 35 and 36 show the excimer laser setup and an alignment hole drilled by it, respectively.



Figure 35. 248nm KrF excimer laser. Minimum obtainable features are $\sim 5\mu\text{m}$.

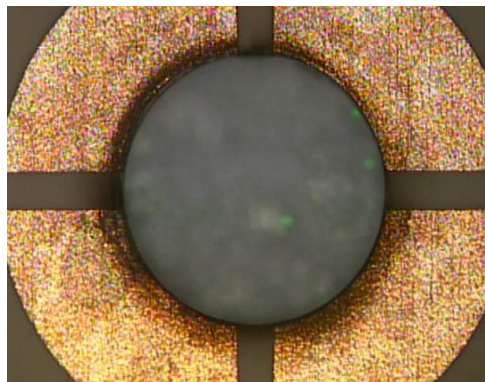


Figure 36. Precise alignment hole cut with the excimer laser.

Excimer Laser Advantages:

- It has the best feature resolution by far. Via holes down to 10–20 μm are possible the excimer laser.
- Arbitrary shapes or patterns can be cut because of the mask system it uses rather than a traditional laser spot. Circular apertures can also be used to create a circular laser spot.

- Cavities can be cut in single copper clad LCP, stopping on the backside metallization without going through it (using the backside metallization as an excimer laser stop layer). This method is used in chapter 6 to create precise cavities for mounting chips.
- Accurate depth-controlled material ablation is possible. The uniformity of depth-controlled cavities is excellent once the ablation rate is determined. However, the uniformity can suffer if the optics have burn marks.

Excimer Laser Disadvantages:

- It is very slow for cutting large features (features greater than a few mm). To cut large holes, a spot beam must be traced around the shape's perimeter. Holes cut in this manner through 4 mil LCP may take several hours.
- The rare gas mixture balance required for the excimer laser can be temperamental and is expensive to refill.

Conclusions drawn from using all three laser systems are as follows: The CO₂ laser is ideal for cutting out any desired shape from bare LCP layers fast and reliably. The excimer laser enables very precise depth-controlled packaging cavities to be etched into thin-film LCP substrates. The excimer is also desirable for small vias and for creating cavities which stop on the backside copper metallization. The infrared laser is most useful for cutting precise alignment holes through double copper-clad LCP or whenever cutting through double copper-clad material is required.

Some standard operating parameters for the laser systems that work well for cutting LCP are described below. To describe the details for every possible configuration would be unnecessarily tedious since most of the laser have numerous parameters that can be varied. The recipes below are provided as a baseline to give an idea of what works.

CO₂ laser: For bare 4 mil LCP, 20% power and 50% speed in vector mode will cut through in one pass. For 1 mil LCP, 10% power and 50% speed in vector mode works well.

Infrared laser: The infrared laser should have the lens set on zero attenuation to allow maximum power on the sample. A cutting velocity of 3–4 mm/sec with 3 passes will cut through double clad 4 mil LCP cleanly. Contrary to logic, if the cutting velocity is lowered on the infrared laser, it may not cut faster since the metal may not be ejected as efficiently away from the sample. Several passes with a faster cutting rate generally works better than a very slow cutting rate and one pass.

Excimer laser: Energy level = 250 mJ; Demagnification = 10; LCP thickness = 4 mil; The laser will cut through to the bottom in about 300 pulses, but if laser optics are dirty, certain spots may not be ablated cleanly, so a few hundred additional pulses may be necessary. The maximum pulse rate for the excimer laser is 90 Hz, but 50 or 60 Hz were generally used for processing. If the pulse rate is too fast, material cannot escape the firing path before the next pulse arrives, which can create a dirtier, less effective cut. If the pulse rate is too slow the cut will take longer. At 50 Hz, if a single hole is cut in one continuous firing sequence, the cut time for the hole is between 6 and 10 seconds. This hole cutting time is valid for sizes that are achievable with 10x demagnification, which are limited by the aperture uniform illumination area to an on sample circular hole diameter of about 0.75 mm.

Samples that have been laser cut all require an oxygen plasma clean to remove the carbon residue before further processing is carried out. The oxygen plasma cleaning recipe used for removing carbon residue from the cutting edges was developed by group member Nickolas Kingsley on the Plasma-Therm RIE in the Georgia Tech MiRC clean room. The recipe is titled NKI_POLY. The recipe uses a power of 350 W. A time of 3 minutes per side will clean the thin residue from a sample. An example of a CO₂ and excimer laser cut sample before and after plasma cleaning is shown in Figure 37. A bare sample cut through with the CO₂ laser requires both sides to be cleaned while a sample which has backside metallization and is cut with the excimer laser will only require a top side plasma clean.

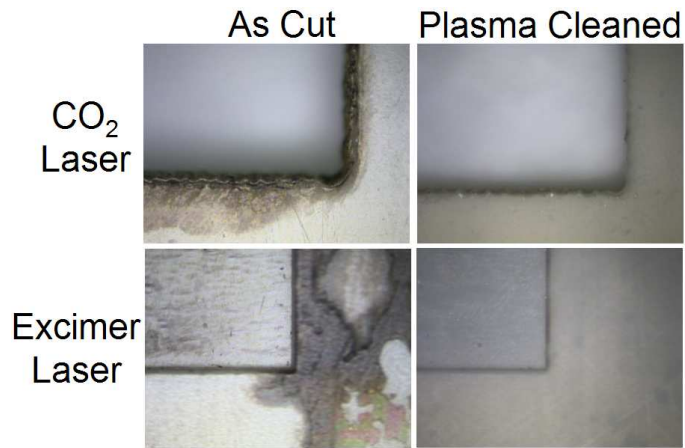


Figure 37. Laser cut samples before and after oxygen plasma cleaning.

4.3 Alignment

Bonding fixtures with alignment pins were the last development that enabled multilayer aligned LCP laminations. Special considerations were made to accommodate bonding in the silicon wafer bonder. First, the lateral size of the plates is limited to less than 4". Next, the total vertical dimension of the stacked plates plus the inserted samples cannot be more than 6 mm. This vertical dimension is a fundamental limitation of the bonder. Two sets of aluminum alignment plates were made, one large and one small. Table 9 describes the alignment plate geometries.

Table 9. ALIGNMENT PLATE GEOMETRIES

	Horizontal Dimensions	Plate Thickness	Alignment Pin Hole Pattern	Alignment Pin Diameter
Large Fixture	7 x 10 cm	0.1"	5 x 6 cm	1/16"
Small Fixture	35.4 x 35.4 mm	0.09"	30.4 x 30.4 mm	1/16"

The alignment pins were press fit into the bottom press plate. The top press plate slides on/off. The small alignment fixture is shown in Figure 38.

The alignment procedure includes pre-cutting holes through the LCP substrates before patterning. All three of the laser systems were used at various times during this research to make the alignment holes. The excimer laser was used when extreme precision was



Figure 38. Small aluminum alignment fixture.

required, the infrared laser was used when double copper-clad LCP required cutting, and for general alignment hole cutting for LCP superstrate packaging layers, the CO₂ laser was the system of choice.

Circular alignment marks slightly smaller than the holes through the substrate are made on the mask so that they can be aligned concentrically within the holes in the substrate during the photolithography process. This method enables front-to-back alignment so that aligned patterning can be performed on both sides of a substrate. The alignment pins in the press plates match the locations of the drilled holes in the patterned LCP substrates. All LCP samples and the Teflon non-stick pads are stacked on the alignment fixture and run through a bonding process to create a laminated multilayer LCP stackup.

CHAPTER 5

LCP PASSIVE DEVICE PACKAGING AND TESTING

5.1 Example: NASA 14/35 GHz dual-polarization 2x2 element antenna arrays

The immediate motivation for initiating a multilayer LCP process was to design and realize 14 and 35 GHz dual-polarization antenna arrays on LCP. This project is part of a research contract with NASA for space-based antenna arrays that image precipitation and snow. Since the start of this project in 2003 the antenna designs have targeted the use of multilayer LCP constructions. The antenna design process has been carried out by three antenna designers: Vasileios Iliopoulos, Gerald DeJean, and Ramanan Bairavasubramanian. Throughout this antenna project, the author has worked closely with the antenna designers in formulating possible configurations and in determining the ultimate structure of the final antenna designs. The final design utilizes all of the capabilities of the multilayer process. It includes laser cutting, bonding, patterning aligned layers on both sides of the same substrate, and alignment with the custom-made press plates. Figure 39 shows the very first successful bond of antenna arrays on multiple layers of LCP from June 2003. This design did not require any alignment or special preparation before the bond procedure.

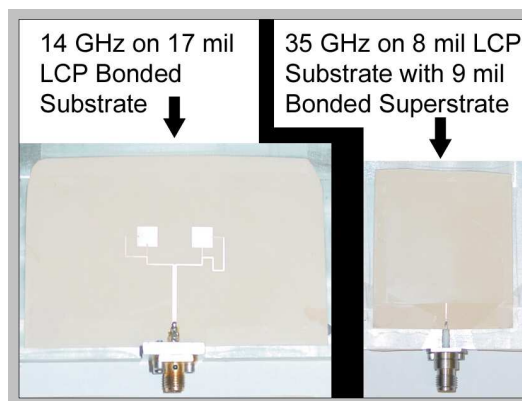


Figure 39. June 2003 LCP antennas. These antennas were the first devices bonded after the development of a successful LCP bond recipe.

In contrast to the first antenna design, the final design is shown in Figure 40. This design has feed lines and aperture slots patterned on opposite sides of the 4 mil bottom substrate in relation to the pre-cut laser holes. The middle 4 mil substrate contains 35 GHz antenna patches and the top 8 mil layer has 14 GHz patches printed on it. Two 1 mil LCP bond layers are used between the core layers to bond the stack together.

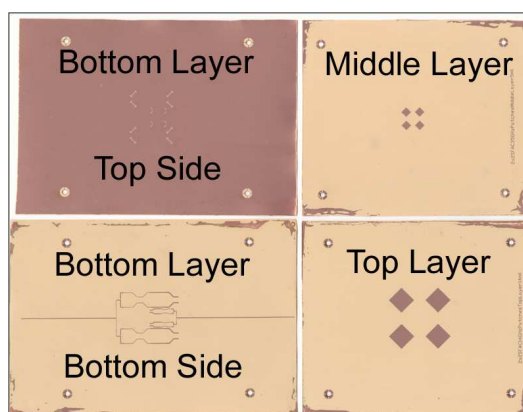


Figure 40. December 2004 aperture coupled 2x2 antennas with all of the patterned layers shown.

A diagram of the layer stackup, which offers a better representation of the configuration, is displayed in Figure 41. The diagram was done by the antenna designer, Ramanan Bairavasubramanian.

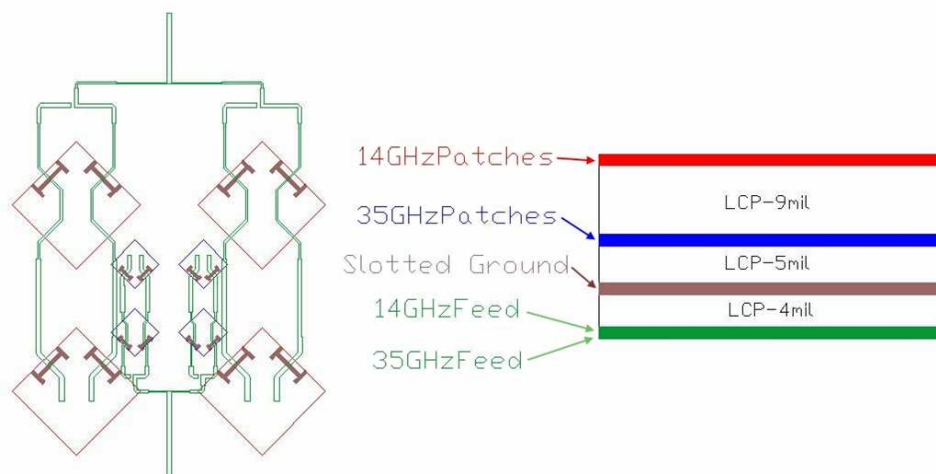


Figure 41. Diagram of the layer stackup for the final design for the aperture coupled 2x2 antennas.

Figure 42 shows the antenna layers stacked loosely over the large alignment fixture. The top aluminum press plate that sandwiches the layers during the bond process is not shown. The multilayer LCP design capability demonstrated with this antenna example is an important stepping stone for demonstrating functional multilayer LCP RF components.

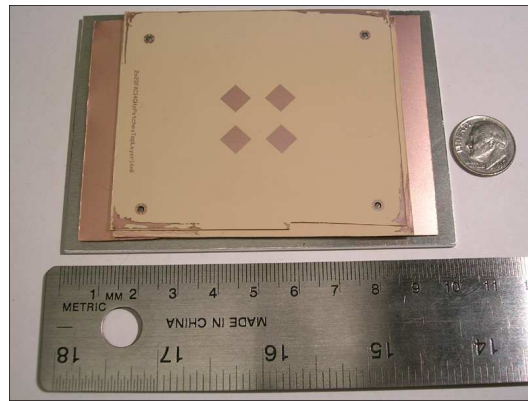


Figure 42. December 2004 aperture coupled 2x2 antennas resting on the alignment fixture.

S_{11} measurements for all generations of these antennas were performed at Georgia Tech, while most of the radiation patterns have been made at the NASA Glenn research facility in Ohio. An example of the S_{11} measurements is shown in Figure 43. The measurements for resonances designed for 14 and 35 GHz are shown. All four measurements are within 300 MHz of their respective design frequencies.

Similar measurements have been done for all four generations of the 14 and 35 GHz antenna arrays (only two are mentioned here). Results for some of these can be found in [49,50].

5.2 Flexibility Testing

One of the key capabilities of antennas on LCP is the assumed ability to be rolled and then deployed once in space. To verify these capabilities, tests were performed on the mechanical rollability and the effects of rolling on the antenna performance. An older 14 GHz 1x2 design was used as a test case since it has a much wider feed line than current designs and can be connected/disconnected with repeatable results with connectors that

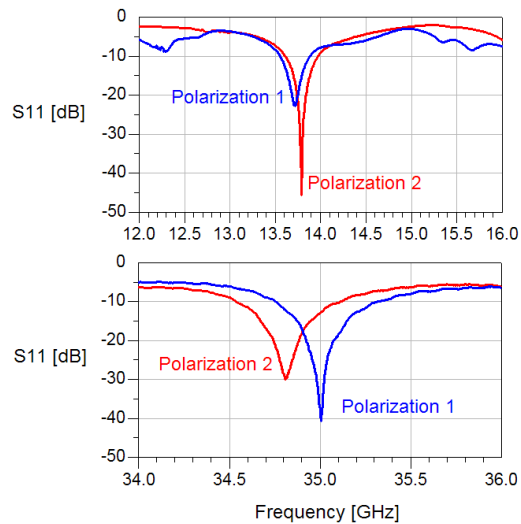


Figure 43. S_{11} measurements for the first generation of 14 and 35 GHz antenna arrays on LCP.

have large, robust signal pins. This antenna array is on a 17 mil substrate which is similar to the 18 mil substrate thickness for the final 2 x 2 antenna design. A picture of an antenna in the default flat state is shown in Figure 44.

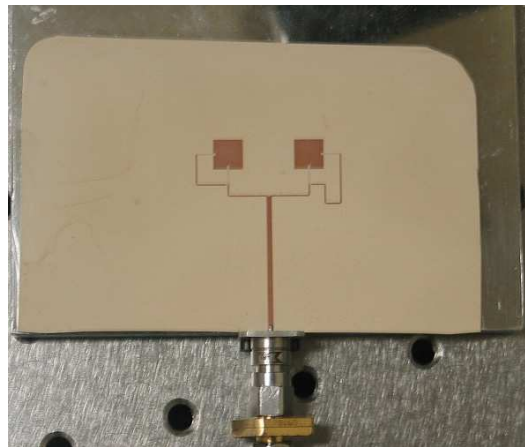


Figure 44. The 14 GHz 1x2 antenna array on a 17 mil bonded LCP substrate.

The procedure for performing this antenna testing included:

1. Ensuring measurement repeatability when connecting/disconnecting an antenna in the default flat state
2. Performing flexure testing on the antenna, rolling it into tubes with various diameters

3. Re-measuring and observing potential differences in measurement or visual structural changes

To ensure measurement repeatability the antenna was connected and disconnected five times by sliding the antenna feed between the coaxial signal pin and the metal ground plane. The signal pin was then forced into hard mechanical contact with the feed line and screwed into position (no solder was used)

Each time the antenna was connected, it was re-measured with a network analyzer and evaluated for any connection related shifts in resonant frequency. A short-open-load-through (SOLT) calibration with 201 data points between 12–16 GHz was used in the measurement. The resulting frequency step was 20 MHz which is a 0.14% frequency resolution at the resonant frequency of 13.80 GHz. This resolution was deemed sufficient to determine any significant frequency shifts. Figure 45 shows the measurement results from measurements taken during the five connect/disconnect cycles. The S_{11} plots are nearly identical for 5 cycles of connecting/disconnecting the antenna.

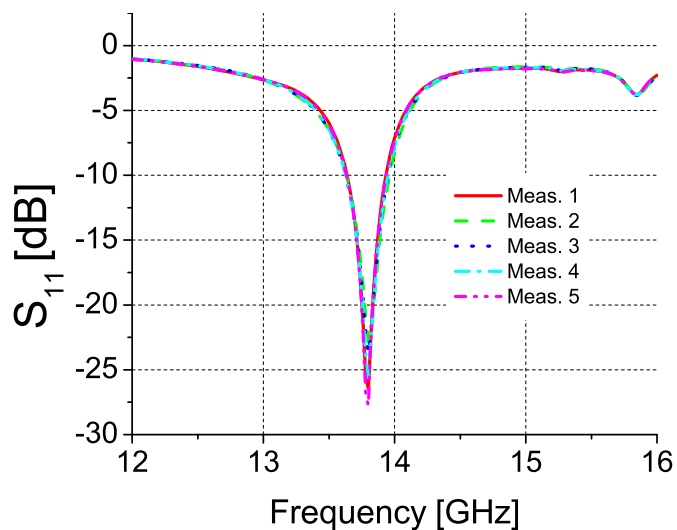


Figure 45. Measurement repeatability testing by connecting the antenna five times and re-measuring it. The dotted rectangle area is magnified and re-plotted in Figure 46.

Figure 46 shows a zoomed in representation of Figure 45, which demonstrates that all resonances occurred at exactly the same frequency point. The level of S_{11} at resonance varies

from -22.5 dB to -27.5 dB which is a negligible 0.4% difference in radiated power. Since the antenna measurements were the same each time it was connected and disconnected, testing was commenced on testing the affects of flexing on antenna performance.

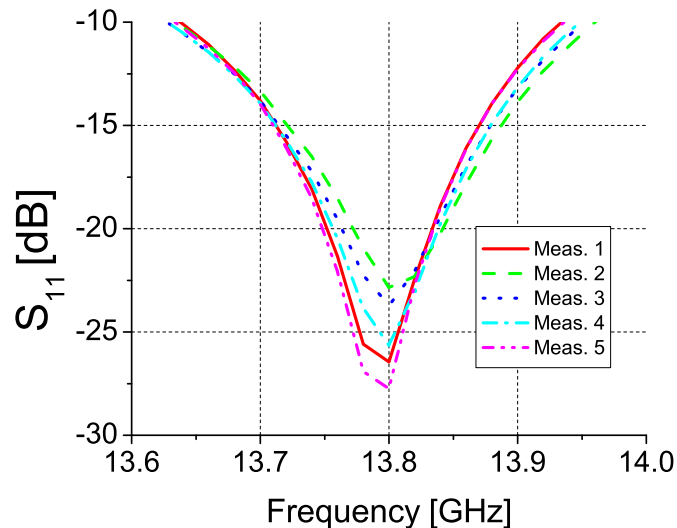


Figure 46. Zoomed in plot of Figure 45. The resonance minimum occurs at the exact same frequency point every time showing that the measurement is repeatable when the antenna is in its default (flat) state.

To test the potential antenna rolling capability, several plastic pipes of varying diameter from Home Depot were used as the conformal surfaces. The inner diameters of the pipes used were 6-5/8", 4-1/2", 3-1/2", and 2-5/8". Figure 47 shows a size comparison of the various pipe diameters next to the antenna and a penny.

Figure 48 shows the antenna array conformed inside of the 2-5/8" pipe.

An extreme case where the antenna was wrapped around a magic marker is shown in Figure 49.

Figure 50 shows the same roll diameter around the magic marker from the top view. In this state the antenna has a roll diameter similar to that of a penny.

For each of these antenna roll diameters the following procedure was carried out:

1. The antenna was conformed to the inner diameter of each pipe (to the outer diameter of the magic marker) and held for 1 minute.



Figure 47. Various pipe diameters in which to roll the 14 GHz antenna.

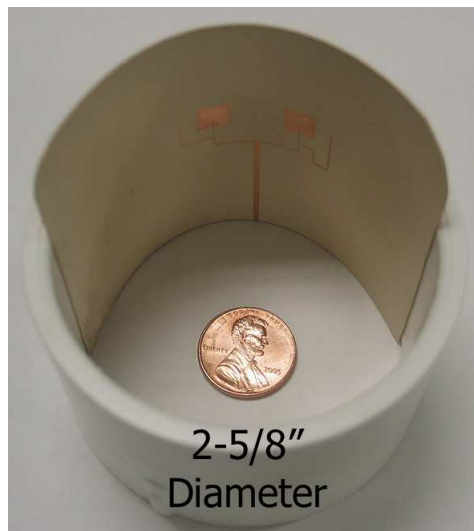


Figure 48. The antenna conformed inside the 2-5/8\" inner pipe diameter.

2. The antenna was removed, flattened, and re-measured.

For most of the roll diameters the antenna was easy to force flat to re-measure in the same flat position as the base case. However for the two tightest roll diameters of the 2-5/8\" pipe and the magic marker, a more significant residual curvature remained. This curvature was also able to be flattened with mechanical force, but before doing this, each antenna was measured in each of these curved states to see how the curvature affected the radiation frequency. Figure 51 and Figure 52 show the residual antenna curvature from these two

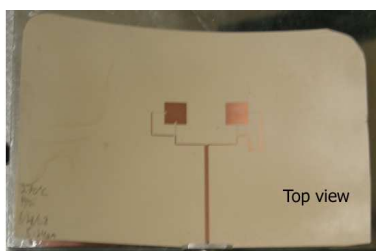


Figure 49. The antenna rolled around a magic marker and taped in place.



Figure 50. The antenna roll diameter from the magic marker shown in comparison to the diameter of a penny.

roll states.



Residual curvature from
2-5/8" roll diameter



Figure 51. Top and side views of the residual curvature of the antenna after taking it out of the 2-5/8" diameter pipe.

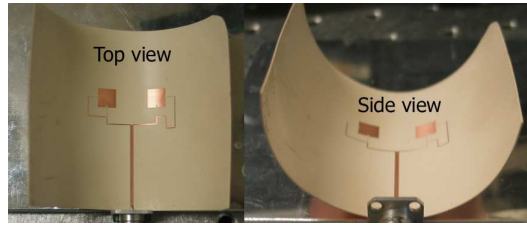


Figure 52. Top and side views of the residual curvature of the antenna after taking it off of the magic marker.

The measurement results from all of the aforementioned cases are shown in Figure 53 and Figure 54. These include:

1. Measuring the antenna flattened after flexing to different diameters.
2. Measuring the two cases of the antenna with the residual curvature.
3. Measuring the antenna after flexing it in opposite directions in the 2-5/8" diameter 10 times then flattening it.

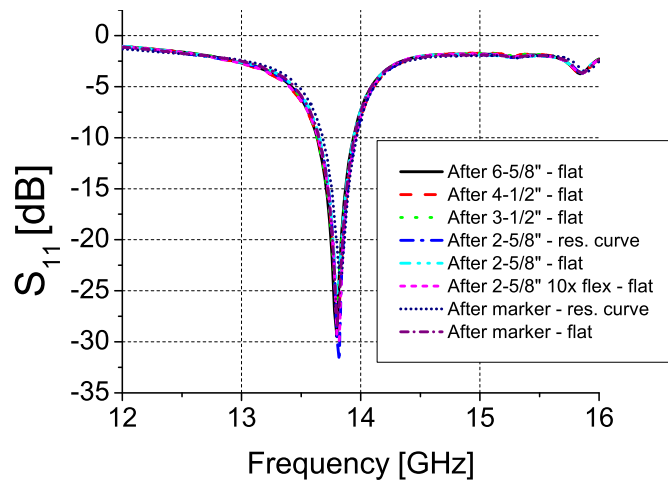


Figure 53. Measurement results of all of the cases of flexing the antenna. Two of the measurements include the antenna in a curved state while the rest are of the flattened antenna after conforming it to different roll diameters.

The measurement case that differed significantly was the one measured while still in the curved state with extreme residual curvature from the diameter of the magic marker. However, even with this curvature, the S_{11} shift was only 0.29%. After flattening the antenna, it again performed identically to the initial measurement.

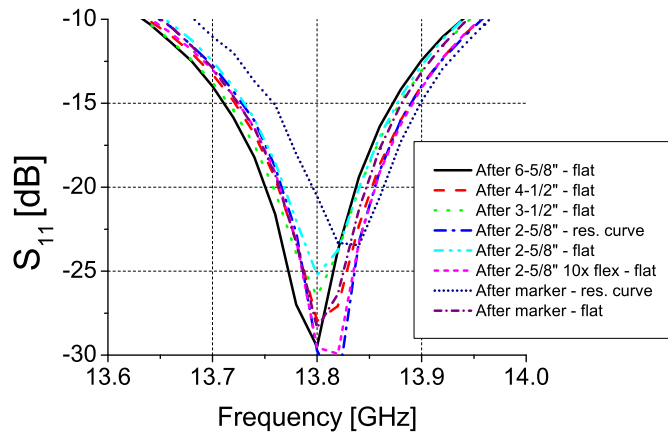


Figure 54. Zoomed in representation of Figure 45.

Several conclusions can be drawn from these antenna flex tests and measurements. First, the 17 mil LCP substrate thickness, which is a likely thickness for a multilayer antenna array, was rolled without difficulty into several tube diameters, including the extreme case of the magic marker. This demonstrates that even relatively thick, bonded LCP substrates have sufficient flexibility to be rolled and unrolled for antenna applications. Further, the LCP can be re-flattened with minimal effort so that the antenna element orientation and spacing are returned to their desired planar configuration. The mechanical robustness of the antennas was demonstrated, as no metal or substrate delamination was observed. Finally, the antenna flexure did not affect the antenna performance (as hoped/expected). These findings demonstrate that antenna arrays on LCP substrates may be rolled and re-deployed and/or conformed as desired without inducing mechanical or electrical differences in the antenna performance.

5.3 LCP Water Absorption

Microwave and millimeter-wave (mm-wave) RF circuits and systems require proper substrate and packaging materials to ensure reliable operation. In particular, the acceptable water absorption characteristics for packaging materials has become a topic of debate. Depending on the desired operating life of the application, appropriate materials are chosen to meet both the lifetime specification and cost. For example, cellular handsets with plastic

packages may be rated to survive for less than ten years, while critical satellite or military devices with hermetic ceramic or metal packages can be expected to last for several decades [51]. However, the packaging implementations of permeable plastic packages vs. the ceramic/metal hermetic packages can make a difference of several orders of magnitude in cost.

Recently, some have questioned the need for truly hermetic packages and even suggested that the “hermetic” requirement could be an outdated and unnecessary requirement from “what worked” for military projects as far back as the 1960’s [52]. Organic materials that have a “near-hermetic” classification could be sufficient to provide acceptable packaging characteristics for intermediate to long lifetimes, and at a fraction of the price, weight, and size of current hermetic packaging solutions [15].

Previous data from [53] shows changes in dielectric properties of materials with 0.25% and 0.05% water absorption. A conclusion is that 0.25% is not an acceptable water absorption level. Several sources [20, 22] have pointed out that liquid crystal polymer (LCP) is a near-hermetic organic material with excellent electrical properties and the ability to be engineered to match the α -CTE of both metals and semiconductors. Recently, [54] has been submitted from this research, which demonstrates a packaging topology that allows active/passive integration on a multilayer laminated near-hermetic LCP substrate. The details are discussed in chapter 6.

The contribution of this research is to investigate the quantitative effects of water absorption on passive element performance in the RF/mm-wave frequency range for low water absorption substrates. Quantitative testing is performed on observed water absorption and the corresponding frequency shifts of microstrip patch antennas on three different low water absorption substrates (0.1% or less). The findings of this research are important for validating non-hermetic, low water permeability substrates as desirable packaging materials for microwave and mm-wave RF systems.

5.3.1 Water Absorption Measurement

The first goal of this research is to experimentally find the relationship between water absorption and passive device performance. Although manufacturers provide water absorption percentages for their materials, this number is difficult to directly relate to expected changes in device performance. In addition, the author did not locate literature that tested passive devices on substrates with varying water retention/permeability characteristics.

The standard technique that microwave materials manufacturers provide for classifying water absorption characteristics is a weight percentage of water absorbed according to IPC-TM-650 2.6.2.1. A range of water absorption characteristics of organic materials is from 0.02% to 0.25% or more. It is well known that low water absorption percentages are better for stability and reliability. Focusing on low absorption materials, a sampling of three microwave substrates with water absorption of 0.1% or less were selected for testing. These materials are compared in table 10. The water absorption percentage listed is that provided by the manufacturer.

Table 10. LOW WATER ABSORPTION MATERIALS TESTED

Material	Water Absorption [%]	ϵ_r	$\tan \delta$	Thickness [mils]	Metal Thickness [μm]
6202	0.1	2.94	0.0015	5	9
3003	<0.1	3.0	0.0013	5	9
LCP	0.04	2.9	0.002	4	18

The substrate thicknesses, dielectric constants, and loss tangents of the three materials were chosen to be as close as possible. Any differences in device performance could then be reasonably attributed to variations from absorbed water content. Although the typical water absorption test is performed with bare samples, this experiment required it to be performed with passive devices on the substrate. Each 2" x 2" substrate had four 14 GHz microstrip patch antennas on the top side and full metallization on the back side. A picture of one such sample is shown in Figure 55.

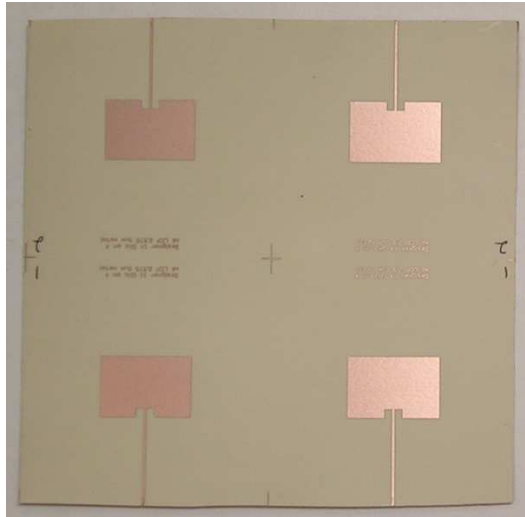


Figure 55. 2" x 2" test sample with four 14 GHz microstrip patch antennas.

For each substrate material, a control sample and a test sample were used. The control samples were used to establish that samples kept at room temperature with ambient humidity could verify stable weight and resonant frequency characteristics over the time duration of the testing. The control samples indeed maintained identical weight and resonant frequencies at all times during the several week testing period. As a result, the test sample differences were identified as direct results of the conditions administered to them.

5.3.2 Water Weight Gain

The standard IPC water absorption test was performed per specification using a digital scale with precision to the nearest tenth of a milligram to weigh the samples. For comparison purposes, all samples were weighed and measured “as fabricated” prior to the IPC testing. The test samples were then baked in an oven for over 1 hour at 110 °C. Each sample was removed individually and immediately weighed. The oven was located only a few feet from the scale, which was important in this measurement. The samples were observed gaining weight while on the scale, apparently from taking in water from ambient humidity. This weight increase was observed in real time on the scale’s digital readout over the course of a few minutes until the readings settled at the pre-bake weight values. The actual weights from the “as baked” and “in air” states are shown for each material in Figure 56. The

humidity in the room was 36%.

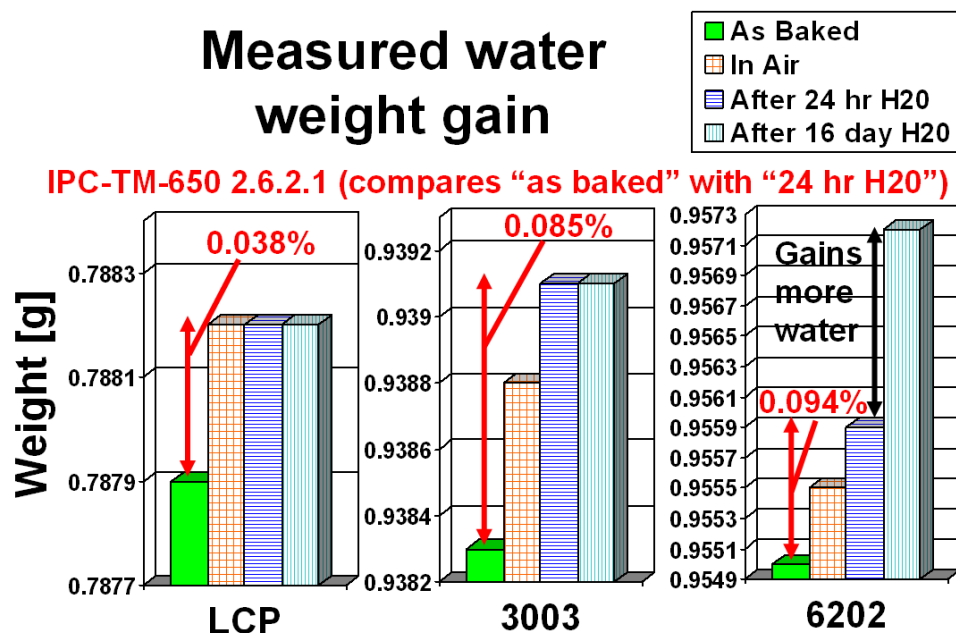


Figure 56. Measured sample weights to the nearest tenth of a milligram for the following cases: 1) Immediately after baking in an oven at 110°C for 1 hour; 2) Dry, at room temperature and ambient humidity; 3) After 24 hours submersed on edge in distilled water, the surface water dried thoroughly upon removal, and the sample measured immediately; 4) With the same method as 3) except after the samples were submersed for 16 days.

The test samples were next submersed on edge in distilled water for 24 hours. Each sample was removed independently from the water, the surfaces quickly and completely dried with paper towels, and weighed. The weight was recorded immediately upon placement on the scale and the value compared to that from the baked (dry) weight. The resulting water absorption percentages, shown in Figure 56, are consistent with those provided by the manufacturer, whose values are listed in Table 10. Once again, the weight was observed to change quickly in real time, this time as the water embedded in the substrate evaporated. Five minutes after removal from the water, all of the substrates had converged from the “after 24 hr H2O” weight to their “in air” weight.

To ensure that the IPC test results are representative for longer submersion times, the samples were dunked in water for 16 days and the same weighing procedures re-administered. The LCP and 3003 samples did not show additional water uptake, while

the 6202 sample more than doubled its initial water absorption amount. The measured values are displayed in Figure 56. The two lower water absorption materials could be assumed to be saturated and perhaps could be expected to stay the same with extended water exposure times. However, the 6202 material seemed to accumulate additional water with time. The calculated water absorption percentage for the 6202 sample after 16 days was 0.23%, which is not a desirable level for a packaging material.

A surprise from these tests was the short time needed for the sample weights to revert to the ambient “in air” values from both the baking and submersion tests. The most rapid weight changes occurred in the first minute or two after an environment change and the absorption/desorption process could generally be assumed complete within 5-10 minutes. As an example of the speed of this process, the 3003 sample that had been underwater for 16 days, settled at the original “in air” weight in 1 minute.

Another interesting aspect of these tests was that LCP showed zero change (0.0 mg) from the ambient “in air” state to the states after both submersion tests. Similarly, the 3003 material gained only 0.3 mg (0.032%) from the “in air” to the submerged states. In operating environments, the water content of the substrates would realistically be expected to fall between these values since a perfect zero water content (zero humidity) is not likely on Earth. As a result, the author believes it may make more sense to compare the “in air” state with the saturated state unless the substrates are being evaluated for space applications. A summary of the potentially more useful water gain result comparing the “in air” and “after 24 hr H₂O” values is shown in Table 11. Note that 6202 is not included in the comparison due to its potential for increasing water uptake with time.

A conclusion from these water weight gain tests is that two of the three substrates absorbed little to zero water between the ambient state and the submerged state. The same results held, even when the submersion time was much longer than that for the standard IPC characterization test. Another result is the fast (few minute) acclimation time of the substrates to reach their equilibrium weight (the “in air” weight) from both the baking *and*

Table 11. WATER ABSORPTION COMPARED WITH “IN AIR” CONDITIONS

Note: The measured absorption values using the IPC test are provided as a comparison.

Material	Measured Water Absorption Using IPC Std. [%]	Water Absorption From “in air” to “after 24 hr H2O” [%]
3003	0.085	0.032
LCP	0.038	0.000

submersion test weights.

5.4 Passive Device Sensitivity to Water Absorption

Water’s dielectric properties are known to be far different from common materials, which is one of the main reasons its absorption into RF substrates is problematic. At a few GHz the dielectric constant is about 80 and between 10-100 GHz water undergoes a dielectric relaxation effect. The relaxation corresponds to a dielectric constant drop from 80 to about 5 and a drastic increase in loss. In order to pick an operating frequency that is sensitive to both the high dielectric constant and loss of water, 14 GHz was selected, which has $\epsilon_r = 50$ and $\tan \delta = 0.5$ [4]. At 14 GHz, water’s dielectric constant is about 17 times that of our test samples and the loss tangent is at least 250 times greater.

5.4.1 Device Selection

A passive device that is sensitive to both dielectric property changes and that is likely to be implemented in these organic materials is a microstrip patch antenna. Changes in the bulk dielectric constant from water absorption are expected to shift the resonant frequency while the loss tangent should increase insertion loss and decrease the depth of the resonance. Ansoft Designer 2.5D planar electromagnetic solver was used to design a 14 GHz microstrip patch antenna on each of the three substrates. Although the dielectric properties and thicknesses of the materials are very similar, an independent design was performed for each material.

5.4.2 Fabrication

The antennas were fabricated in the Georgia Tech MiRC cleanroom using photolithography and ferric chloride copper etchant to define the patterns. Each sample had alignment marks on the substrate that formed a 2" square so that the substrates could be easily cut to the specified 2" x 2" size for the IPC water absorption testing.

5.4.3 Measurement

An important lesson from the water weight gain tests was that a fast connection and measurement would be critical for observing the electrical effects due to water absorption. With this in mind, a special fixture with an adjustable RF signal pin height was used for the measurement. First, a 1-port SOLT calibration was performed on an Agilent 8510C network analyzer. Prior to official testing, the pin height was calibrated to the desired substrate thickness with the control samples such that a sample with the same thickness could slide under the pin quickly (with some friction) and to be held in hard mechanical contact. The procedure for placing an antenna on the fixture, positioning the feed line properly in hard contact beneath the signal pin, and beginning a measurement could thus be done in about 10 seconds. To determine the repeatability of such a measurement method, the control substrate antennas were measured several times by removing/replacing them and re-measuring. The measurement repeatability is estimated to be within ± 5 MHz which corresponds to $\pm 0.036\%$ at 14 GHz.

Prior to subjecting the test antennas to the baking or water submersion tests, they were all measured. It is important to note that this initial measurement corresponds to the substrate condition which has the "in air" weight. The resonances from these initial measurements were compared with those taken upon removing each substrate from the 24 hour and 16 day submersion tests. The LCP and 3003 results after 16 days were predictably the same since they measured identical water absorption amounts for both time periods. The 6202 results were shifted significantly more after the 16 day submersion. A summary of the results is shown in Figure 57.

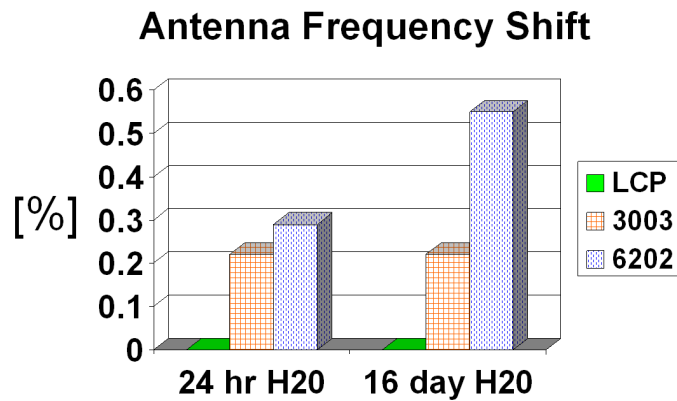


Figure 57. Measured frequency shift of 14 GHz microstrip patch antennas for the two submersion cases as compared with the resonant frequency from the “in air” case.

Each of the measurements was performed on 4 antennas per material and the results averaged. The consistency of measurements was generally excellent.

As an example of the most extreme frequency shift, the measurements from the 16 day 6202 sample is shown in Figure 58. Immediately upon removal from the 16 day water submersion, a resonance shift of 0.55% was observed, which is approximately half way out of band. However, these antennas have inherently narrow bandwidths due to the substrate thickness of slightly less than $0.01\lambda_G$ at 14 GHz. More attention should be paid to the magnitude of the shift, which may be insignificant for a 15% bandwidth antenna, but could be critical for an antenna for a bandwidth of a few percent. The worst case shift for the 3003 substrate was only 0.22% and that for LCP was undetectable with the 0.036% measurement resolution.

These antenna tests demonstrate an insignificant effect on two of the three substrates from even the worst case water absorption scenario - full immersion. Even if directly exposed to rain and high humidity, these low absorption organic materials would not likely reach the same level of water uptake as seen in the tests. In practical applications, the 3003 substrate would not be expected to approach the 0.22% worst case shift and the LCP substrate would be expected to stay extremely stable (no shift) as demonstrated in this testing.

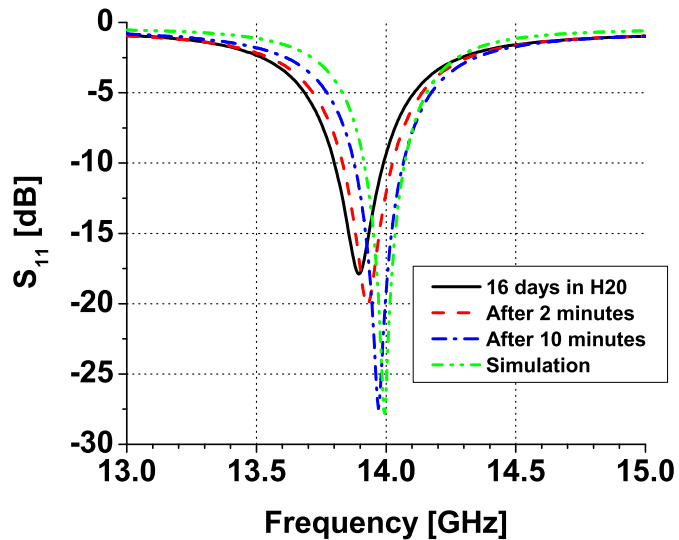


Figure 58. Frequency shifts of the worst case 14 GHz antenna on the 6202 substrate after the 16 day submersion in water. This plot corresponds to the 0.55% frequency shift case from Figure 57. Successive traces are of the same antenna after waiting 2 minutes and 10 minutes for the water embedded in the board to evaporate. After 10 minutes the response is identical to the dry measurement made before the submersion. The original trace for the dry measurement is not shown to reduce plot clutter. Also shown for comparison is the antenna simulation result.

5.4.4 Corrosion

A side note about practical implementation of packaged systems using these organic materials is that the standard copper metallization should have some passivation layer to protect the copper from corroding. Some techniques for accomplishing the passivation would be to sputter a thin gold layer on the top of the copper, or in the case of a copper trace on LCP, a lamination can be carried out to cover/seal the copper metallization inside a multilayer LCP stackup. This technique has been used with the 35 GHz antenna elements in [50]. An example of why a passivation layer is necessary for copper is shown in Figure 59.

5.4.5 Passive Device Sensitivity to Water Conclusion

Tests have been performed to determine the water absorption characteristics of three low absorption organic substrates. The dielectric substrate weight returns to the ambient equilibrium weight after exposure to submersion and baking processes in as short as 1 minute. Two of the three substrates were found to possess exceptional dielectric stability as demonstrated by minimal (0.22% to 0.0%) frequency shifts by 14 GHz microstrip patch antennas.

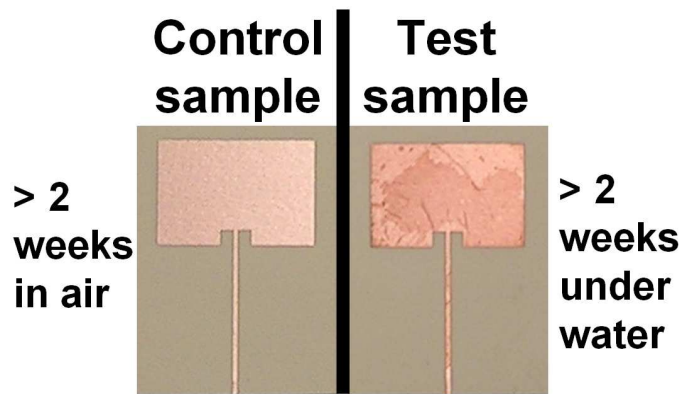


Figure 59. 14 GHz microstrip patch antennas on a control board which was kept in air at ambient humidity vs. an antenna that was submersed in distilled water for 16 days. The submersed antenna demonstrates the corrosion that can occur due to moisture interaction with copper.

Specifically, LCP showed no detectable change in its antenna performance from full submersion, even after an extended length of time. The measured water weight gain in LCP occurred primarily between the baked state and that at ambient humidity. It did not gain a measurable amount of water from direct water contact. As a result, LCP passive device performance is expected to be very stable to changes in humidity or rain. The negligible changes in LCP's weight and 14 GHz antenna performance indicate that its near-hermetic classification is desirable for both cost and performance in reliable, packaged RF and mm-wave systems.

CHAPTER 6

LCP ACTIVE DEVICE PACKAGING AND TESTING

In academia, solid state devices such as pin diodes on a bare die have been placed on top of an LCP substrate and connected [17]. In addition, several companies have recently developed injection molded LCP packaging caps [55, 56], which can be used to seal individual components with epoxy or laser sealing. The laser sealing requires a glass backing and an LCP contact area impregnated with carbon black to absorb the laser energy. These packages can be bulky, which may limit the packaging integration density. And the rigid packaging “caps” (LCP becomes rigid when it has sufficient thickness) can take away one of the LCP substrate’s very unique characteristics – flexibility.

In this research, methods are investigated to create a new kind of LCP package consisting of laminated thin-film LCP layers. This method offers the benefits of minimizing the package size, weight, and cost while integrating active devices inside of a package that is shared with the embedded passives. Research was necessary on several aspects of this package type to ensure/debunk the feasibility of creating mm-wave RF modules in multi-layer LCP substrates. The potential difficulties that were investigated are:

- Dielectric/impedance discontinuities and package parasitics at package cavity interfaces.
- Active device survivability through an LCP lamination process.
- Matching the coefficient of thermal expansion with embedded active devices.
- Seal integrity for packages with transmission lines passing directly between layers.

A failure from any of these considerations could have precluded multilayer LCP packaging from being a desirable method for creating low-cost, compact RF and mm-wave modules with this material technology. Each of the items described above are investigated

in this chapter. The results are all promising endorsements for the implementation of RF systems in LCP packaging topologies.

6.1 Package Interconnect

Traditionally, with high dielectric constant materials, introducing air cavities ($\epsilon_r = 1$) inside of multilayer RF modules for embedding chips or other elements creates impedance discontinuities that cause reflections and can destroy RF performance. In addition, many package cavities rely on metal bonding rings around the cavity interface, which necessitates more difficult feedthrough solutions such as re-routing and tapering the transmission line underneath the seal [57, 58]. A unique possibility with LCP, because of its low dielectric constant and multilayer lamination capabilities, is to form cavities in the substrate before lamination to provide “sandwiched” all-LCP constructions that can pass transmission lines directly through the package interface with negligible effects on the RF performance.

Since LCP has a low dielectric constant near 3.16 [20] (close to free space $\epsilon_r = 1$), impedance mismatches were found to be minimal when an LCP superstrate layer is added on top of a standard transmission line. In addition, if cavities are micromachined in the superstrate layer, they do not create large impedance mismatches at the cavity interface. Figure 60 shows three different transmission line cross sections and the impedance difference between them. The first cross section is a standard conductor-backed finite ground coplanar (CB-FGC) line, the second includes a 4 mil superstrate packaging layer, and the third has a 2 mil laser machined cavity in the superstrate layer. Because the impedance difference between a transmission line with a superstrate and one with the cavity cross section only varies by approximately 4Ω , the reflections are minimal.

These cross sections were simulated with Ansoft HFSS to find the respective impedances. Then, to determine the effects of varying the lateral cavity dimensions, the impedances of each cross section were input into Agilent ADS and a circuit model was simulated for all electrical length combinations of transmission lines with these impedance discontinuities.

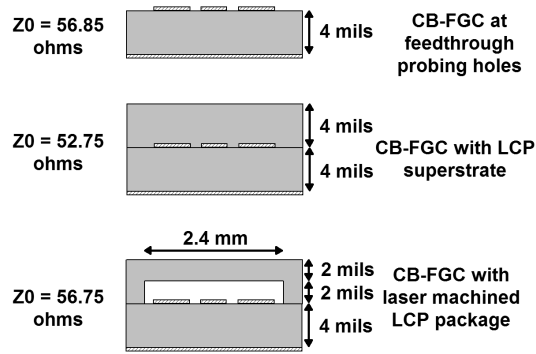


Figure 60. Three different FGC cross sections present in the measured packaging structures. Impedance values are from HFSS 3D simulator for an FGC with signal width $S=200\ \mu\text{m}$, gap $G=120\ \mu\text{m}$, and $\epsilon_r = 3.16$. Z_0 only differs by $4\ \Omega$ in the three different cross sections.

With $Z_0 = 53\ \Omega$ and $57\ \Omega$ for our two segments of transmission line the *worst case* value obtained for any combination of feed line lengths and cavity lengths is $S_{11} = -17.7\ \text{dB}$ (1.7% power reflected). Most combinations yield S_{11} below $-20\ \text{dB}$ and the optimal transmission line length and cavity length combinations yield S_{11} close to $-40\ \text{dB}$. Because S_{11} values less than $-20\ \text{dB}$ correspond to power reflection $< 1\%$, the package cavity size can be chosen almost at random to fit any desired device. Figure 61 shows an optimal design for 20 GHz operation where the feed line lengths are $\lambda_G/4$ at 20 GHz and the cavity size is swept from $\lambda_G/24$ to λ_G .

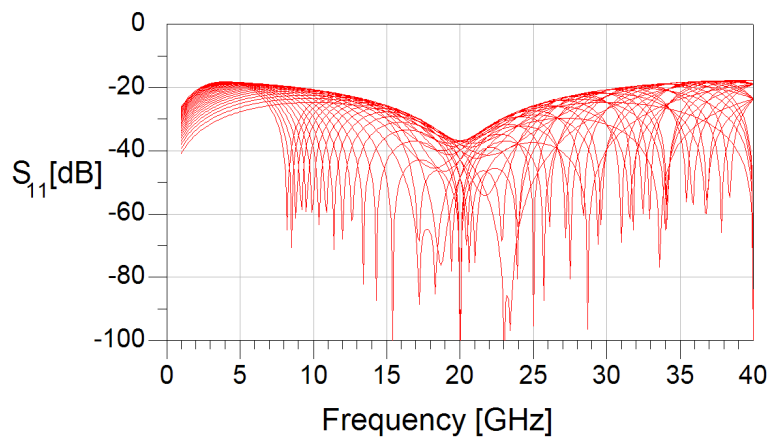


Figure 61. S_{11} for cavities with electrical lengths from $0\text{--}360^\circ$. The CB-FGC in the cavity has $Z_0 = 57\ \Omega$ and the CB-FGC with superstrate feeding the cavity has $Z_0 = 53\ \Omega$. The feeding CB-FGC lines are $\lambda_G/4$ at 20 GHz which is an optimal configuration for minimizing the already low reflections.

A conclusion drawn from the simulation results is that LCP's low dielectric constant could enable package cavities of arbitrary size to be integrated in a superstrate packaging layer to accommodate chips, MEMS, or other devices without concern for the parasitic packaging effects. The LCP superstrate layer can be bonded with a low melting temperature LCP bond layer to create an all-LCP package.

Several advantages of this technique are that the flexibility of the substrate is maintained for applications such as conformal antennas, the package is lightweight, and the LCP packaging layer is a standard inexpensive microwave substrate that can be made into any system-level package configuration. In addition, it presents a new way to package multiple devices located across an LCP substrate and the package fitted across both the transmission lines and the devices at once.

6.2 MEMS Switch Package

To determine the RF characteristics of the thin-film LCP packaging structure with an actual device, a demonstration involving an excimer laser micromachined thin-film package for encasing air-bridge type RF MEMS switches was performed [59]. A 4 mil non-metallized LCP superstrate layer with a 2 mil depth-controlled laser micromachined cavity was investigated as a package layer for testing the RF parasitic effects of the package on the MEMS switch. The 2 mil (51 μm) deep laser-machined cavity allowed plenty of clearance for the switch membranes, which are only elevated about 2 μm above the base substrate. To accommodate devices that require more vertical clearance, multiple LCP layers could be stacked together.

RF MEMS switches were fabricated by group members Nickolas Kingsley and Guoan Wang on LCP substrates. The switches are comprised of a 1 μm thick electroplated gold doubly supported air-bridge layer suspended approximately 2 μm above the lower metal layer. The 100 x 200 μm membrane is suspended over the signal line of a CB-FGC transmission line and anchored to the ground planes on both sides. A microscope picture of the

MEMS switch on LCP is shown in Figure 62.

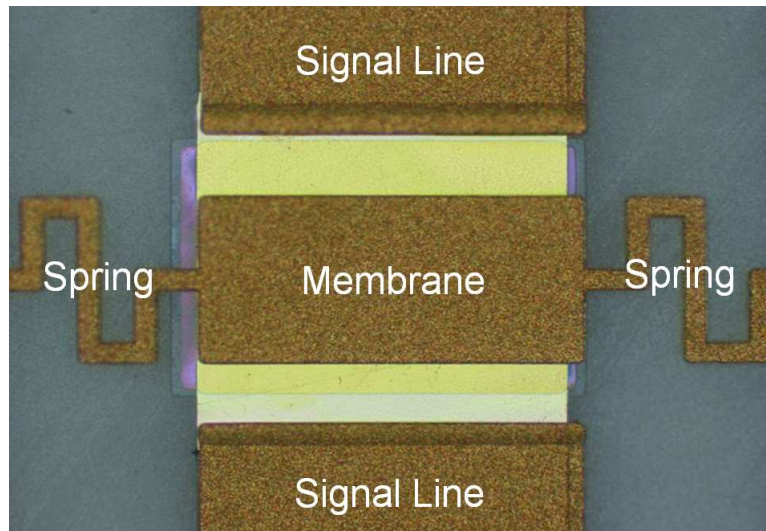


Figure 62. Air-bridge type MEMS switch on an LCP substrate. The springs anchor the membrane to the CB-FGC's ground planes [not shown]. Note: Dark brown is electroplated gold. Yellow is evaporated gold.

In the default state, the membrane is up, in which case full signal transmission should take place. When a DC actuation voltage is introduced, the membrane is flexed down into contact with a thin silicon nitride layer between the two metal layers and creates a capacitive short circuit that blocks signal transmission. The signal blockage is only optimized in a narrow frequency band due to the LC resonance of the inductive meander line springs and the capacitance created between the membrane and the signal line.

LCP layers with 4 mil thickness were then laser processed to create alignment holes and the 2 mil deep package cavities. Alignment holes were drilled in the same relative locations in the packaging layers, the TRL calibration line substrate, and the MEMS switch substrate. The superstrate packaging layers were aligned by stacking them over a metal alignment fixture with four alignment pins, as seen in Figure 63.

Because MEMS switches are by nature fragile, an iterative measurement procedure was undertaken. First, the switches were measured in air to provide a base measurement case. The second and third measurements were done with the package layer aligned and held into contact with the base substrate. The first packaging iteration was done by gently holding

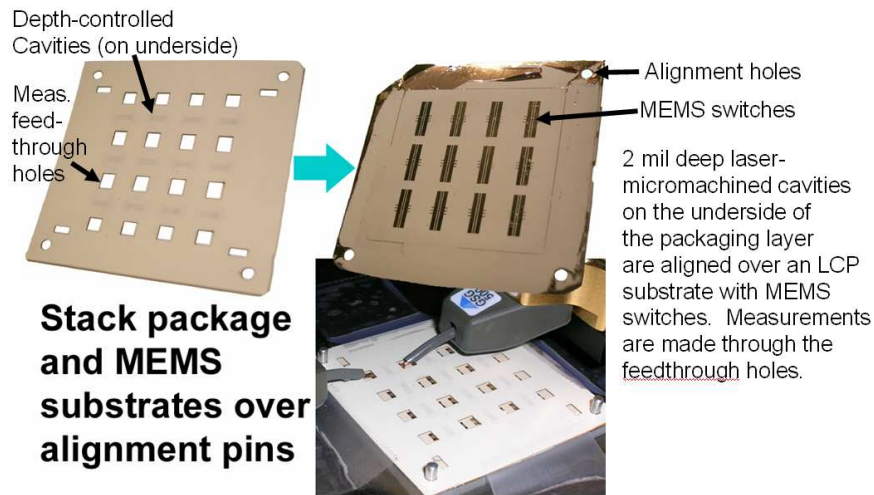


Figure 63. Top left: LCP superstrate packaging layer with holes for alignment and probe feed-throughs. The packaged cavities between each set of probing holes are visible due to LCP becoming partially transparent at a 2 mil thickness. Top right: CB-FGC transmission lines with air-bridge RF MEMS switches in the center of the transmission lines. Bottom right: Both layers stacked on alignment fixture and probed through the feed-through windows.

the package layer down over the MEMS substrate with tape. When the switches continued to operate with the package layer in place, this ensured that the alignment of the package cavities was successful. Finally, the top metal plate was placed over the alignment pins and a 15 pound weight was balanced on top of the samples to approximately simulate the pressure from a bonding process. The plate was removed and the samples were re-measured (still with the packaging layer held in hard contact).

Results for these measurements are seen in Figures 64 and 65. The S-parameters of the packaged switch and the non-packaged switch are nearly identical in both the up and down states. For example, the variation between the three measurement cases for S_{21} in the UP state only varies by an average of 0.032 dB across the entire measurement band. The other S-parameter comparisons with and without the package layer are also essentially identical.

To show the effects of the packaging layer and cavity on a simple transmission line, the switch membrane was physically removed and the circuit re-measured. The results of the bare transmission line with and without the packaging layer are shown in Figure 66. As expected from the simulations, the cases with and without the packaging layer are nearly

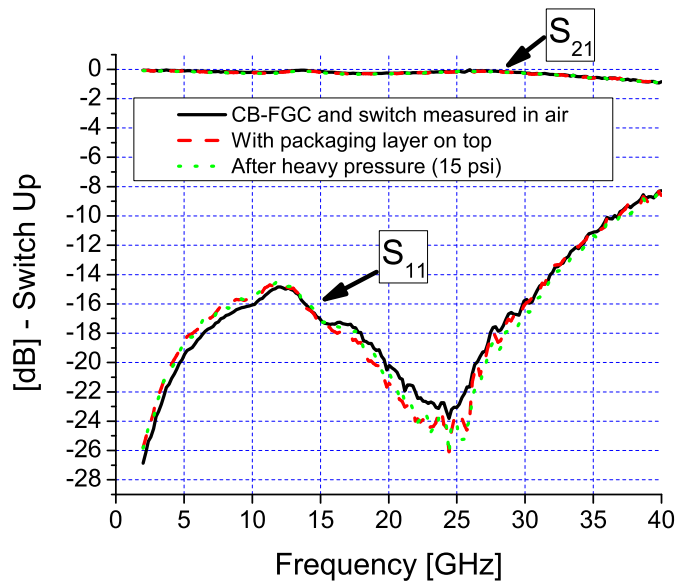


Figure 64. Comparison of S-parameter measurements of an air-bridge type CPW MEMS switch in the “UP” state. Case 1: The switch is measured in open air. Case 2: The packaging layer is brought down and taped into hard contact and measured. Case 3: A top metal press plate and a fifteen pound weight are put on top of the packaging layer (15psi) to simulate bonding pressure. The weight and the press plate are then removed and the switch was re-measured.

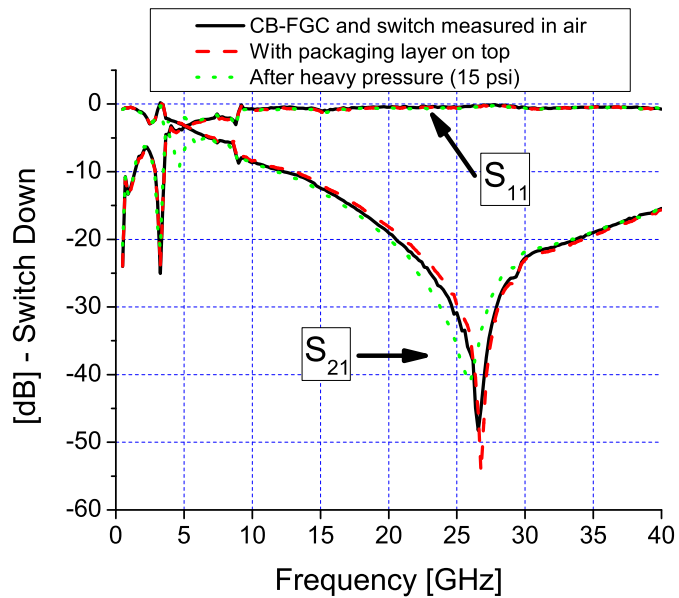


Figure 65. Comparison of S-parameter measurements of an air-bridge type CPW MEMS switch in the “DOWN” state. The three measurement cases shown are the same as those explained in the caption for Figure 64.

the same.

The RF characteristics of thin-film LCP packaging layers with laser micromachined

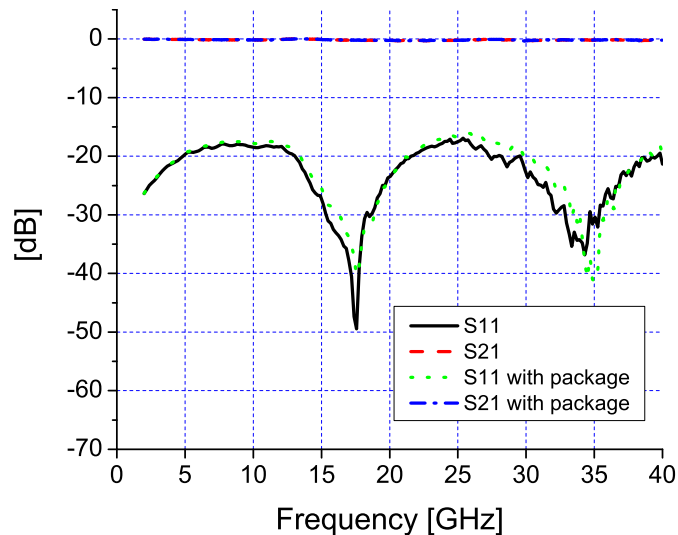


Figure 66. Comparison of S-parameter measurements of the MEMS switch transmission line after the switch was physically removed. The cases with the package and without the package layer are nearly the same.

cavities have been investigated for frequencies up to 40 GHz. Because of LCP's low dielectric constant, the air/dielectric discontinuities in these packaging structures were found to be insignificant. Thus, the package cavities can be designed with this method almost arbitrarily without concern for their effect on RF performance. To test this packaging structure, RF MEMS switches and plain transmission lines were fabricated and measured with and without an LCP packaging layer with air cavities (dielectric discontinuities). S-parameter measurement results showed little to no difference with or without the package. This interconnect technology could pave the way for simple, low-cost, near-hermetic, system-level packaging structures.

6.3 Microwave Monolithic Integrated Circuit (MMIC) Packaging

6.3.1 Packaging Concept

In addition to the single layer LCP packaging concept presented in the previous section, multiple layers of thin-film LCP can be arranged and laminated to form low-profile lightweight packaging structures for active devices. Low melting temperature LCP layers (285 °C) are used to adhere generally thicker high melting temperature core layers (315 °C) to create a homogeneous LCP package stackup. As mentioned before, the electrical properties of

high and low melting temperature are the same, which alleviates any concern for dielectric discontinuities. Laser or mechanical drilling can be used to selectively remove parts of certain layers in arbitrarily desired shapes, which, when laminated with solid layers, become cavities for embedded active or passive devices.

Since LCP comes commercially in 1, 2, and 4 mil thicknesses, the layers will require stacking to achieve the necessary thickness and cavity topology to encase an active device. In the MMIC embedding process presented in this research, a cavity must be formed above the chip so that the wire bonds have sufficient space to connect from the chip pads to the feeding transmission lines. This vertical clearance (on the order of 100 μm) is also important since in the final topology the bypass capacitor and chip will be elevated slightly by an electrically conductive cured silver paste that connects the components to the RF ground plane. Based on a lenient fabrication tolerance budget, on HFSS simulations, and on available LCP thicknesses, the final package test topology is shown in Figure 67.

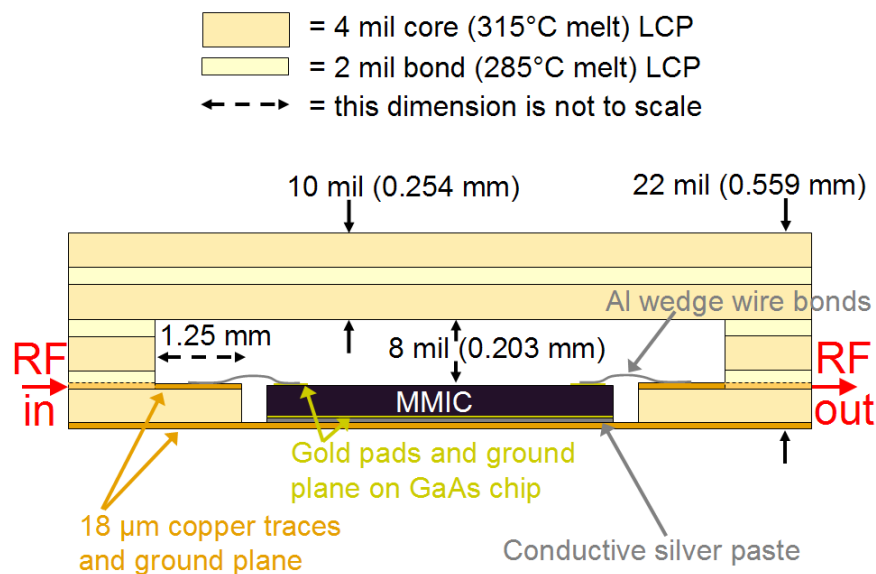


Figure 67. Pictorial side view of package stackup.

Matching the coefficient of thermal expansion (CTE) for the package, transmission lines, and semiconductor is important for system reliability. The MMIC has a gold ground plane (CTE = 14.4 [ppm/°C]), which is seated onto copper with silver paste, both of which

have a CTE = 17 [ppm/°C]. This close CTE match, as well as the 17 CTE of LCP in the xy -plane, ensure that thermally induced stresses are small on the package and die.

One key point about this package, discussed in the previous section, is that the feeding microstrip transmission lines have cross sections with slightly different impedances inside and outside of the cavity section. It was shown that due to LCP's low dielectric constant, these impedance discontinuities are minimal and have almost negligible RF effects. During the thermocompression bonding process, the low melting temperature LCP bond ply melts/conforms around the feeding transmission lines and creates a seal. The RF signal is then passed directly through the side of the laminated LCP stackup as seen in Figures 67 and 68.

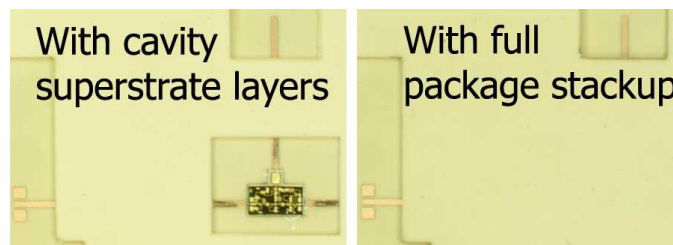


Figure 68. Comparison of the LCP multilayer package stackup. The left picture shows only the package layers with cavities. The right picture shows the full LCP package stackup.

6.3.2 Component Selection

To test the feasibility of embedding an active device in the thin-film LCP packaging topology, identifying a test component representative of those used in mm-wave RF systems was desired. In addition, the die should have compatible dimensions with the planned fabrication processes. Finally, the number of input/output connections for wire bonds was desired to be as low as possible for ease of assembly.

These requirements pointed roughly in the direction of testing either a GaAs amplifier or oscillator. An oscillator is generally more stable to impedance mismatches from external wire bond and package parasitics. However, a packaged circuit that is more sensitive to external matching is potentially more informative as an indicator of the package utility. That reasoning shifted the decision to a 13–25 GHz low noise amplifier die (model HMC342

from Hittite). This chip was selected since it was one of their smallest chips (2.02 mm x 1.06 mm) and it has the simplest connection (input, output, and one DC bias pad). Also, the 4 mil die thickness was perfect for embedding into a cavity in a commercially available 4 mil LCP sheet. And since GaAs is used well into the mm-wave spectrum, this is a die type that can be used for a wide variety components and frequency ranges.

An off chip bypass capacitor was one further component required by amplifier. To integrate the capacitor in the same topology as the chip, a 17 mil x 14 mil x 5 mil thick (0.43 mm x 0.36 mm x 0.13 mm) 130 pF parallel plate bypass capacitor from Presidio Components Inc. was selected.

6.3.3 Multilayer LCP Package Design Considerations

Several non-traditional concerns arose when considering the packaging of an MMIC inside of an LCP stackup that requires a 285 °C lamination process.

6.3.3.1 Wire Bonding

Problem: The wire used for the wire bond should have a melting temperature lower than LCP so that it does not melt the LCP substrate during the wire bonding process. But if the wire melts below LCP's melting temperature, then surviving a bonding process which is designed to melt the LCP will result in wire sagging or reflow.

Solution: Conveniently, wire bonders are able to create reliable metal-to-metal bonds without melting the wire, but with ultrasonic energy. This means the bond takes place at a low temperature far below LCP's melting point even though the wire's melting temperature is far above LCP's melting point. So the wire bonded connection sticks well even if it is heated to 285 °C and held there for an extended period of time. In our case, we used pure aluminum bonding wire which has a melting temperature of a safe 650 °C.

6.3.3.2 Other Electrical Connections (Solder, Silver Epoxies, etc.)

Problem: Solders and silver epoxies commonly have temperature limitations which occur in the 100–200 °C range. These materials are needed to create an electrical connection

between the electronic components and the RF ground plane. Solder commonly reflows below 250 °C, so any solder connections made before an LCP lamination process would likely float away, create a mess, and/or become disconnected. Silver epoxies are usually cured into their conductive state by baking between 100–150 °C for a short time. But all of the silver epoxies the author came across had maximum temperature ratings well below 285 °C. The material safety data sheets (MSDSs) showed that they had flash points, fume warnings, and carbonizing problems that made them unsuitable for use with LCP lamination. In addition to these debilitating issues, silver epoxies have high coefficients of thermal expansion (CTEs) ~35 to >100 (ppm/°C), which would induce undesired stresses at the contact points. So the question remained, how to create spot contact electrical connections that will survive an LCP bonding process?

Solution: After contacting many companies about suitable formulations without success, a single inorganic electrically conductive silver paste was located. It is good up to 649 °C and has the additional benefit of a 17 (ppm/°C) CTE, which is a perfect match to copper. The resistivity is also an excellent 0.0002 Ω-cm. The product is Pyro-Duct 597-A from Aremco.

6.3.3.3 *Chip and Bypass Capacitor Mounting With Silver Paste*

Problem: The physical process of mounting the chip and capacitor with the silver paste between them and the RF ground plane is quite a challenge. Because the chip and the capacitor are so small, depositing a measured amount of silver paste onto the desired conductive surface, ensuring an extremely thin and uniform deposition, and placing the silver paste covered component with sub 50 μm precision before the paste solidified seemed to be impossible without specialized equipment. For this research, it had to be done by hand.

Solution: The silver paste was far too viscous to meet any of the deposition requirements. However, it is water soluble. The paste was mixed with water until the consistency was similar to water, but with densely suspended silver particles. A droplet of this solution was picked up onto the tip of some extremely fine tweezers. The drop size was reduced

manually to the smallest possible size with some paper towels. Then the tip of the tweezers was touched to the exposed copper on the bottom of the cavity. The surface tension of water sucks the solution into the cavity. The chip and capacitor are then placed and floated on the water meniscus and can be positioned as the water evaporates. When the water completely evaporates, the components are left in contact with the ground surface, having a thin uniform silver paste film adhering them to it. A few hours of curing with heat further solidifies the bond and improves the electrical conductivity.

6.3.4 Package Fabrication

6.3.4.1 LCP Substrate Layer

The base layer for the package is a double copper clad 4 mil 3850 LCP sheet from Rogers Corporation. Precise alignment holes, as well as the perimeter dimensions, were cut through the double clad base substrate with a 1047 nm wavelength infrared laser. Next the feeding transmission lines were patterned on the top of the board using standard photolithography and ferric chloride was used to etch the copper. The transmission lines on the substrate include the chip feeds, a DC bias line, and a full through-reflect-line (TRL) calibration set.

After the patterning was completed, a KrF1 248 nm excimer laser was used to ablate a cavity for the chip and capacitor. A cavity was created in the polymer all the way down to the 18 μm Cu back-side metallization, which works as an excimer laser stop layer. The laser cutting leaves behind some carbonized LCP residue in a small region around the cavity. An oxygen plasma clean was then used to remove this thin residue. Next, the manual capacitor and chip placement were performed with the special high temperature inorganic conductive silver paste. These assembly steps are shown graphically in Figure 69.

A closeup of the completed component placement is shown in Figure 70.

6.3.4.2 LCP Superstrate Layers

The LCP layer thicknesses selected for the superstrate packaging layers were 2 mil low melting temperature bond ply (285 °C) layers and 4 mil high melting temperature core layers (315 °C). The 2 mil bond ply has sufficient thickness to melt uniformly over the

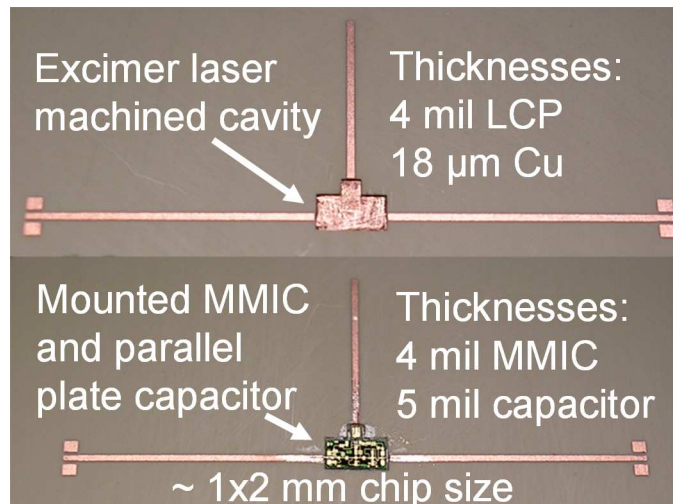


Figure 69. Comparison of the LCP laser machined base layer before and after the MMIC and parallel plate capacitor were mounted with an inorganic silver paste and wire bonded to the feed lines.

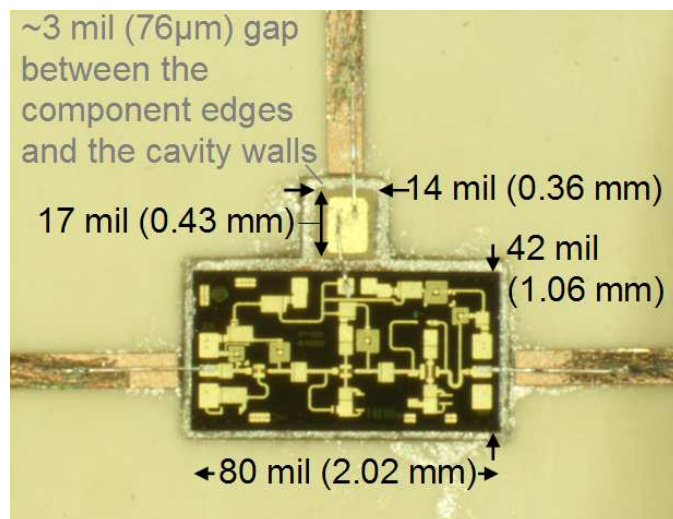


Figure 70. Hittite HMC342 13–25 GHz GaAs LNA and a 130 pF parallel plate bypass capacitor attached inside of an excimer laser micromachined cavity in a 4 mil LCP substrate. Aluminum wedge wire bonds connect the components to the feeding transmission lines.

18 μm thick feeding transmission lines. The 4 mil core layers are thick enough that when two of them are bonded together (with 2 mil bond ply) into a 10 mil total thickness, the mechanical rigidity is high enough to prevent the top membrane layer above the cavities from deflecting down toward the chip. However, to ensure the top membrane layer is laminated uniformly, even above the cavity, the top three LCP layers were first pre-bonded, then laminated with the rest of the stackup.

The superstrate packaging layers were machined with a CO₂ laser to form square holes in some layers for the chip cavity while leaving other layers solid to create a sealed cavity once laminated. All of the layers, including the base substrate had laser cut alignment holes in the same relative locations to enable precise stacking on an aluminum bonding fixture. The final laminated package is shown on the fixture with the top press plate removed in Figure 71.

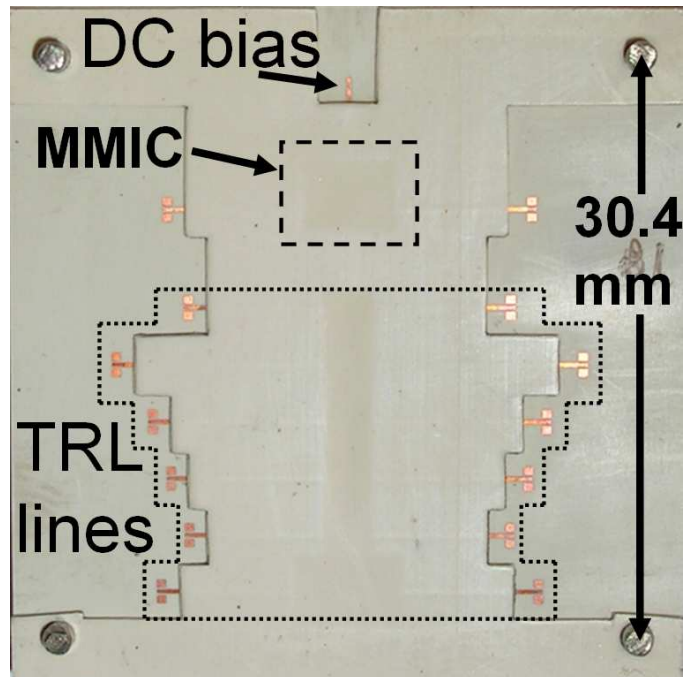


Figure 71. Top view of the 13-25 GHz GaAs MMIC packaged in multiple thin layers of LCP.

The 2 mil bond ply was unclad and the 4 mil pieces required the double sided copper to be etched off before laser processing. The bare LCP is quickly cut into the desired shapes with a CO₂ laser. The superstrate layer cavities, alignment holes, and the sample perimeters were all cut with the CO₂ laser. To clean the carbonized LCP residue left around the cut edges, an oxygen plasma was again used to clean both sides of each of the packaging layers.

6.3.4.3 Wire Bonding

The wire bonds were performed with a Marpet Enterprises Inc. wedge wire bonder with 1.5 mil diameter aluminum bond wire. A wedge bonder was ideal for this application since

it is capable of creating a nearly flat wire from pad to pad. This wire flatness is important for minimizing the height of air cavity above the bonds, which means only a few stacked LCP layers are necessary for creating sufficient clearance between the wire bond and the top package layers. In addition, the wedge bonder creates a “cool” bond by using ultrasonic energy to fuse the contact points. Each sample required four bonds – one to each of the RF input and output pads, one from the chip’s DC bias pad to the bypass capacitor, and one from the bypass capacitor to the DC bias transmission line.

Wire bonding is usually done with 80/20 gold/tin or aluminum bond wire and the preferred pad materials are gold, aluminum, or titanium. These materials are selected due to their inherent “stickiness” which ensures a good bond. For the first iteration, 4 μm of aluminum was sputtered and patterned to follow these material guidelines. However, the wire would not stick to the sputtered aluminum. Since LCP comes double copper clad with a high quality electrodeposited copper, the wire bonder was then tested with the copper, and against the common practice, it stuck well. As a result, the base substrate was re-fabricated with copper traces and the aluminum bond wire connected the gold pads on the chip and capacitor to the copper feed lines. In a commercial product, the same metal would be desired for the feeding transmission lines, wire bonds, and MMIC metallization for reliability purposes.

6.3.4.4 Assembly

The base substrate and the upper LCP package layers were aligned and stacked using the small aluminum fixture described in chapter 4. Since all of the LCP layers have laser cut alignment holes through them, the layers are easily stacked over the pins. The top aluminum plate then slides over the stackup. The entire stackup was then laminated with a thermocompression bonding process in the Karl Suss SB-6 silicon wafer bonder as detailed in chapter 4.

6.3.5 MMIC Measurements

An 8510C network analyzer was used to measure the amplifier from 12–26 GHz (the 13–25 GHz specified amplifier range plus a 1 GHz buffer on either side). A TRL calibration placed the measurement reference planes at the wire bond locations near the ends of the feeding microstrip transmission lines. A Keithley DC power supply provided the 3V amplifier bias voltage.

The LNA was first measured without the packaging layers, and then after the chip was packaged with an LCP thermocompression bonding process. The pre-bond and post-bond gain measurement of the chip are compared and also shown against the manufacturer's measurement specification in Figure 72. The result shows that the gain produced by the chip after the packaging process (45 minutes at 285 °C with ~300 psi tool pressure) is nearly the same as that before the packaging process. The effects of the package's dielectric discontinuity and the heat/tool pressure of the bonding process are thus shown to have minimal effects on the embedded/package MMIC performance. In addition, all of the measurements are close to the manufacturer's specification with and without the package layers in place. This result of a working MMIC after the LCP lamination process is excellent news since the lamination temperature isn't far from the manufacturer's 320 °C temperature warning, at which a chip is not to be held for >20 seconds.

The reflection characteristics (S_{11}) of the packaged LNA vs. the company specification are shown in Figure 73. The packaged S_{11} is slightly better than the company specification, though it is within 10% of the specification across the operating frequency range. The improved S_{11} could be due to differences in the inductance from the input wire bond and the calibration method used for the packaged chip vs. that used by the manufacturer. The general S_{11} shape is very similar for both measurements and the packaged chip shows excellent input reflection characteristics, indicating it is well matched in the packaged state.

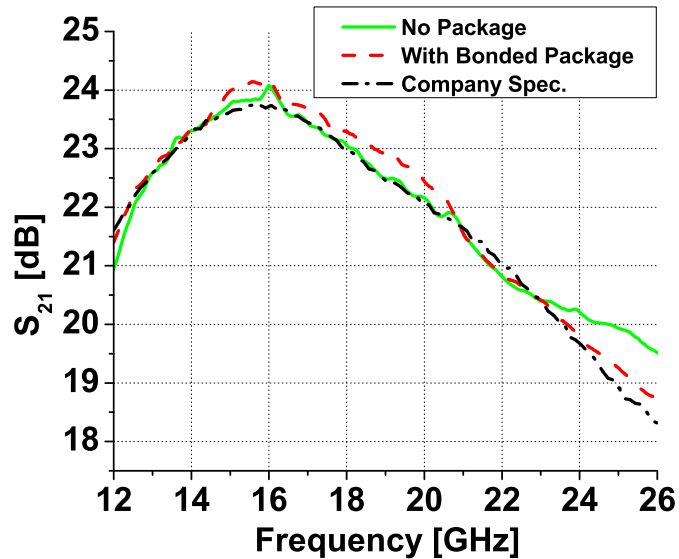


Figure 72. Gain measurement of the Hittite HMC342 13–25 GHz LNA. The chip measures very similarly with or without the LCP package. The package presence and package lamination process show no significant effect.

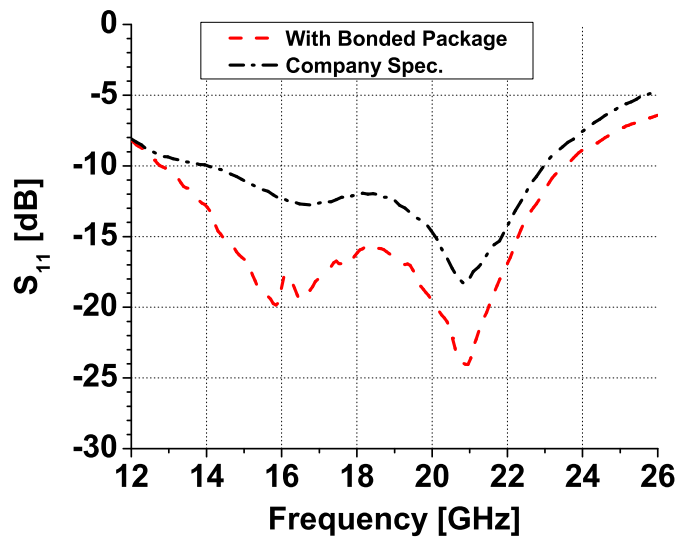


Figure 73. S_{11} measurement of the Hittite HMC342 13–25 GHz LNA.

6.3.6 Packaged MMIC Conclusion

The feasibility of an LCP multilayer packaging topology that can accommodate embedded MMICs up to the mm-wave frequency range has been demonstrated for the first time. Processes have been developed to laser micromachine LCP layers to create multilayer LCP package cavities and to embed chips/capacitors with a special high temperature inorganic

conductive silver paste. Measurements show that active device assemblies survive the standard LCP bond process and perform similarly to the pre-bonded state. This result and the unique fabrication methods presented are encouraging developments for enabling integrated RF modules with actives and passives laminated together into all-LCP 3D system-on-a-package RF front ends.

6.4 MMIC Package Water Seal Testing

An important proof-of-concept for the thin-film MMIC package is to show that a seal can be created around the 18 μm thick feeding transmission lines. These transmission lines pass directly through the side of the package stackup and require a 2 mil (50 μm) low melting temperature LCP bond layer to melt and conform around them to create a seal. Figure 67 showed a scale representation of the height of LCP's default metallization to the height of the bond ply. A closeup picture of the actual transmission line feedthrough, which demonstrates the ability of the LCP material to conform around the transmission line, is shown in Figure 74.

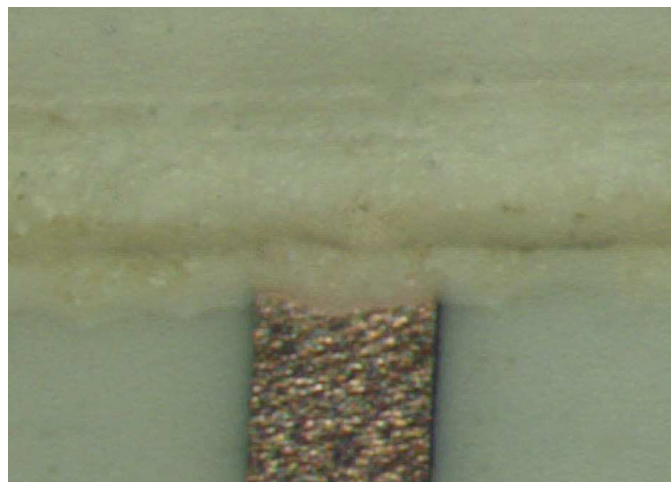


Figure 74. 18 μm thick LCP transmission line passing directly through the side of a bonded superstrate package stackup.

To test the package seal, the packaged MMIC was submersed in water for 48 hours. The sample was held on edge while underwater to encourage any potential cavity leaks to

be breached. A TRL calibration was performed with an identical alternate sample so that the measurement of the packaged chip could be made immediately upon removal from the water. The gain of the packaged MMIC was then measured and compared with the gain before the submersion test. The results of this test are shown in Fig. 75.

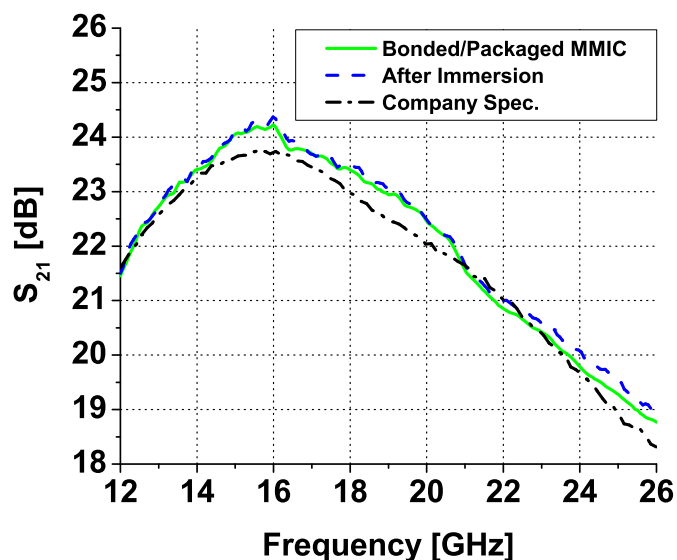


Figure 75. Gain measurement of the Hittite HMC342 13–25 GHz LNA. The first measurement is of the packaged/bonded MMIC. The second measurement was done immediately after the packaged MMIC was submerged in water on edge for 48 hours. The match of the measurements demonstrates a successful seal by the LCP package. The minimal water absorption into the package shows no significant effect on the MMIC performance.

The gain measurement in the before/after states is identical, indicating that the MMIC package formed out of multilayer LCP is a method that can be used successfully for packaging active devices.

CHAPTER 7

CONCLUSION

Liquid crystal polymer has been thoroughly investigated as a mm-wave substrate and packaging material. The broadband dielectric properties (up to 110 GHz) have been determined for the first time and validated with ring resonator and cavity resonator methods. The dielectric constant is low and stable near 3.16 from 30–110 GHz, and the loss tangent linearly increases according to equation 4, found in chapter 3. The values obtained are relatively low even up to mm-wave frequencies. The losses per unit length of the three most common types of transmission lines; microstrips, CPWs, and CB-CPWs and have all been measured, each on several different substrate thicknesses, and the results provided as a design guide for real world transmission line loss. These results are useful to the designing for creating power loss budgets for feed line networks for antenna arrays, for example.

The dielectric stability vs. temperature has been determined, not just at 10 GHz as is standard on data sheets for almost all commercially available microwave materials, but also at frequencies approximately every 10 GHz up to 105 GHz. LCP's thermal coefficient of dielectric constant, τ_{ϵ_r} , was found to be better a majority of high performance RF substrates. This statement is even more substantial since it compares LCP's average τ_{ϵ_r} value of -42 [ppm/°C] across the entire 11–110 GHz range, with other thermal stability values which are only available at 10 GHz. Transmission line loss per unit length at elevated temperatures was provided as a guide for circuits expected to heat significantly due to high power levels, or due to a hot surrounding environment.

Processes were developed to enable the fabrication of novel multilayer LCP RF and mm-wave circuits. A difficult lamination process with a tight temperature tolerance was developed. Three different laser systems were investigated for micromachining LCP. The findings of using CO₂, infrared, and excimer lasers as they apply to LCP processing are

reported. These systems allowed the formation of precision LCP parts and packages. Special thin-film LCP packaging structures were enabled through the capabilities of the laser system investigations. A multilayer alignment process was also developed to allow precise registration between stacked LCP layers.

Passive components on LCP were designed and measured successfully. Several design generations of multilayer dual-frequency dual-polarization 14/35 GHz antenna arrays for a NASA contract were enabled through the processes developed. The quantization of the effects of water absorption on LCP was performed, comparing it with two other RF materials with water absorption rated at 0.1% or less. Water weight gain for LCP was found to be insignificant. In parallel with the water weight gain study, 14 GHz microstrip patch antennas were used as sensing elements to determine the sensitivity of passive devices to the change in substrate water content. Similar to the water weight gain results, LCP was shown to be so stable that the frequency and resonance level of antennas on substrates exposed to water was not distinguishable from the ambient case.

To provide a solution for integrating active devices within all-LCP RF and mm-wave modules, a new concept of thin-film LCP packaging was developed. This low-profile packaging topology allows low-cost, light weight, packages which are able to have a coefficient of thermal expansion match to both metal traces and semiconductors. In addition, it allows system-level packaging of actives *and* passives with a relatively low temperature lamination process (compared to LTCC). In this research, active devices were shown to survive the LCP lamination process and to perform essentially the same with or without the presence of the package. A 13–25 GHz low noise amplifier die was the primary active device used for the proof-of-concept for embedding MMICs in laser micromachined LCP packages. The MMIC package was shown to be sealed around the transmission lines feeding directly through the side of the package stackup. As a result, the packaged MMIC measured identically before and after submersion testing.

In summary, this research has extracted LCP's important material properties as they pertain to designing mm-wave circuits on LCP substrates and packages. It has developed processes which enable unique multilayer fabrication processes and circuit/package/module topologies. The result is an expanded understanding of the key parameters, capabilities, and principles for the active/passive device integration in the LCP material technology with the goal of enabling RF and mm-wave multilayer organic packaged systems.

REFERENCES

- [1] A. Matsuzawa, "RF-SoC - expectations and required conditions," *IEEE Trans. Microwave Theory Tech.*, vol. 50, no. 1, pp. 245–253, Jan. 2002.
- [2] S. Taylor, Intel Corporation, on-campus presentation. Apr. 2005.
- [3] K. Lim, et. al., "RF-SOP for wireless communications," *IEEE Microwave Magazine*, vol. 3, no. 1, pp. 88–99, Mar. 2002.
- [4] R. Buchner, J. Barthel, and J. Stauber, "The dielectric relaxation of water between 0°C and 35°C," *Chemical Physics Letters*, vol. 306, no. 1-2, pp. 57–63, June 1999.
- [5] Rogers Corporation advanced circuit materials website. [Online]. Date accessed: Dec. 2003. Available: <http://www.rogerscorporation.com/acm/index.htm>
- [6] Taconic microwave materials website. Various materials data sheets. [Online]. Date accessed: Jul. 2005. Available: <http://www.taconic-add.com/>
- [7] H. Cunningham, Thunderline-Z, Personal communication at the IMS exhibition. June 2005.
- [8] Kyocera website. [Online]. Date accessed: Feb. 2006. Available: <http://americas.kyocera.com/kai/semiparts/pdfs/DesignGuide.pdf>
- [9] D. Karaboga and K. Guney, "A simple formula obtained using tabu search algorithm for the radiation efficiency of a resonant rectangular microstrip antenna," *Turk J Elec Engin*, vol. 7, no. 1-3, pp. 19–28, 1999.
- [10] R. Kulke, M. Rittweger, P. Uhlig, and C. Gunner, "LTCC - multilayer ceramic for wireless and sensor applications," english translation from Produktion von Leiterplatten und Systemen (PLUS), IMST GmbH, Dec. 2001.
- [11] J. Grzyb, D. Cottet, and G. Troster, "mm-wave integrated antennas on low cost MCM-D substrates," in *Electrical Perf. of Electronic Pack.*, 2000.
- [12] H. Inoue, S. Fukutake, and H. Ohata, "Liquid crystal polymer film heat resistance and high dimensional stability," in *Proc. Pan Pacific Microelect. Symp.*, Feb. 2001, pp. 273–278.
- [13] X. Wang, J. Engel, and C. Liu, "Liquid crystal polymer (LCP) for MEMS: processes and applications," *J. Micromech. Microeng.*, vol. 13, 2003.
- [14] L. M. Higgins III, "Hermetic and optoelectronic packaging concepts using multi-layer and active polymer systems," *Advancing Microelectronics*, vol. 30, no. 4, pp. 6–13, July 2003.

- [15] K. Jayaraj, T. E. Noll, and D. R. Singh, "RF characterization of a low cost multichip packaging technology for monolithic microwave and millimeter wave integrated circuits," in *URSI Int. Signals, Systems, and Electronics Symp.*, Oct. 1995, pp. 443–446.
- [16] G. Zou, H. Gronqvist, P. Starski, and J. Liu, "High frequency characteristics of liquid crystal polymer for system in a package application," in *IEEE 8th Int. Advanced Packaging Materials Symp.*, Mar. 2002, pp. 337–341.
- [17] G. Zou, H. Gronqvist, J. P. Starski, and J. Liu, "Characterization of liquid crystal polymer for high frequency system-in-a-package applications," *IEEE Trans. Adv. Packag.*, vol. 25, 2002.
- [18] B. Farrell and M. S. Lawrence, "The processing of liquid crystalline polymer printed circuits," in *IEEE Electronic Components and Technology Conf.*, May 2002, pp. 667–671.
- [19] C. Murphy, Rogers Corporation, private communication. Jan. 2004.
- [20] D. C. Thompson, O. Tantot, H. Jallageas, G. E. Ponchak, M. M. Tentzeris, and J. Pappapolymerou, "Characterization of liquid crystal polymer (lcp) material and transmission lines on lcp substrates from 30-110 ghz," *IEEE Trans. Microwave Theory Tech.*, vol. 52, 2004.
- [21] E. C. Culbertson, "A new laminate material for high performance pcbs: Liquid crystal polymer copper clad films," in *IEEE Electronic Components and Technology Conf.*, May 1995, pp. 520–523.
- [22] K. Jayaraj, T. E. Noll, and D. R. Singh, "A low cost multichip packaging technology for monolithic microwave integrated circuits," *IEEE Trans. Antennas Propagat.*, vol. 43, pp. 992–997, Sept. 1995.
- [23] C. Khoo, B. Brox, R. Norrhede, and F. Maurer, "Effect of copper lamination on the rheological and copper adhesion properties of a thermotropic liquid crystalline polymer used in pcb applications," *IEEE Trans. Comp., Packag, Manufact., Technol.*, vol. 20, pp. 219–226, July 1997.
- [24] T. Suga, A. Takahashi, K. Saijo, and S. Oosawa, "New fabrication technology of polymer/metal lamination and its application in electronic packaging," in *IEEE 1st Int. Polymers and Adhesives in Microelectronics and Photonics Conf.*, Oct. 2001, pp. 29–34.
- [25] X. Wang, L. Lu, and C. Liu, "Micromachining techniques for liquid crystal polymer," in *14th IEEE Int. MEMS Conf.*, Oct. 2001, pp. 21–25.
- [26] K. Brownlee, S. Bhattacharya, K. Shinotani, C. P. Wong, and R. Tummala, "Liquid crystal polymers (LCP) for high performance SOP applications," in *8th Int. Adv. Packag. Materials Symp.*, Mar. 2002, pp. 249–253.

- [27] J. Kivilahti, J. Liu, J. E. Morris, T. Suga, and C. P. Wong, "Panel-size component integration (PCI) with molded liquid crystal polymer (LCP) substrates," in *IEEE Electronic Components and Technology Conf.*, May 2002, pp. 955–961.
- [28] T. Suga, A. Takahashi, M. Howlander, K. Saijo, and S. Oosawa, "A lamination technique of LCP/Cu for electronic packaging," in *2nd Int. IEEE Polymers and Adhesives in Microelectronics and Photonics Conf.*, June 2002, pp. 177–182.
- [29] T. Zhang, W. Johnson, B. Farrell, and M. S. Lawrence, "The processing and assembly of liquid crystalline polymer printed circuits," 2nd Int. IEEE Polymers and Adhesives in Microelectronics and Photonics Conf., 2002, presented at the.
- [30] L. Chen, M. Crnic, L. Zonghe, and J. Liu, "Process development and adhesion behavior of electroless copper on liquid crystal polymer (LCP) for electronic packaging application," *IEEE Trans. Comp., Packag, Manufact., Technol.*, vol. 25, pp. 273–278, Oct. 2002.
- [31] Modern Machine Shop Online. [Online]. Date accessed: Sept. 2004. Available: <http://www.mmsonline.com/articles/030107.html>
- [32] PMTEC LCP Materials Symp., Huntsville, AL, Oct. 29, 2002.
- [33] H. Kanno, H. Ogura, and K. Takahashi, "Surface mountable liquid crystal polymer package with vertical via transition compensating wire inductance up to V-band," in *IEEE MTT-S Int. Microwave Symp. Dig.*, vol. 2, June 2003, pp. 1159–1162.
- [34] M. F. Davis, S.-W. Yoon, S. Pinel, K. Lim, and J. Laskar, "Surface mountable liquid crystal polymer package with vertical via transition compensating wire inductance up to v -band," in *IEEE MTT-S Int. Microwave Symp. Dig.*, vol. 2, June 2003, pp. 1155–1158.
- [35] L. Hsieh and K. Chang, "Equivalent lumped elements G , L , C , and unloaded Q 's of closed- and open-loop ring resonators," *IEEE Trans. Microwave Theory Tech.*, vol. 50, 2002.
- [36] I. Wolff and N. Knoppik, "Microstrip ring resonator and dispersion measurement on microstrip lines," *Electron. Lett.*, vol. 7, no. 26, pp. 779–781, Dec. 1971.
- [37] J. Frey, *Microwave Integrated Circuits*. Dedham, MA: Artech House, 1975.
- [38] R. B. Marks, "A multiline method of network analyzer calibration," *IEEE Trans. Microwave Theory Tech.*, vol. 39, pp. 1205–1215, Dec. 1991.
- [39] D. M. Pozar, *Microwave Engineering*. New York, NY: Wiley, 1998.
- [40] R. A. Pucel, D. J. Mass, and C. P. Hartwig, "Losses in microstrip," *IEEE Trans. Microwave Theory Tech.*, vol. MTT-16, pp. 342–350, June 1968.
- [41] –, "Correction to Losses in microstrip," *IEEE Trans. Microwave Theory Tech.*, vol. MTT-16, p. 1064, Dec. 1968.

- [42] B. C. Wadell, *Transmission Line Design Handbook*. Norwood, MA: Artech House, 1991.
- [43] K. C. Gupta, R. Garg, I. Bahl, and P. Bhartia, *Microstrip Lines and Slotlines 2nd ed.* Norwood, MA: Artech House, 1996.
- [44] L. J. van der Pauw, "The radiation of electromagnetic power by microstrip configurations," *IEEE Trans. Microwave Theory Tech.*, vol. 25, pp. 719–725, Sept. 1977.
- [45] M. D. Abouzahra and L. Lewin, "Radiation from microstrip discontinuities," *IEEE Trans. Microwave Theory Tech.*, vol. MTT-27, pp. 722–723, Aug. 1979.
- [46] P. Guillon and Y. Garault, "Complex permittivity of mic substrate," *AEU*, 1981.
- [47] S. Kennedy, Rogers Corporation, private communication. Sept. 2004.
- [48] J. Baker-Jarvis, M. D. Janezic, B. Riddle, C. L. Holloway, N. G. Paulter, and J. E. Blendell, "Dielectric and conductor-loss characterization and measurements on electronic packaging materials," in *National Institute of Standards and Technology NIST Technical Note 1520*, July 2001.
- [49] G. DeJean, R. Bairavasubramanian, D. Thompson, G. E. Ponchak, M. M. Tentzeris, and J. Papapolymerou, "Liquid crystal polymer (LCP): A new organic material for the development of multilayer dual-frequency/dual-polarization flexible antenna arrays," *IEEE Antennas Wireless Propagat. Lett.*, vol. 4, pp. 22–25, 2005.
- [50] R. Bairavasubramanian, D. Thompson, G. DeJean, G. E. Ponchak, M. M. Tentzeris, and J. Papapolymerou, "Development of mm-wave dual-frequency multilayer antenna arrays on liquid crystal polymer (LCP) substrate," in *IEEE AP-S Int. Antennas and Prop. Symp. Dig.*, July 2005, pp. 393–396.
- [51] R. Tummala, *Fundamentals of Microsystems Packaging*. New York, NY: McGraw-Hill, 2001.
- [52] G. Riley. (2004, May) Hermeticity: much to do about nothing. Flip Chips Dot Com. [Online]. Date accessed: Oct. 2005. Available: <http://www.flipchips.com/tutorial41.html>
- [53] The benefits of selecting RT/Duroid 6010LM for band pass filter applications. Rogers Corporation. Date accessed: Nov. 2005. [Online]. Available: <http://www.rogerscorporation.com/mwu/pdf/rt295.pdf>
- [54] D. Thompson, M. M. Tentzeris, and J. Papapolymerou, "Packaging of MMICs in multilayer LCP substrates," *IEEE Microwave Wireless Compon. Lett.*, 2006.
- [55] K. Gilleo, J. Belmonte, and G. Pham-Van-Diep, "Low ball BGA: a new concept in thermoplastic packaging," in *IEEE 29th Intl. Elect. Manuf. Tech. Symp.*, July 2004, pp. 345–354.
- [56] R. J. Ross, "LCP injection molded packages - keys to JEDEC 1 performance," in *IEEE 54th Elect. Comp. Tech. Conf.*, June 2004, pp. 1807–1811.

- [57] M. A. Morton and J. Papapolymerou, "Wide-band finite ground coplanar (FGC) interconnects for on-chip packaging of RF MEMS switches used in smart antennas and phased arrays," *IEEE Antennas Wireless Propagat. Lett.*, vol. 3, pp. 239–242, 2004.
- [58] G. M. Rebeiz, *RF MEMS Theory, Design, and Technology*. New York: Wiley, 2003.
- [59] D. Thompson, N. Kingsley, G. Wang, J. Papapolymerou, and M. M. Tentzeris, "RF characteristics of thin film liquid crystal polymer (LCP) packages for RF MEMS and MMIC integration," in *IEEE MTT-S Int. Microwave Symp. Dig.*, June 2005, pp. 857–860.